A search for Fermi LAT pulsars in archival VERITAS data

Jonathan Tyler

Doctor of Philosophy

Department of Physics

McGill University

Montreal, Quebec

2018-12-13

A thesis submitted to the Faculty of Graduate Studies and Research in partial fulfilment of the requirements for the degree of Doctor of Philosophy

DEDICATION

This thesis is dedicated to my friends and family.

ACKNOWLEDGEMENTS

I would first like to thank my supervisor Prof. Ken Ragan for all his advice, guidance and patience over the years and for convincing me to join the VERITAS group at McGill, which introduced me to the amazing world of high-energy astrophysics. I would next like to thank Prof. David Hanna for sharing much knowledge and insight and for effectively acting as a second supervisor.

Thank you to Gregory Richards for working on this project with me, for his contributions to this work, for many fruitful discussions and for doing the bulk of the work on the paper describing the pulsar search while I worked on this thesis. I am particularly grateful to Andrew McCann for introducing me to gamma-ray pulsar astronomy, and for his enthusiasm for the subject, which convinced me to become involved in the pulsar search. I would also like to thank him for his many contributions to this work and for all of his insights. I would next like to thank Nepomuk Otte for all of his insight regarding the pulsar search and for initially suggesting the gate finding method that I implemented. Thank you to Tony Lin for many good conversations regarding the pulsar analysis methods and for helping me to fix bugs in the code. I'm also grateful to the members of the VERITAS collaboration not already mentioned that provided insights regarding the pulsar search: Benjamin Zitzer, John Finley, Avery Archer, Philip Kaaret, John Quinn, David Williams and Ralph Bird. Special thanks to Gernot Maier who provided indispensable help with the Event Display analysis package.

I wish to thank the past and present graduate students and post-docs of the

McGill VERITAS group not already mentioned that I've had the privilege of getting to know and working with: David Staszak, Jean-Francois Rajotte, Gordana Tesic, Qi Feng, Sajan Kumar, Stephan O Brien, Simon Archambault, Sean Griffin, Roxanne Guenette, Michael McCutcheon, Audrey Mcleod, Matthew Lundy, Samuel Trepanier, Étienne Bourbeau, Gabriel Chernitsky, Thomas Rosin, Sreela Das and Emma Ellingwood. I would next like to express my appreciation to the Professors of the McGill physics department who taught me many things over the years and supported me in my academic endeavours: Andreas Warburton, Matt Dobbs, Brigitte Vachon, Tracy Webb, Victoria Kaspi, Robert Rutledge, Andrew Cumming, Daryl Haggard and Gil Holder. I would also like to extend my thanks to the staff of the McGill physics department. Special thanks to Paul Mercure and Juan Gallego, who helped me with many computer problems.

Next, I wish to thank all of the past and present members of the VERITAS collaboration not yet mentioned that I've had the privilege of meeting and working with. I would also like to express my gratitude to the past and present staff at the Fred Lawrence Whipple Observatory that supported me while I was there: Pascal Fortin, Michael Daniel, Ken Gibbs, Martin Schroedter, Gareth Hughes, Jack Musser, George Jones, Danny West and Cesar Lopez. Special thanks to Trevor Weekes for being the father of ground based gamma-ray astronomy and a very nice person.

I would next like to thank my family. To my mother Heather Ayerst, thank you for all your support over the years. This work would not have been possible without you. To my father James Tyler, thank you for inspiring me to appreciate nature and to cultivate diverse interests. To my sisters Jennifer Tyler and Megan Parisé,

my brother in law Dan Shumuk, my nieces Isla and Zoe Shumuk, my aunts Debbie Tyler, Cheryl Buttrum and Valerie Ayest, my uncles Robin Tyler, Keith Buttrum and Jay Ayerst, and my cousins Ben Buttrum, Angela Buttrum, Maggie Buttrum and Rachel Ayerst, lots of love. Thank you all for supporting me in various ways. Special thanks to my grandparents Lucile Ayerst, James Ayerst, Barbara Tyler and Merton Tyler, you continue to inspire me in many ways.

Thank you to my friends Jordan Hughes, Geoff Livingston, Daniel Thorne, Caitlin O'Brien, Coriander Golden, Sam Lazarus, Sophie Nasser, Genki Kondo, Kate Washington, Sam Vipond, Alex Botros, Carolyn Wyse, Mike O'Brien, and Aaron Ball. Thanks for the great times I've had with you.

Finally, I would like to thank my partner Jessica Fitzgerald, who has helped me through the writing of this thesis and who has shared her life with me and our four legged friends Oliver, Zena and Orville.

ABSTRACT

Pulsars are extra-terrestrial sources of periodic radiation thought to consist of highly magnetized, rapidly rotating neutron stars. As the neutron star rotates, beams of radiation may become visible to an observer at different rotational phases, causing an observed periodic signal. Pulsars are mostly detected at radio frequencies, but are also detected in optical light, X-rays and gamma rays. Radiative emission from pulsars is currently not well understood. The main open questions in the field are the radiation emission mechanisms and the location of the emission regions. This work describes the search for pulsations from 14 pulsars with VERITAS, a ground-based very-high-energy (VHE) gamma-ray observatory. Currently only two pulsars have been detected at VHE energies: the Crab and Vela. This search was undertaken in order to increase this number, and to constrain pulsar gamma-ray emission scenarios. The data set consists of archival data, where pulsars detected by the Large Area Telescope (LAT) on-board the Fermi Gamma-ray Space Telescope were observed directly or were present in the field of view during observations of other sources. The VERITAS data for each pulsar were analyzed with three sets of data selection cuts, and two periodicity tests for each set of cuts. No pulsations were discovered for any of these analyses. Flux upper limits were calculated for each pulsar at the 95% confidence level for each set of cuts using two separate methods. The limits for each pulsar are contextualized with spectra produced from LAT data, and the results are interpreted within the context of current pulsar gamma-ray emission scenarios.

ABRÉGÉ

Les pulsars sont des sources extraterrestres de rayonnements périodiques que l'on pense être constitués d'étoiles à neutrons fortement magnétisées et à rotation rapide. Lorsque l'étoile à neutrons tourne, des faisceaux de rayonnement peuvent devenir visibles à un observateur à différentes phases de rotation, provoquant l'observation d'un signal périodique. Les pulsars sont principalement détectés aux fréquences radio, mais sont également détectés avec la lumière optique, les rayons X et les rayons gamma. L'émission radiative des pulsars n'est actuellement pas bien comprise. Les questions principales dans ce domaine d'étude sont les mécanismes d'émission de rayonnement et l'emplacement des régions d'émission. Ce travail décrit la recherche de pulsations à partir de 14 pulsars avec VERITAS, un observatoire rayon gamma à très hautes énergies situé sur la Terre. En ce moment, seulement deux pulsars ont été détectés en rayons gamma a très hautes énergies: les pulsars Crabe et Vela. Cette recherche a été entreprise pour augmenter ce nombre et pour contraindre les scénarios d'émission de rayons gamma. L'ensemble de données est constitué de données d'archives, où des pulsars détectés par le Large Area Telescope (LAT) à bord du Fermi Gamma-ray Space Telescope ont été observés directement ou étaient présents dans le champ de vision pendant des observations d'autres sources astronomiques. Les données VERITAS pour chaque pulsar ont été analysées avec trois ensembles de coupes de sélection de données, et deux tests de périodicité pour chaque ensemble de coupes. Aucune pulsation a été découverte pour ces analyses. Les limites supérieures du flux ont été calculées pour chaque pulsar au niveau de confiance de

95% pour chaque ensemble de coupes en utilisant deux méthodes distinctes. Les limites pour chaque pulsar sont contextualisées avec des spectres produits à partir de données du LAT, et les résultats sont interprétés dans le contexte des scénarios actuels d'émission de rayons gamma par les pulsars.

STATEMENT OF ORIGINAL CONTRIBUTIONS

The author has contributed in many ways to the VERITAS collaboration over the course of his PhD studies at McGill.

The pulsar search described in this thesis was performed in collaboration with several others. The author worked closely with Gregory Richards on this project, who performed a similar analysis using a different analysis package, allowing the methods and results to be cross checked. The author is a joint author on the paper describing the pulsar search, which will be submitted to the Astrophysical Journal, and is listed as a corresponding author. Most of the material presented in Chapters 6 and 7 describes the authors own work, presenting the details of the search for pulsations in archival VERITAS data from 14 pulsars detected by the Fermi LAT gamma-ray space telescope and the calculation of flux upper limits for these sources. The author processed all of the VERITAS data and produced all of the VERITAS results, implemented code for calculating VERITAS flux upper limits, identified and fixed several bugs in the code and implemented the phase gate finding algorithm described in the text. Greg Richards performed the Fermi LAT analyses required to produce the pulsar spectra and implemented the code for displaying the VERITAS flux upper limits with those spectra. Andrew McCann implemented the code for generating the VERITAS run list for each source, the code that passed the recorded arrival times of the VERITAS gamma ray candidate events to the TEMPO2 software, code for calculating VERITAS flux upper limits and the code for displaying the VERITAS phase profiles of the pulsars. He also obtained the timing solutions

used in this work, and performed the cross correlation analyses required to calculate the phase offsets described in the text.

As part of his PhD work, the author implemented a muon identification algorithm he devised (as described in his master's thesis) as well as improving existing muon analysis algorithms in the Event Display analysis package. These algorithms are now applied to all of the VERITAS data to identify and analyze muon images in order to monitor the optical responses of the telescopes.

Over a period of five years, the author travelled to the VERITAS site seven times in order to contribute to the operation of the observatory. In 2012, the author spent three months at the VERITAS site, primarily working as part of the day crew, where he helped with the day to day maintenance of the instrument. During this three month period, he also participated in two observing shifts. The author participated in a total of eight ten-day observing shifts over the course of his PhD studies. On three of these occasions, the author was in charge of the observing shift (the shift czar), where he was responsible for the the observing schedule and decisions regarding the operation of the observatory.

The author was also in charge of improving and maintaining the VERITAS data quality monitoring (DQM) website described in the text for several years during his PhD studies. This included the transfer of the website from McGill to the VERITAS site, which significantly improved the reliability of the website. The author also participated in four data quality monitoring shifts, where he evaluated the quality of the data and identified problems with the VERITAS hardware using the DQM website.

The author wrote three internal memos for the VERITAS collaboration: a memo describing the muon identification technique, a study regarding a dedicated muon trigger for VERITAS and a memo describing the details of the phase gate finding algorithm described in the text.

The author attended weekly McGill VERITAS group meetings, and presented the results of his work at these meetings on many occasions. New papers on astrophysics, high energy physics and high-energy astrophysics were also presented by the author to the McGill VERITAS group at weekly journal clubs. The author travelled to six VERITAS collaboration meetings during his PhD studies, giving oral presentations regarding muon analysis techniques on two of these occasions. The author attended two annual meetings of the Center for Research in Astrophysics of Quebec (CRAQ) during his PhD studies, and four CRAQ summer schools, giving an oral presentation on space-based gamma-ray astronomy at one of them. The author also attended the 2012 cosmic-ray summer school in Erice Sicily. In the summer of 2013, the author travelled to the International Cosmic Ray Conference (ICRC) in Rio de Janeiro, and presented the muon identification technique in a poster. The author also presented this method in a poster at the Canadian Association of Physicists conference in 2013, winning best student presentation in the instrumentation category and third best student poster, allowing the author to publish the technique in an issue of Physics In Canada (PIC).

TABLE OF CONTENTS

LIST OF TABLES

LIST OF FIGURES

CHAPTER 1
Introduction and Thesis outline

1.1 Introduction

Astronomy, the observation and study of celestial objects and phenomena, is one of the oldest natural sciences. Humans have been observing the light from the night sky with the naked eye for millennia, making optical astronomy the oldest and most familiar form of astronomy. The invention of the optical telescope in the early 15th century allowed much more detailed optical observations of the night sky, leading to new astronomical discoveries. Due to advancements in physics and instrumentation in the 20th century, astronomical observations are now performed throughout the electromagnetic (EM) spectrum: with radio waves, infrared, optical and ultraviolet light, X-rays and gamma rays. Figure 1–1 shows the wavelengths of the electromagnetic spectrum, with atmospheric opacities shown for each wavelength. As can be seen from the figure, astronomical observations of optical light, some infrared wavelengths and radio waves may be performed from the ground. Astronomical observations at other wavelengths of the EM spectrum require the use of space telescopes, with the exception of gamma rays, some of which may be observed indirectly from the ground (see section 1.2). Astronomy is now also performed with non-electromagnetic messengers, including cosmic rays, neutrinos and gravitational waves, using specialized space-based and ground-based detectors. The development of new forms of astronomy has historically led to new astronomical discoveries, such

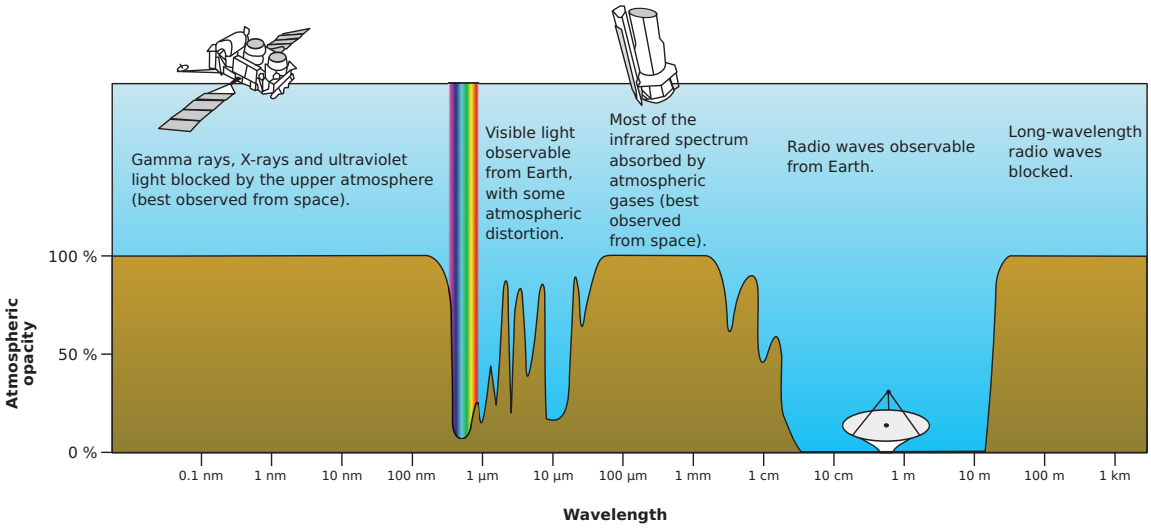

Figure 1–1: The wavelengths of the electromagnetic (EM) spectrum, with atmospheric opacities shown for each wavelength. Astronomical observations of optical light, some infrared wavelengths and radio waves may be performed from the ground. Astronomical observations of the other wavelengths of the EM spectrum require the use of space telescopes, with the exception of very high energy (VHE) gamma rays, which may be observed indirectly from the ground (see section 1.2). Figure from [23].

as the discovery of pulsars (see section 1.3) as a result of the development of radio astronomy.

This thesis describes the search for pulsars with VERITAS, a ground-based gamma-ray observatory. In this chapter, space-based and ground-based gamma ray astronomy will be reviewed, followed by a brief overview of pulsars. Chapter 2 presents a detailed overview of pulsars with an emphasis on pulsar gamma-ray emission models. Chapter 3 presents a summary of space-based and ground based gamma-ray pulsar observations and a description of the VERITAS archival pulsar search. Chapter 4 presents an outline of the imaging atmospheric Cherenkov technique, and describes the VERITAS IACT array in detail. Chapter 5 describes the VERITAS data analysis techniques. Chapter 6 presents the results of the VERITAS archival pulsar search. Chapter 7 presents an interpretation of the results shown in Chapter 6 within the context of current pulsar gamma-ray emission models, and conclusions.

1.2 Gamma-ray astronomy

Within the context of astronomy, 'gamma ray' refers to photons with energies of 100 keV and above, making gamma rays the most energetic photons of the electromagnetic spectrum. Gamma-ray astronomy probes the most energetic and violent phenomena in the universe, such as active galactic nuclei (AGN), supernova remnants (SNR), and pulsars. In these sources, charged particles are accelerated to high energies, emitting gamma rays by various non-thermal processes, including synchrotron radiation, curvature radiation, inverse Compton scattering and neutral pion decay. As mentioned in section 1.1, extra-terrestrial gamma rays are absorbed by the

Band	Energy range
Low energy (LE)	100 keV to 10 MeV
Medium energy (ME)	10 MeV to 30 MeV
High energy (HE)	30 MeV to 100 GeV
Very high energy (VHE)	100 GeV to 100 TeV
Ultra high energy (UHE)	100 TeV to 100 PeV
Extremely high energy (EHE)	100 PeV and above

Table 1–1: Gamma ray energy bands with corresponding energy ranges.

atmosphere. In order to perform gamma-ray astronomy by directly detecting the observed photons, space telescopes must be used. The gamma-ray band is subdivided into various sub-bands, which are shown in Table 1–1. Space telescopes are sensitive to gamma rays from the LE to the HE bands. However, the fluxes of gamma rays in the VHE band and above are insufficient to be detected by space-based telescopes in large numbers. At these energies, ground-based detectors that observe the gamma rays by indirect means must be used. In this section, an overview of space-based gamma-ray astronomy will be presented, with an emphasis on the HE band, where all of the known gamma-ray pulsars have been detected. This is followed by a brief description of the current state of ground-based gamma-ray astronomy in the VHE band, where two pulsars have currently been detected.

1.2.1 Space-based gamma-ray astronomy

This section will give an overview of gamma-ray astronomy, with an emphasis on the HE band. In this energy range, electron-positron pair production is the dominant photon-matter interaction mechanism, and gamma-ray astronomy is performed with pair-production telescopes. Incoming gamma rays pair produce in these telescopes, and the resulting electron-positron pairs are tracked, allowing the arrival directions

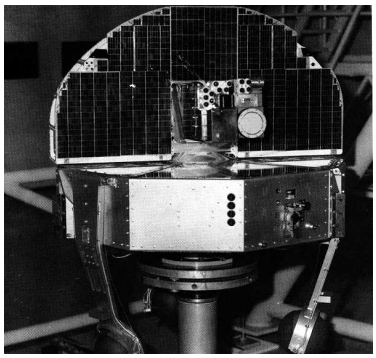

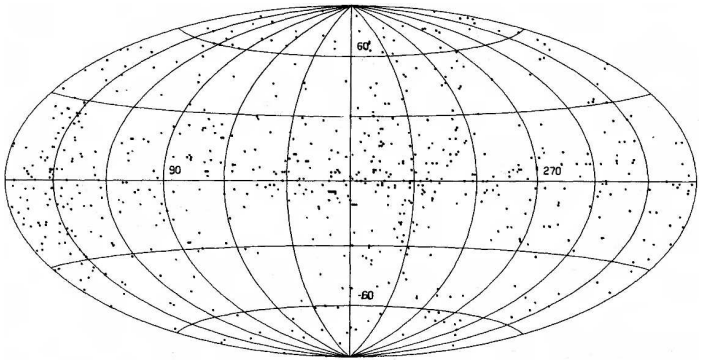

Figure 1–2: Left: The OSO-3 satellite, launched in 1967, included a gamma ray telescope that operated for approximately 16 months. Figure from [101]. Right: the arrival directions of the gamma rays detected by the OSO-3 satellite in galactic coordinates. The distribution of arrival directions was found to be highly anisotropic, and clustered around the galactic plane. Figure from [51].

of the gamma rays to be determined. The combined energies of the electron-positron pairs are also measured, typically via absorption in calorimeters, allowing the energies of the gamma rays to be estimated. At lower energies, different types of telescopes are used for space-based gamma ray astronomy. That topic is beyond the scope of this thesis.

The first space-based gamma-ray telescope, Explorer 11, was launched in 1961. The telescope consisted of CsI and NaI crystal scintillators, a Cherenkov counter, and a plastic scintillator anti-coincidence shield. Gamma-ray data was acquired over a period of four months, resulting in 22 detected gamma rays. The arrival directions of these gamma rays showed no correlation with any known cosmic source.

The Third Orbiting Solar Observatory (OSO-3), shown in Figure 1–2 (left), was launched in 1967, and included a gamma-ray telescope. The gamma-ray telescope consisted of CsI and plastic scintillators, a Cherenkov counter, a tungsten

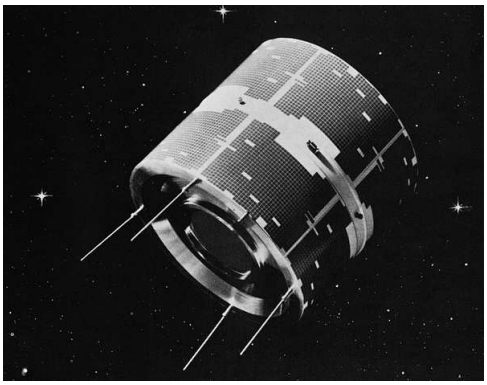

Figure 1–3: Left: the SAS-2 satellite was launched in 1972, and performed gamma ray observations for approximately seven months. Figure from [102]. Right: the COS-B satellite was launched in 1975, and operated for approximately seven years. Figure from [99].

and NaI detector for measuring the energies of the pairs, and a plastic scintillator anti-coincidence shield. The gamma-ray telescope operated for approximately 16 months, and detected 621 cosmic gamma-ray events. The arrival directions of the gamma rays were found to be highly anisotropic and clustered around the galactic plane. Figure 1–2 (right) shows the arrival directions of the detected gamma rays in galactic coordinates.

The second NASA Small Astronomy Satellite (SAS-2), shown in Figure 1–3 (left), was launched in 1972, and consisted of two spark chamber tracking detectors, four Cherenkov counters, four plastic scintillator counters, and a plastic scintillator anti-coincidence shield. Gamma-ray data was taken for approximately seven months, resulting in the first detailed look at the gamma-ray sky and the detection of several sources, including the Crab and Vela pulsars.

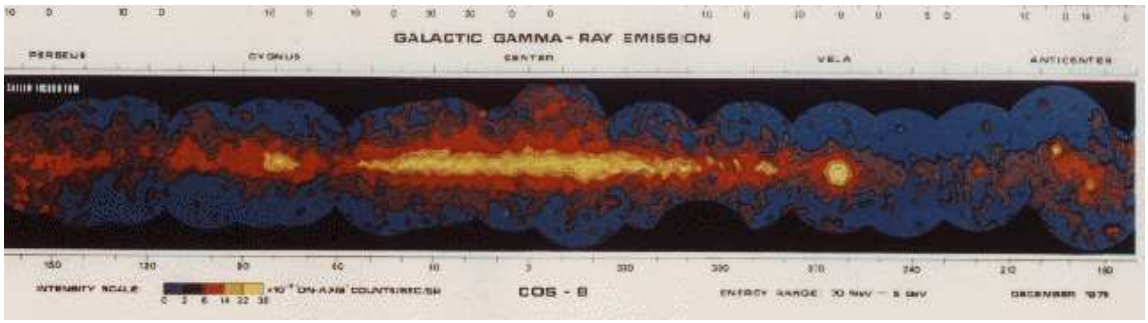

Figure 1–4: The first map of the galactic plane in gamma rays, produced by COS-B. Figure from [100].

The COS-B satellite (Figure 1–3, right) was launched in 1975, and recorded gamma ray data for approximately seven years. The telescope consisted of a spark chamber tracking detector, a CsI calorimeter, and a plastic scintillator anti-coincidence shield. COS-B detected 25 gamma-ray sources, and produced a gamma-ray map of the galactic plane, shown in Figure 1–4.

The Compton Gamma-Ray Observatory (CGRO), shown in Figure 1–5 (left), was launched in 1991 and de-orbited in 2000. The instruments on-board CGRO included: the Imaging Compton Telescope (COMPTEL), a Compton scattering telescope; the Burst and Transient Source Experiment (BATSE), a full-sky gamma-ray burst detector; the Oriented Scintillation Spectrometer Experiment (OSSE), a gamma-ray spectrometer; and the Energetic Gamma Ray Experiment Telescope (EGRET), a pair-production telescope sensitive to gamma rays in the HE band. EGRET consisted of a spark chamber tracking detector, a NaI calorimeter and a plastic scintillator anti-coincidence shield. EGRET produced the first map of the full sky in HE gamma rays, shown in Figure 1–6 (top), and detected 271 sources of

Figure 1–5: Left: the Compton Gamma-Ray Observatory was launched in 1991 and de-orbited in 2000. Figure from [96]. Right: The Fermi Gamma-ray Space Telescope was launched in 2008, and is currently in orbit. Figure from [97].

HE gamma rays, which were published in the third EGRET catalogue (3EG). The locations of the 3EG sources are shown in Figure 1–6 (bottom) in galactic coordinates. In addition to the Crab and Vela pulsars, EGRET detected four new gamma-ray pulsars, and an additional new gamma-ray pulsar was discovered by COMPTEL (see section 3.1.1).

The AGILE satellite was launched in 2007 and is currently in orbit. The telescope consists of a silicon-tungsten tracking detector, a CsI calorimeter and a plastic scintillator anti-coincidence shield. AGILE has detected many gamma-ray sources, and discovered three new gamma-ray pulsars. The latest source catalogue published by AGILE contains 54 sources [56].

The Fermi Gamma-ray Space Telescope, shown in Figure 1–5 (right), was launched in 2008, and is also currently in orbit. The instruments on board consist of: the

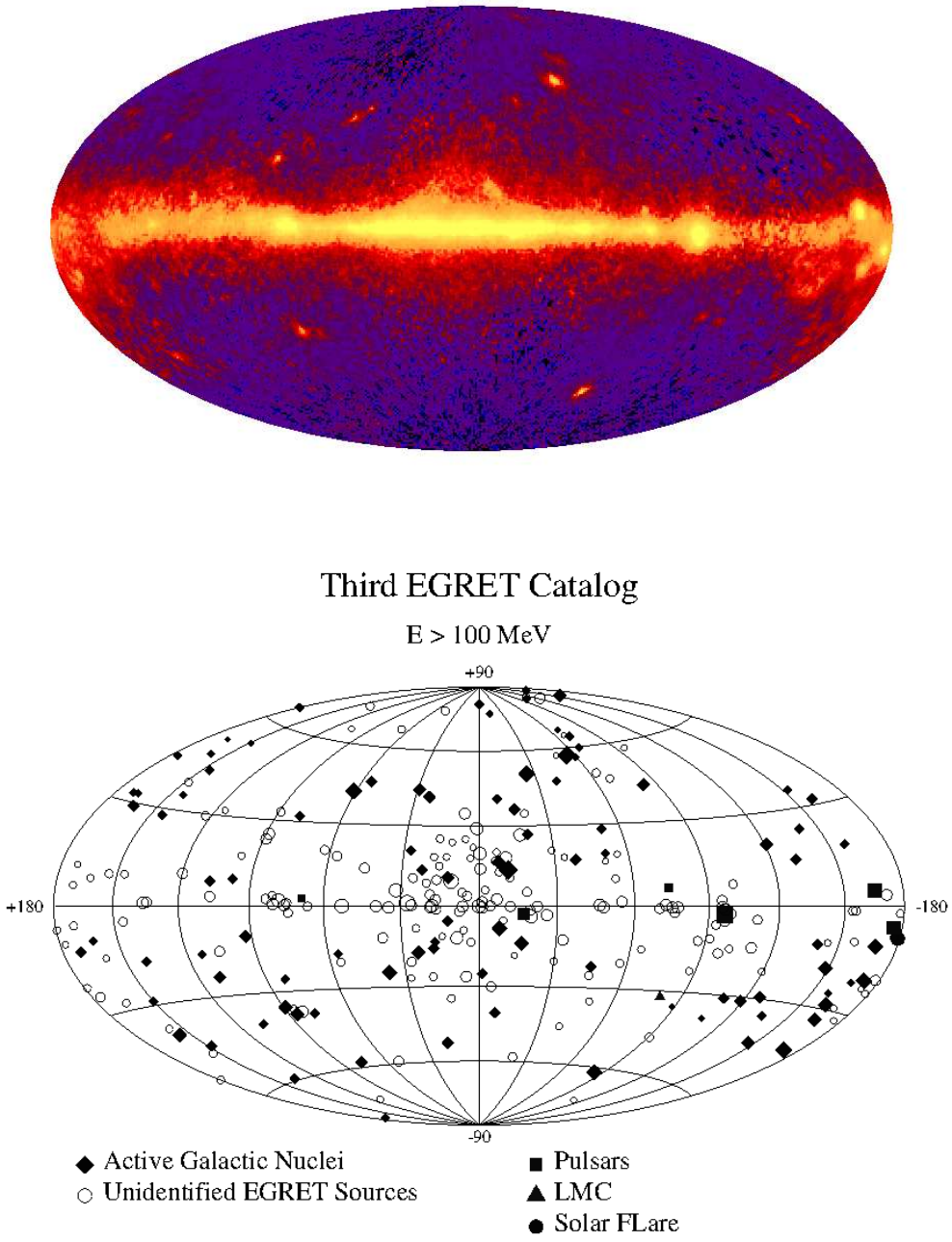

Figure 1–6: Top: the first map of the full sky in HE gamma rays, produced by EGRET. Bottom: the locations of the 271 sources in the third EGRET catalogue in galactic coordinates. Figures from [118].

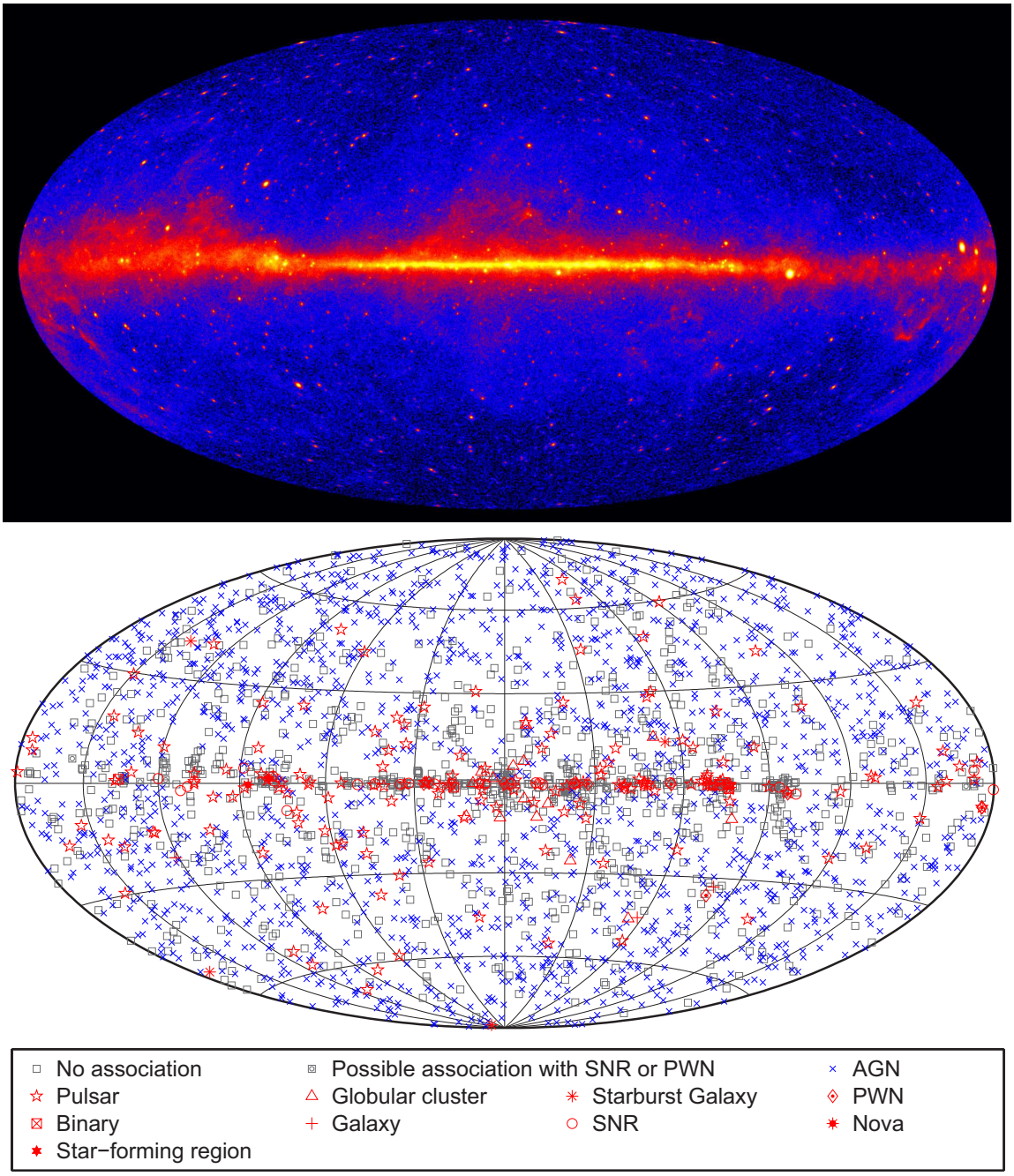

Figure 1–7: Top: a detailed view of the HE gamma-ray sky produced by Fermi LAT. Figure from [62]. Bottom: the locations of the 3033 sources listed in the Fermi Large Area Telescope third source catalogue in galactic coordinates. Figure from [32].

Gamma-ray Burst Monitor (GBM) a full-sky gamma-ray burst detector; and the Large Area Telescope (LAT), a pair-production telescope. Like AGILE, LAT consists of a silicon-tungsten tracking detector, a CsI calorimeter and a plastic scintillator anti-coincidence shield. The LAT has produced a detailed view of the HE gamma-ray sky, as shown in Figure 1–7 (top), and has increased the number of known HE gamma-ray sources by more than an order of magnitude. The newest catalogue of LAT sources, the Fermi LAT third source catalogue (3FGL), lists 3033 sources [32]. The locations of these sources are shown in Figure 1–7 (bottom). The LAT has also increased the number of known gamma-ray pulsars by more than an order of magnitude. At the time of the writing of this thesis, the LAT had detected 205 gamma ray pulsars (see section 3.1.1).

1.2.2 Ground-based gamma-ray astronomy

In the VHE band and above, gamma-ray fluxes are too low to be detected by space-based gamma-ray telescopes in large numbers due to the size limitations of the detectors that may be placed into orbit. For example, the flux of the Crab nebula, the brightest VHE gamma-ray source in the sky, has been measured to be approximately 38 photons m^{-2} yr^{-1} above 300 GeV [36]. Ground-based detectors with large detection areas must be used in order to detect gamma rays in large numbers at these energies. As mentioned in section 1.1, gamma-ray photons are absorbed by the atmosphere. This occurs via the conversion of the gamma rays into particle cascades of electrons, positrons and photons, called air showers. In order to perform gamma-ray astronomy from the ground, these air showers may be observed.

Figure 1–8: Left: the H.E.S.S array of imaging atmospheric Cherenkov telescopes, located in Namibia. Figure from [115]. Right: the MAGIC telescopes, located in La Palma, Spain. Figure from [116].

The charged particles from the air showers move at relativistic speeds as they travel through the atmosphere, causing the atmosphere to emit Cherenkov radiation (see section 4.3). Imaging atmospheric Cherenkov telescopes (IACTs) focus the Cherenkov light with large reflectors onto sensitive cameras, allowing images to be made of the air showers. The analysis of these images allows the arrival directions and energies of the gamma rays that initiated the showers to be determined. The first observed source of extra-terrestrial VHE gamma rays, the Crab nebula, was detected in 1989 by the Whipple 10 m telescope [57]. Current IACTs include: the High Energy Stereoscopic system (H.E.S.S), the Major Atmospheric Gamma Imaging Cherenkov telescopes (MAGIC), and the Very Energetic Radiation Imaging Telescope Array System (VERITAS). H.E.S.S is located in Namibia, and consists of four telescopes with 12 m diameter reflectors, and one telescope with a 28 m diameter reflector. A photograph of the H.E.S.S array is shown in Figure 1–8 (left). H.E.S.S began operations as a four-telescope array in 2003, and as a five-telescope array in 2012.

MAGIC consists of two telescopes with 17 m diameter reflectors, and is located in La Palma, Spain. A photograph of the MAGIC telescopes is shown in Figure 1–8 (right). MAGIC began single-telescope operations in 2004 and two-telescope operations in 2009. VERITAS is located in Arizona USA, and consists of four telescopes with 12 m diameter reflectors. VERITAS began operations as a four-telescope array in 2007, and is described in detail in section 4.5. The next generation IACT, the Cherenkov Telescope Array (CTA), is currently being built, and will consist of large arrays of telescopes of different sizes at a northern and southern site [90]. Only two VHE gamma-ray pulsars have currently been detected by IACTs: the Crab and Vela pulsars (see section 3.1.2). For more information about IACTs, see Chapter 4.

The charged particles from the air showers initiated by extra-terrestrial gamma rays may also be directly detected from the ground. The most advanced detector of this type is the High Altitude Water Cherenkov Observatory (HAWC), located in Puebla, Mexico. HAWC consists of 300 water Cherenkov detectors (WCDs) arranged in an array, as shown in Figure 1–9. Charged particles from air showers that pass through the WCDs cause the water to emit Cherenkov radiation, which is detected by sensitive light detectors inside the WCDs. The intensity patterns and timing information recorded by the array allow VHE gamma-ray astronomy to be performed. The latest catalogue of gamma-ray sources detected by HAWC (2HWC) contained 39 sources [31]. No gamma-ray pulsars have currently been detected with this instrument.

The VHE gamma-ray source catalog, TeVCat [1] currently lists 210 sources. Figure 1–10 shows the locations of these sources in galactic coordinates.

Figure 1–9: A photograph of the HAWC gamma-ray observatory. Figure from [114].

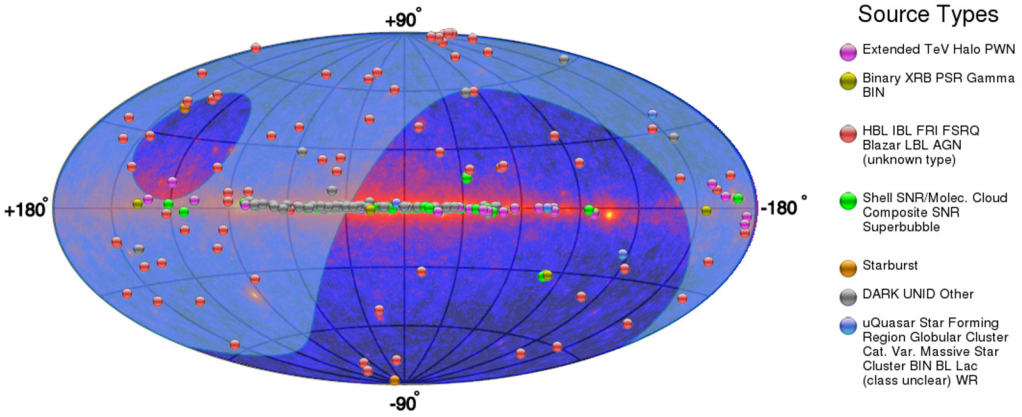

Figure 1–10: The locations in galactic coordinates of the 210 sources listed in the TeVCat catalogue of VHE gamma-ray sources. The light blue region corresponds to the region of the sky where VERITAS is most sensitive. The Fermi LAT full-sky HE gamma-ray map is shown in the background. Figure from [1].

1.3 Pulsars

Pulsars are extra-terrestrial sources of periodic radiation. They were first observed in 1967, and are thought to consist of highly magnetized, rapidly rotating neutron stars (see Chapter 2). As the neutron star rotates, beams of radiation may become visible to an observer at different rotational phases of the pulsar, causing an observed periodic signal. Pulsars are mostly detected at radio frequencies, but are also detected in optical light, X-rays and gamma rays. As mentioned in section 1.2.1, the gamma-ray pulsar catalogue has been expanded considerably by Fermi LAT, revolutionizing the field of gamma-ray pulsar astronomy. Current open questions in the field are: the nature of the gamma-ray emission mechanism, and the location of the gamma-ray emission region in the area surrounding the pulsar. Measurements of the pulse profiles of gamma-ray pulsars may constrain the location of the gamma-ray emission region. Measurements of the spectra of these pulsars or flux upper limits may constrain both the location of the gamma-ray emission region and the emission mechanism. As mentioned in section 1.2.2, the Crab and Vela pulsars are the only known VHE gamma-ray pulsars. The VERITAS archival pulsar search, the topic of this thesis, was undertaken in order to increase the number of known VHE pulsars, and to constrain pulsar gamma-ray emission scenarios. An overview of pulsars is presented in the next Chapter.

CHAPTER 2
Pulsars

2.1 Introduction

Pulsars were discovered in 1967 by Jocelyn Bell Burnell [49], who discovered a signal while analyzing the data from a radio telescope. The signal consisted of 'scruff' recorded on paper that appeared every sidereal day, which meant that the signal had an astrophysical origin. When the speed of the paper was increased while the signal was present, a series of regularly spaced pulses was revealed. Figure 2–1 (top) shows the 'scruff' that was discovered by Bell, and Figure 2–1 (bottom) shows the pulses.

Thomas Gold argued shortly after their discovery that pulsars consisted of rapidly rotating neutron stars[1] emitting beams of radiation, and compared the pulses to the light observed from a lighthouse [66]. At the time of the writing of this thesis, 2163 pulsars have been identified, mostly at radio frequencies [59] [89].

In addition to being detected in the radio, pulsars have been detected in optical light, X-rays, and gamma rays. Optical pulses were discovered for the first time from the Crab pulsar in 1969 [19]. X-ray pulsations from the Crab pulsar were discovered

[1] Neutron stars had been theorized in 1934 by Walter Baade and Fritz Zwicky [8], who suggested that they would be formed in supernovae.

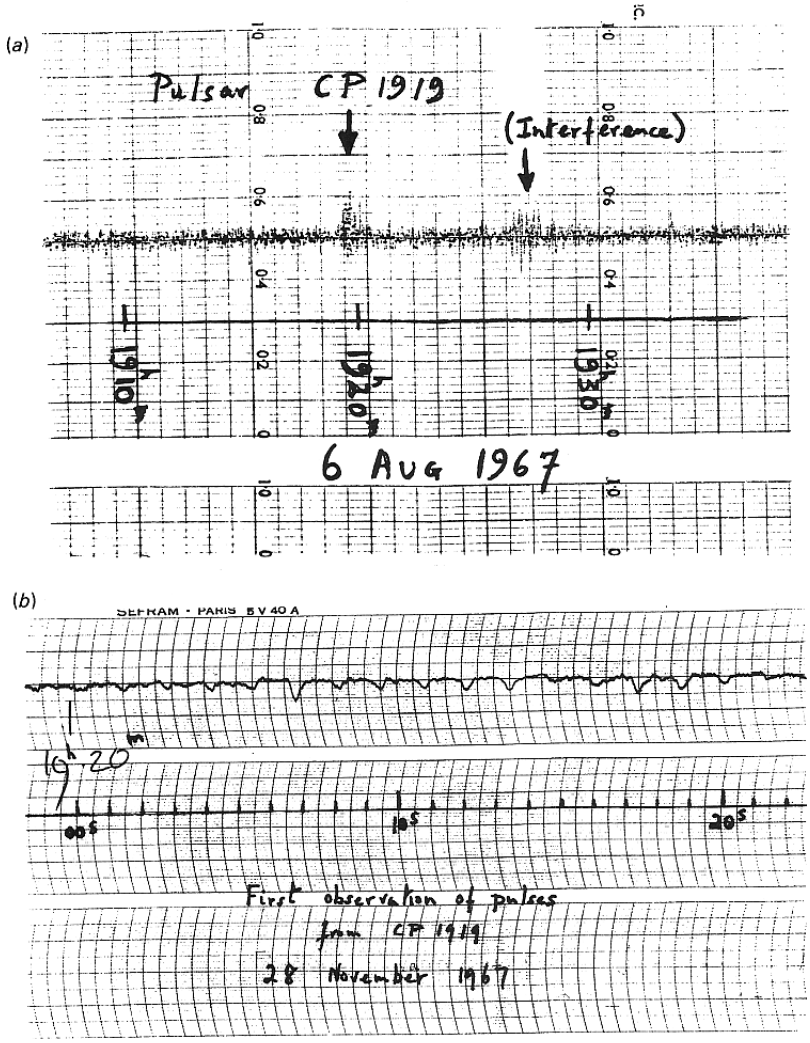

Figure 2–1: The discovery of the first pulsar. The 'scruff' found by Jocelyn Bell (top, marked "CP 1919", and the first pulses observed from a pulsar (bottom) [81].

shorty thereafter [45] [12]. Gamma-ray pulsations were first discovered from the Crab pulsar in data from the SAS-2 satellite in 1974 [43].

Pulsars may be categorized according to the dominant mechanism that produces the observed electromagnetic radiation: rotation-powered pulsars, accretion-powered pulsars and magnetars. Rotation-powered pulsars are observed to spin down, and are powered by the loss of the rotational energy of the pulsar. These pulsars account for the bulk of the observed radio, optical and gamma-ray pulsars, and include the pulsars which are the subject of this thesis. Accretion-powered pulsars are thought to be powered by the accretion of matter from a companion star. The in-falling matter is channelled onto the poles of the pulsar, where it falls onto the surface, emitting thermal radiation, mostly in soft X-rays. Accretion-powered pulsars account for the bulk of observed X-ray pulsars, but do not tend to emit radiation at other wavelengths. Magnetars are pulsars with very strong magnetic fields compared to other pulsars and are thought to be powered by the decay of their magnetic field. Anomalous X-ray pulsars (AXPs), and soft gamma repeaters (SGRs) are thought to be examples of magnetars.

Rotation-powered pulsars may be placed into two categories, according to their observed pulse periods P and period derivatives $\dot{P}$: young pulsars and millisecond pulsars. Most young pulsars have periods of over 10 ms and period derivatives between 10^{-12} to 10^{-17} ss^{-1}. Their estimated ages and magnetic field strengths (see section 2.3) range from $\sim 10^3$ to 10^8 years, and $\sim 10^{11}$ to 10^{13} G respectively. Young pulsars account for the majority of known pulsars, and have been observed in radio, optical light, X-rays and gamma rays. Gamma-ray pulsars tend to be very

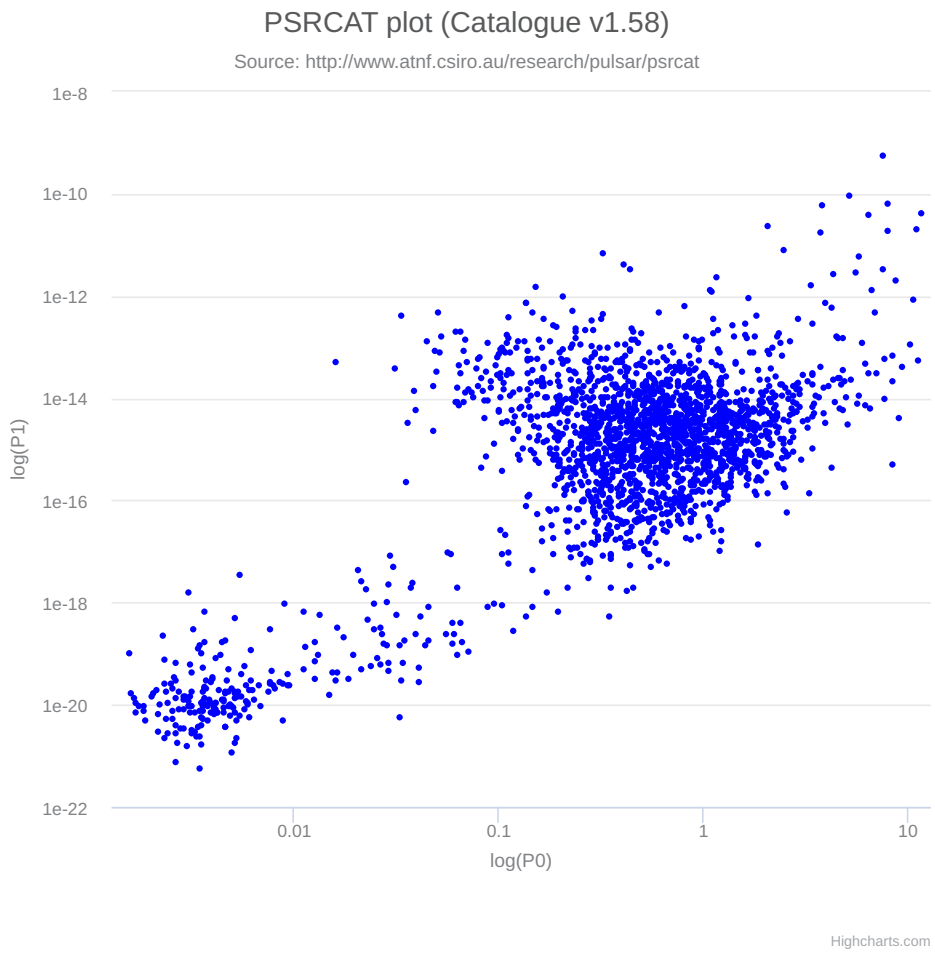

Figure 2–2: The period derivatives of the known pulsars plotted vs their periods: a P - $\dot{P}$ diagram. The period values are expressed in seconds and the period derivatives are expressed in seconds per second. The young pulsars correspond to the population located at the top right of the diagram and millisecond pulsars correspond to the smaller population located at the bottom left. Figure modified from [59] [89].

young, with most having estimated ages of between 10^3 and 10^6 years. Millisecond pulsars mostly have periods of between 1 ms and 10 ms, and much smaller period derivatives, ranging from 10^{-19} to 10^{-21} ss^{-1}. Their estimated ages and magnetic field strengths mostly range from 10^9 to 10^{10} years and 10^8 to 10^9 G respectively. Millisecond pulsars are thought to be old pulsars that have been 'spun up' due to accretion of matter from a companion star. For this reason, millisecond pulsars are also called recycled pulsars. Millisecond pulsars have also been observed in radio, optical light, X-rays and gamma rays. Figure 2–2 shows the period derivatives of the known pulsars plotted vs their periods: a P - $\dot{P}$ diagram. The young pulsars correspond to the population located at the top right of the diagram and millisecond pulsars correspond to the smaller population located at the bottom left.

In this chapter, the properties of rotation-powered pulsars will be discussed, with an emphasis on gamma-ray emission mechanisms and regions. First, the formation of pulsars will be discussed followed by a brief description of neutron stars. A magnetic dipole model for rotation powered pulsars will then be presented, which allows various pulsar parameters to be estimated. The basic picture of a pulsar magnetosphere will then be introduced, followed by a discussion of various radiation emission mechanisms and emission locations thought to be responsible for the observed electromagnetic radiation, including gamma rays.

2.2 Neutron stars

Neutron stars are thought to be the remnants of main sequence stars with masses between 8 and 25 solar masses ($M_\odot$). They consist of very dense compact objects composed primarily of neutrons, supported by neutron degeneracy pressure. Neutron

stars are formed in supernova explosions, which eject large amounts of the original stellar mass into space, creating a supernova remnant. For more information about the formation of neutron stars and other compact objects, see Appendix A. Neutron stars have a maximum mass above which the degeneracy pressure holding them up would be insufficient to prevent collapse. For neutron stars, this mass is thought to be between two and three $M_\odot$ [16]. Measurements from binary systems indicate that the masses of most pulsars are close to 1.4 $M_\odot$, ranging from 1.1 to 2 $M_\odot$ [104]. A canonical value of 1.4 $M_\odot$ is often used for for the purpose of estimating various quantities. Neutron star radii have been found to be between 9.9 and 11.2 km through spectroscopic measurements and pulse profile modelling [104]. A canonical value of 10 km is often used to estimate various quantities. The mass and radius values just described correspond to very high densities, close to that of an atomic nucleus. The gravitational field at the surface of a neutron star with a mass of 1.4 $M_\odot$ and a radius of 10 km is approximately 2×10^{11} times the gravitational force on the surface of the earth. The magnetic field at the surface of the neutron star is expected to be quite strong as well, assuming the magnetic flux is conserved as the core of the progenitor star collapses. Following a similar argument, neutron stars are expected to be rapidly rotating assuming angular momentum is conserved as the star collapses.

2.3 The magnetic dipole model

Many properties of rotation-powered pulsars may be deduced from their observed periods P and period derivatives $\dot{P}$, assuming a simple model in which a

pulsar consists of a rapidly rotating neutron star with a strong dipole magnetic field. These properties are briefly described below.

The energy of a rotating sphere of uniform density is given by $E_{rot} = \frac{1}{2} I\omega^2$, where ω is the angular velocity of the sphere and I is its moment of inertia. The rate of rotational energy loss, called the spin down luminosity, is given by:

$$\frac{dE_{rot}}{dt} = -I\omega\dot{\omega} = -4\pi^2 I\frac{\dot{P}}{P^3}$$

where $P = \frac{2\pi}{\omega}$. For the Crab pulsar, where $P = 0.033$ s and $\dot{P} = 4.2 \times 10^{13}\ ss^{-1}$, assuming a mass of 1.4 $M_\odot$ and a radius of 10 km, the spin down luminosity is approximately 5×10^{38} ergs/s. The power emitted by a rotating dipole is given by:

$$\frac{dE_{dip}}{dt} = -\frac{32\pi^5 B^2 R^6 \sin^2\theta}{3\mu_0 c^3 P^4}$$

where B is the magnetic field strength at the magnetic pole of the neutron star with a radius of R, θ is the angle between the rotation and dipole axes, c is the speed of light in a vacuum and μ_0 is the permeability of free space [15]. By equating the spin down luminosity with the energy emitted by a rotating dipole, $\frac{dE_{dip}}{dt} = \frac{dE_{rot}}{dt}$ and solving for the magnetic field, an expression for the magnetic field strength at the magnetic pole of the pulsar may be obtained:

$$B = \frac{1}{2\pi R^3 \sin\theta}\sqrt{\frac{3\mu_0 c^3 I P\dot{P}}{2\pi}}.$$

Using this formula with $\sin\theta = 1$ to estimate the magnetic field for the Crab pulsar gives an estimate of $B \sim 8 \times 10^{12}$ G. Assuming that the strength of the magnetic field is constant in time, the expression above may be re-arranged to show that $P\dot{P} = constant$, from which it can be shown that:

$$P\dot{P}\tau = \frac{P^2 - P_0^2}{2}.$$

Where τ and P_0 are the age and initial period of the pulsar respectively. Assuming that the initial period of the pulsar is much smaller than the current period, an estimate of the age of the pulsar may be obtained, called the dipole age:

$$\tau_{dip} \equiv \left(\frac{P}{2\dot{P}}\right).$$

Using the P and $\dot{P}$ values for the Crab pulsar, one obtains a dipole age of approximately 1240 years. The supernova associated with the Crab pulsar was observed in the year 1054, so the dipole age is close to the actual age of the Crab pulsar.

2.4 The pulsar magnetosphere

The previous description of a pulsar as a rotating neutron star with a strong dipole magnetic field assumes that the pulsar is surrounded by a vacuum. Goldreich and Julian first realized that in this case, strong electric fields induced by the rotation of the pulsar in the direction of the magnetic field lines would cause particles to be pulled from the surface, resulting in a plasma surrounding the pulsar. Assuming the plasma close to the pulsar slides freely along the magnetic field lines ($\vec{E} \cdot \vec{B} = 0$)

and co-rotates with the pulsar, they derived an expression for the charge density ρ_{GJ} of the co-rotating plasma [67]:

$$\rho_{GJ} = -\frac{\vec{\omega} \cdot \vec{B}}{(2\pi c)(1 - (\omega r/c)^2 \sin^2 \theta)}.$$

This expression was derived for the case of aligned rotation and magnetic dipole axes, where $\vec{\omega}$ is the angular velocity vector of the pulsar, r is the distance from the center of the pulsar and θ is the angle from the rotation axis. It can be seen from the expression for the Goldreich-Julian density that regions of zero charge density exist where $\vec{\omega} \cdot \vec{B} = 0$. These regions are called null lines. The null lines divide the magnetosphere into three regions. The regions near the poles of the pulsar have the same charge sign, and the region close to the equator of the pulsar has an opposite charge sign. The co-rotation of the plasma can only occur up to a maximum distance from the rotation axis of the pulsar, where the plasma would have to be moving at the speed of light in order to maintain co-rotation. This radius, $R_{LC} = \frac{c}{\omega}$ defines an imaginary boundary called the light cylinder. The plasma contained within the light cylinder is called the pulsar magnetosphere. The light cylinder defines two regions within the pulsar magnetosphere: a region where the magnetic field lines close within the light cylinder (closed magnetic field lines), and a region where the magnetic field lines cross the light cylinder (open magnetic field lines). The plasma moving along the closed magnetic field lines co-rotates with the pulsar and is confined to the light cylinder. The plasma moving along the open field lines is free to stream out of the light cylinder, creating a wind of charged particles beyond the light cylinder, called

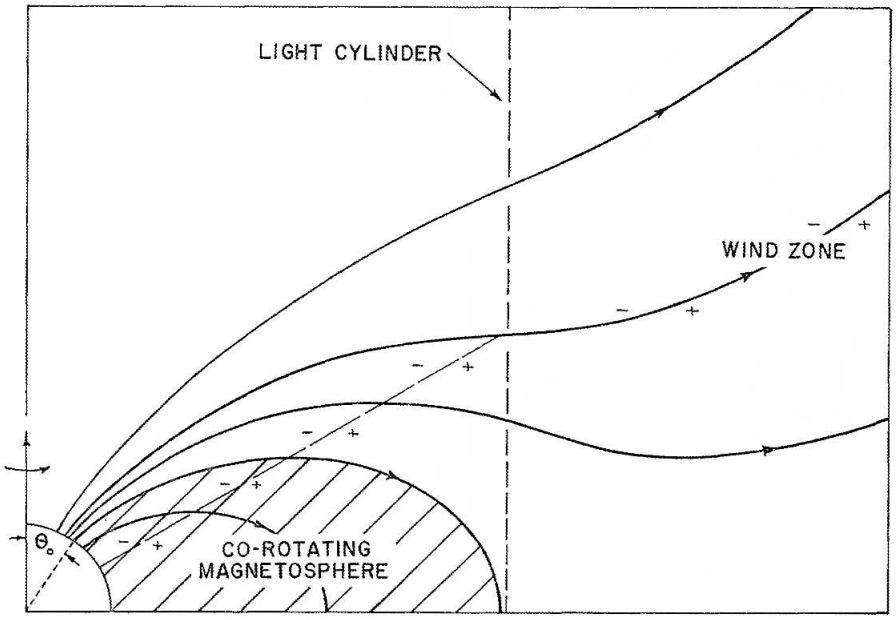

Figure 2–3: A diagram of the region surrounding a pulsar, showing the co-rotating magnetosphere, the light cylinder, a null line (the straight diagonal line, not labelled) and the wind zone. Figure modified from [67].

the wind zone [67]. Figure 2–3 shows a diagram of the region surrounding a pulsar, showing the co-rotating magnetosphere, the light cylinder, a null line (the straight diagonal line, not labelled) and the wind zone. This picture of a pulsar as a rotating neutron star with a strong dipole magnetic field, a co-rotating magnetosphere and wind zone is the basis upon which most pulsar models are founded.

2.5 Radiative emission from pulsars

The emission of electromagnetic radiation from rotation-powered pulsars is currently poorly understood. The radiation is thought to be powered by the rotation of the pulsar, but a consistent and satisfactory description of the the details of the emission processes remains elusive. The main open questions in the field are the nature of

the radiation emission mechanisms and the location of the emission regions. The luminosity of the radiation observed from pulsars at various wavelengths has provided some insight regarding the emission mechanisms. The observed high luminosity of the radio emission requires that it be produced by coherent processes, such as the coordinated motion of charges, maser emission or relativistic plasma emission [84]. The nature of the radio emission is the least understood aspect of radiative emission from pulsars, and is beyond the scope of this thesis. The luminosity of the optical, X-ray and gamma-ray emission is consistent with incoherent processes involving individual charged particles [110]. The incoherent processes are generally thought to consist of inverse Compton scattering, cyclotron radiation, synchrotron radiation and curvature radiation [84], which are described in section 2.6. Pair production on strong magnetic fields, which may limit the energy of the emitted photons, is discussed in section 2.7. Finally, proposed locations for the radiation emission regions are described in section 2.8.

2.6 Pulsar radiation emission mechanisms

This section describes the radiation mechanisms thought to be responsible for the optical, X-ray and gamma-ray emission from pulsars: inverse Compton scattering, cyclotron radiation, synchrotron radiation and curvature radiation.

Compton scattering refers to the scattering of a photon by a charged particle (usually an electron, which is assumed here), where the photon transfers some of its energy to the electron. This results in an increase in the kinetic energy of the electron and the wavelength of the photon. Similar to Compton scattering, inverse Compton scattering refers the scattering of a high energy photon by an electron,

where the electron transfers energy to the photon. This results in a decrease in the kinetic energy of the electron and the wavelength of the photon. Inverse Compton scattering occurs in astrophysical contexts, where high energy electrons up-scatter low energy photons into the gamma-ray regime. For a population of electrons following a power-law energy distribution up-scattering a low energy photon field, the resulting distribution of up-scattered photons also follows a power law [109]. For more information regarding Compton scattering and inverse Compton scattering, see Appendix B.1.

When a non-relativistic charged particle moves in a magnetic field, it spirals around the magnetic field lines due to the Lorentz force, emitting electromagnetic radiation called cyclotron radiation. For a particle moving perpendicular to the magnetic field lines, the frequency ν_L with which the particle moves around the magnetic field lines (called the Larmor frequency) is given by:

$$\nu_L = \frac{qB}{2\pi m}$$

where B is the strength of the magnetic field, and q and m are the charge and mass of the particle respectively. The cyclotron radiation emitted by the charged particle is polarized, and emitted at the Larmor frequency. For more information about cyclotron radiation, see Appendix B.2.

When a relativistic charged particle moves in a magnetic field, the particle spirals about the magnetic field lines, emitting radiation over a wide range of frequencies, called synchrotron radiation. Due to the relativistic beaming of light, the emission is

beamed in a cone in the direction of motion of the particle. The frequency spectrum of the emitted radiation peaks at approximately $\nu_{max} \sim 0.29\nu_C$, with

$$\nu_c = \frac{3\gamma^2 qB}{4\pi m} \sin\alpha$$

where α is the angle of the trajectory of the particle with respect to the magnetic field lines, and γ is the Lorentz factor [110]. The spectrum is proportional to $\nu^{\frac{1}{3}}$ below ν_{max} and $\exp[-(\frac{\nu}{\nu_c})]$ above ν_c. The shape of the synchrotron radiation spectrum produced by a population of charged particles depends on the shape of the energy spectrum of the charged particles. For example, the synchrotron radiation spectrum emitted by a population of charged particles with a power law energy distribution is also a power law [110]. Like cyclotron radiation, synchrotron radiation photons are highly polarized. For more information about synchrotron radiation, see Appendix B.3.

When a relativistic charged particle moves in a very strong magnetic field, the motion perpendicular to the magnetic field lines may be rapidly damped by synchrotron radiation losses, causing the particle to move along the magnetic field lines. Like synchrotron radiation, the emission is beamed in a cone in the forward direction. The motion of the charged particle along the curved magnetic field lines causes the particle to radiate electromagnetic radiation called curvature radiation in a manner similar to synchrotron radiation [110] [85]. The single particle spectrum is the same as for synchrotron radiation, with

$$\nu_c = \frac{3\gamma^3 c}{4\pi\rho}$$

where ρ is the radius of curvature of the magnetic field lines. Like synchrotron radiation, the photon spectrum produced by a population of charged particles with a power law energy distribution is also a power law. Due to the strong magnetic fields associated with pulsars, many models of pulsar gamma ray emission invoke curvature radiation as the dominant emission mechanism [95] [107] [13] [10] [30]. In these models, charged particles are accelerated in gaps in the plasma (see section 2.8) by electric fields with components in the direction of the magnetic field lines. The particles accelerated in the gaps have a maximum energy, which is attained when the rate of energy gained by the particles due to the electric field is equal to the power emitted via curvature radiation, called the radiation reaction limit. The maximum charged-particle energy leads to a break in the emitted photon spectrum, above which the photon spectrum falls off exponentially [10]. Such a spectral feature is called an exponential cutoff, and is predicted by models that invoke curvature radiation as the primary gamma-ray emission mechanism from pulsars. For pulsar emission scenarios involving curvature radiation, the measured maximum energy of the emitted photons may be related to the distance of the emission region above the surface of the pulsar [10]. For more information about curvature radiation, see Appendix B.4.

2.7 Pair production on strong magnetic fields

Due to the strong magnetic fields in the vicinity of pulsars, high-energy photons in the pulsar magnetosphere may undergo pair production: $\gamma_B + \gamma_{HE} \rightarrow e^+ + e^-$. The produced pairs may radiate additional photons which produce further pairs, resulting in a cascade of secondary photons and pairs, called secondary pair plasma.

This process may limit the maximum energy of the photons that escape the pulsar magnetosphere. For pulsar gamma-ray emission models with emission regions close to the surface of the pulsar (see section 2.8), high-energy photons are expected to undergo significant pair production due to the strong magnetic field. These models predict breaks in the photon spectrum, with super-exponential cutoffs above the break energy [10] [9]. For a given pulsar, the maximum measured photon energy may be used to constrain the minimum height of the gamma ray emission region above the surface of the pulsar [9]. For more information about pair production on strong magnetic fields, see Appendix B.5.

2.8 Pulsar radiation emission regions

Standard pulsar radiation emission models require the acceleration of charged particles within the pulsar magnetosphere; these particles then emit the observed electromagnetic radiation via inverse Compton scattering, synchrotron radiation and curvature radiation. Within the magnetospheric plasma defined by Goldreich and Julian, electric field components in the direction of the magnetic field lines, required to accelerate the charged particles, are screened. However, regions where the plasma density is depleted relative to the Goldreich-Julian density may develop, called gaps. In the gaps, unscreened electric field components in the direction of the magnetic field lines (caused by the changing magnetic field) allow the acceleration of charged particles, which emit the observed electromagnetic radiation. As the pulsar makes a complete rotation, the intensity of the observed radiation is modulated according to the geometry of the gap locations and the line of sight of the observer, resulting in

the observed characteristic pulsed signal. Several proposed locations for these gaps are described below.

2.8.1 Polar cap

The polar cap model postulates magnetospheric gaps directly above the surface of the pulsar, at the region of the magnetic poles defined by the open magnetic field lines. In these gaps, charged particles may be accelerated by powerful electric fields with components parallel to the magnetic field lines. These particles may reach relativistic energies, producing gamma-ray photons via curvature radiation; these photons then pair produce due to the strong magnetic field near the surface of the pulsar. The pairs then create further gamma-ray photons, leading to a cascade of photons and pairs, creating a secondary pair plasma. The maximum height of the gap above the surface of the neutron star is determined by the distance required for the charged particles to accelerate to the energies required to emit curvature radiation energetic enough for pair production. Coherent processes involving the pair plasma are believed to be the source of the radio emission [84]. The incoherent emission, associated with the observed electromagnetic radiation at other wavelengths, is thought to be produced via synchrotron radiation, curvature radiation and inverse Compton scattering processes involving the primary accelerated particles and the pair plasma. The observed pulse profile is thought to be a consequence of the polar cap region(s) becoming visible at certain rotational phases of the pulsar. As mentioned in section 2.6 and Appendix B.5, the pair cascade process may limit the maximum energy of the high energy photons that can escape the pulsar magnetosphere. For gamma-ray emission scenarios involving emission regions close to the

surface of the pulsar such as the polar cap model, high-energy photons are expected to undergo significant pair production due to the strong magnetic field. This limits the maximum energy of the photons that can escape the pulsar magnetosphere, leading to a break in the observed photon spectrum, with a super-exponential cut-off above the break energy [10] [9]. Polar cap models were originally developed by Sturrock (1971) [113] and Ruderman and Sutherland (1975) [108], and have been extended by others [84].

2.8.2 Slot gap

The slot gap model, first proposed in 1979 [7], can be thought of as an extension to the polar cap model. In the slot gap model, the gap forms over the magnetic poles of the pulsar like in the polar cap model, but the electric field is weakened near the edge of the last open field lines. This results in larger distances required to accelerate the particles to the energies required to emit curvature photons capable of pair producing, causing the pair formation front to extend far away from the pulsar near the last open field lines. Figure 2–4 shows the resulting 'hollow cone' slot gap geometry. The slot gap may extend all the way to the light cylinder where the magnetic field strength is weaker than near the surface of the pulsar, allowing high-energy photons to escape the magnetosphere without undergoing significant pair production. As in the polar cap model, the radio emission is thought to originate from coherent processes involving the pair plasma, and the incoherent emission is thought to involve synchrotron radiation, curvature radiation and inverse Compton scattering [74]. The slot gap model was first proposed by Arons (1979) [7], and has been extended by others [94] [72] [74].

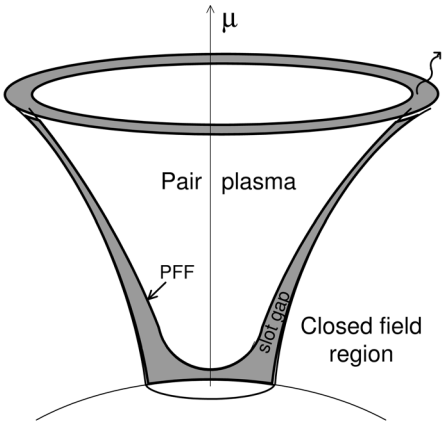

Figure 2–4: Slot gap geometry, where μ is the magnetic dipole axis of the pulsar. The electric field near the last open field lines is weaker than at the poles, resulting in the pair formation front (PFF) extending to higher altitudes, forming a 'hollow cone' gap geometry. See text for details. Figure modified from [72].

2.8.3 Outer gap

The outer gap model involves acceleration gaps located in the region bounded by the light cylinder, the last closed magnetic field lines, and the null lines, defined by $\vec{\omega} \cdot \vec{B} = 0$. As the pulsar spins, the radiation is emitted perpendicular to the last closed magnetic field lines in a fan like geometry. In outer gap models, the radio emission is expected to be produced in the polar cap region by coherent processes involving the pair plasma. The incoherent radiation emission mechanisms, as in the previously mentioned gap models, are assumed to involve synchrotron radiation, curvature radiation and inverse Compton scattering. As in the slot gap model, the location of the emission region close to the light cylinder where the magnetic field strength is weaker than near the surface of the pulsar, allows high energy photons to escape the magnetosphere without undergoing significant pair production. The outer gap model was first proposed by Cheng, Ho and Ruderman (1986) [17] [18], and extended by others [107].

2.8.4 Summary and new models

Figure 2–5 shows the main features of the standard pulsar models described in the text: a rapidly rotating, highly magnetized neutron star with a dipole magnetic field surrounded by a co-rotating plasma. Charged particles are accelerated and radiate electromagnetic radiation in one or more gaps in the plasma. The three gap location scenarios discussed in the literature (the polar cap, slot gap and outer gap regions) are shown in the figure. These models constitute the standard paradigm of radiative emission from pulsars. In these models, curvature radiation is thought to be the mechanism responsible for the gamma-ray emission, predicting

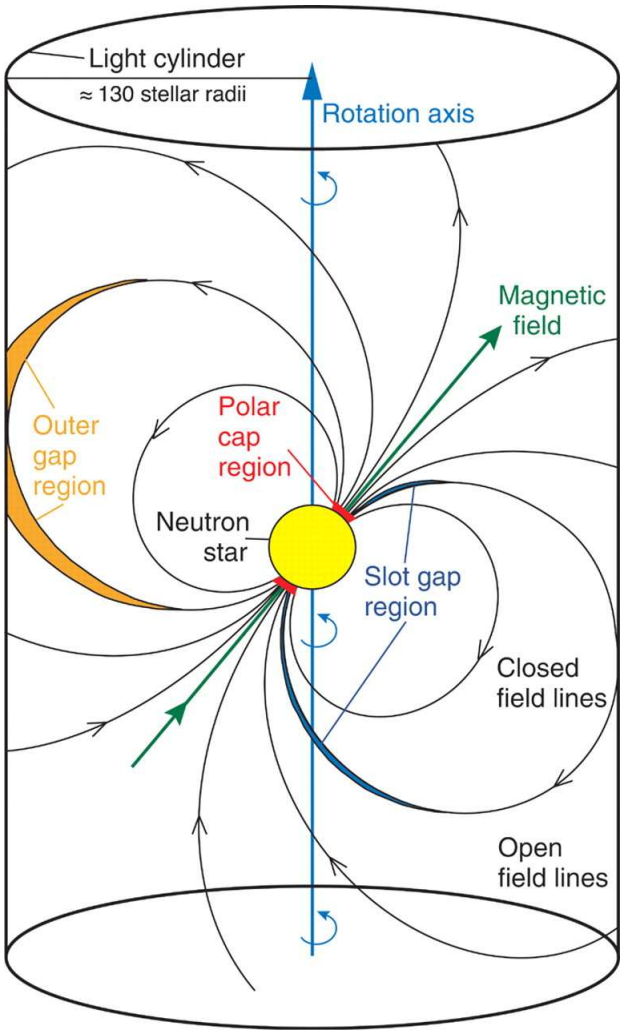

Figure 2–5: A diagram showing the main features of the standard pulsar models described in the text: a rapidly rotating, highly magnetized neutron star with a dipole magnetic field surrounded by a co-rotating plasma. Charged particles are accelerated and radiate electromagnetic radiation in one or more gaps in the plasma. The three gap location scenarios discussed in the literature, the polar cap, slot gap and outer gap regions are shown (see section 2.8 for details). The null lines, where the plasma density is zero (not shown) occur where $\vec{\omega} \cdot \vec{B} = 0$, the points at which the magnetic field lines are perpendicular to the rotation axis. The light cylinder, where the co-rotating plasma would be moving at the speed of light, is also shown, with the distance calculated for the Crab pulsar. Figure from [37].

exponential cutoffs in the spectra below 100 GeV for slot gap and outer gap scenarios [95] [107] [13] [30]. Polar cap models predict super-exponential cutoffs in the gamma ray spectra due to pair production near the surface of the pulsar [10] [9]. The spectra of the pulsars discovered by the Fermi gamma ray space telescope all exhibit spectral breaks at several GeV, and may be fit with power laws with exponential cutoffs (see section 3.1), consistent with curvature radiation emission from the slot gap or outer gap regions [30]. In 2011, VERITAS detected the Crab pulsar at energies above 100 GeV, favouring a broken power law spectral fit over a power law with an exponential cutoff, a result inconsistent with the curvature radiation emission scenario [38]. MAGIC has since detected the Crab pulsar at energies of up to 1.5 TeV [54]. In light of these results (see section 3.1), new models invoking alternative emission scenarios were proposed in order to explain the gamma-ray emission from the Crab and possibly other pulsars.

Several models were proposed involving inverse Compton scattering in the magnetospheric gaps within the light cylinder. Lyutikov et al. (2012) proposed a synchrotron self-Compton (SSC) model broadly consistent with the Crab pulsar observations, where synchrotron-emitting secondary pair plasma in the outer gap upscatters the synchrotron photons to high energies in the Klein-Nishina regime [87]. The MAGIC collaboration fit the Crab spectrum with a model involving inverse Compton scattering in the outer gap [34] [35]. Lyutikov et al. (2013) [86] fit the Crab pulsar spectrum with an outer gap cyclotron self-Compton (CSC) model, shown in Figure 2–6 (left). Hirotani (2015) presented an outer gap SSC model where very young pulsars are able to produce strong pulsed TeV emission and characteristic

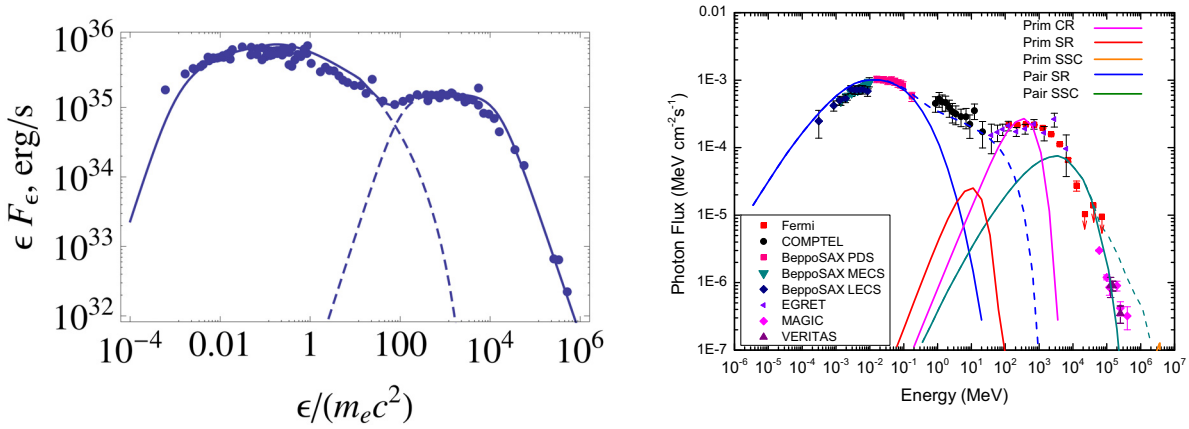

Figure 2–6: Magnetospheric gap models involving inverse Compton scattering proposed in light of the discovery of emission above 100 GeV from the Crab pulsar. Left: the Crab pulsar spectrum fit with an outer gap cyclotron self-Compton model by [86]. Right: the Crab pulsar spectrum fit with a slot gap synchrotron self-Compton model by [73].

double-peaked light curves [77]. Harding et. al (2015) [73] fit the Crab pulsar spectrum with a slot gap SSC model, shown in Figure 2–6 (right).

Several other models were proposed involving radiative emission from the wind zone, beyond the light cylinder. Aharonian et al. (2012) [4] proposed a model invoking a new radiation component at VHE energies in order to explain the detection of the Crab pulsar above 100 GeV. The new component involves inverse Compton scattering of magnetospheric photons by ultra-relativistic wind particles accelerated beyond the light cylinder. Figure 2–7 (left) shows the gamma-ray spectrum of the Crab pulsar, with power law with exponential cutoff fits (grey lines) to the FERMI

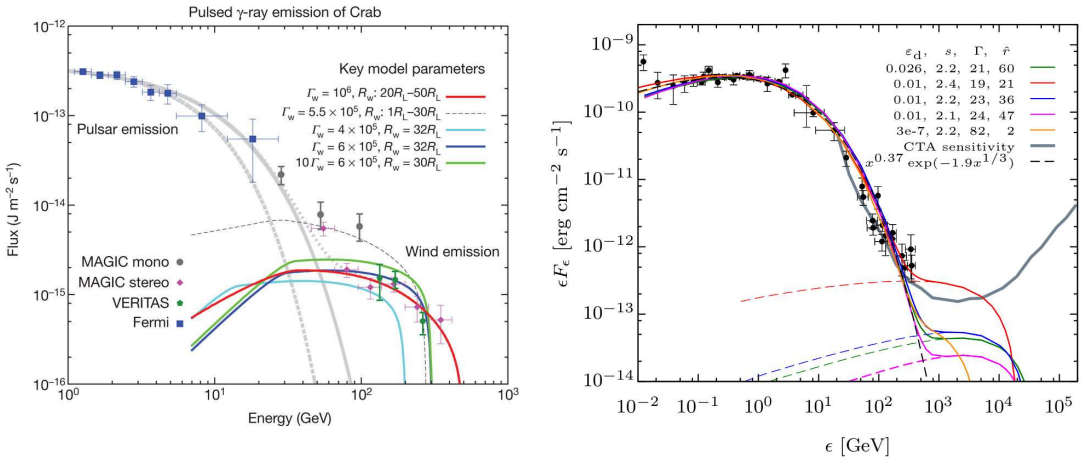

Figure 2–7: Models involving radiative emission from the wind zone beyond the light cylinder proposed in light of the discovery of emission above 100 GeV from the Crab pulsar. Both of the models combine two spectral components in order to explain the gamma-ray emission from the Crab pulsar. Left: A model proposed by Aharonian et al. (2012) [4] invoking a new radiation component at VHE energies consisting of inverse Compton scatting of magnetospheric photons by ultra-relativistic wind particles accelerated beyond the light cylinder. The grey lines are power law with exponential cutoff fits to the FERMI data, consistent with the magnetospheric curvature radiation scenario, and the coloured lines represent the inverse Compton emission for various model parameters. Right: A model proposed by Mochol and Petri (2015) [93] postulating that synchrotron and synchrotron self-Compton (SSC) radiation from particles accelerated by magnetic reconnection in the wind zone is responsible for the observed gamma-ray emission from the Crab and Vela pulsars. The solid coloured lines correspond to the total (synchrotron + SSC) emission and the dashed coloured lines correspond to the SSC components.

data points, consistent with the magnetospheric curvature radiation scenario, and the inverse Compton emission from the wind zone (coloured lines) for various parameters of the model. This model successfully fits the Crab pulsar spectrum up to approximately 400 GeV and reproduces the observed gamma-ray pulse profile, but is inconsistent with the new results from MAGIC [54], where the spectrum has been observed to follow a power law up to approximately 1.5 TeV (see section 3.1). Petri et al. (2012) [105] and Arka and Dubus (2013) [6] proposed models where the gamma-ray emission of the FERMI pulsars is explained as synchrotron radiation originating from particles in the wind zone. Petri et al. invoke an inverse Compton component in order to explain the VHE emission from the Crab pulsar. Mochol and Petri (2015) [93] [92] proposed a model postulating that synchrotron and synchrotron self-Compton (SSC) radiation from particles accelerated by magnetic reconnection in the wind zone are responsible for the observed gamma-ray emission from the Crab and Vela pulsars. Figure 2–7 (right) shows the spectrum of the Crab pulsar as measured by FERMI and MAGIC, fit with the SSC model for various model parameters. The solid coloured lines correspond to the total (synchrotron + SSC) emission and the dashed coloured lines correspond to the SSC components.

Given the multiplicity of models, it is clear that consensus on a single theory of radiative emission from pulsars remains elusive.

CHAPTER 3
Gamma-ray pulsar astronomy

3.1 Introduction

This chapter briefly summarizes the field of gamma-ray pulsar astronomy, describing observations of gamma-ray pulsars, and some of the theoretical implications of the observations. Space-based gamma-ray pulsar astronomy will first be described, followed by ground-based gamma-ray pulsar astronomy. In order to detect pulsations from gamma-ray pulsars, where the gamma-ray detection rate is often quite low, a pulsar rotational phase must be assigned to the detected photons. In order to accomplish this, the arrival times of the photons are converted to the arrival times that would have been recorded at the center of mass of the solar system, a process called barycentering. These times are then used to assign a rotational phase to each photon in a process called phase folding. Phase folding requires a pulsar timing solution, which includes the measured period and one or more period derivatives corresponding to a particular time, the location of the pulsar and other parameters. Timing solutions may be made using observations at other wavelengths, or directly from the gamma-ray data. The latter technique involves scanning over the pulsar parameters, and is therefore less sensitive due to the multiple trials incurred. Once the phases of the photons have been determined, pulsars may be detected by discovering deviations from uniformity in the phase profiles. For more information regarding

barycentering, phase folding, and methods for the detection of non-uniformities in the phase profiles, see section 5.15.

3.1.1 Space-based gamma-ray pulsar astronomy

This section briefly describes pulsar observations by space-based gamma ray observatories, and presents some theoretical implications of the observations. As mentioned in the introduction, gamma-ray pulsations were first discovered from the Crab pulsar by the SAS-2 satellite in 1974 [43]. The second gamma-ray pulsar discovered, the Vela pulsar, was also discovered by SAS-2, in 1975 [119]. COS-B confirmed the Crab and Vela detections, but did not detect any new gamma-ray pulsars. The Crab and Vela pulsars remained the only known gamma-ray pulsars until the Compton gamma-ray observatory (CGRO) detected five new pulsars, in addition to the Crab and Vela, between 1991 and 2000. The phase profiles of the pulsars detected by the CGRO are shown in Figure 3–1. The new pulsars discovered by the CRGO included the first discovered radio-quiet gamma-ray pulsar: Geminga, in 1992 [42]. The measured spectra of the CGRO pulsars were unable to constrain the location of the emission region [117]. AGILE went online in 2007, and discovered three new gamma-ray pulsars early in the mission [47] [53].

The Fermi gamma-ray space telescope was launched in 2008, and in 2010 the LAT team published the first Fermi Large Area Telescope catalogue of gamma-ray pulsars (1PC). The catalogue consisted of 46 gamma-ray pulsar sources detected during the first six months of operations, including six of the pulsars detected by the CGRO, and two of the pulsars discovered by AGILE [29]. 24 of the newly detected pulsars were discovered using timing solutions obtained from observations at other

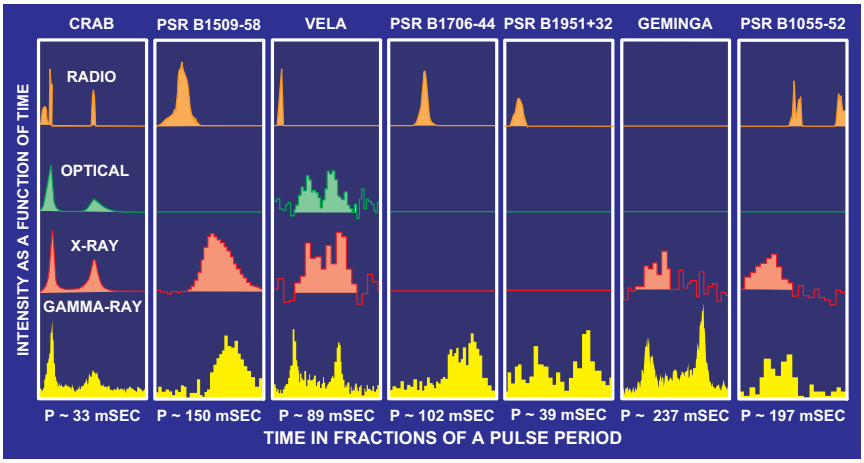

Figure 3–1: The phase profiles of the seven gamma ray-pulsars detected by the Compton Gamma Ray Observatory (CGRO), which operated from 1991 to 2000. In addition to the Crab and Vela pulsars which had been previously detected (see text for details), CGRO discovered five additional gamma-ray pulsars. The new pulsars included Geminga, the first radio quiet gamma-ray pulsar. Figure from [98].

wavelengths and 16 were discovered from the gamma-ray data alone using blind period searches. Eight of the pulsars were millisecond pulsars (MSPs), a new class of gamma-ray pulsar. Most of the pulse profiles were observed to have two peaks, separated by approximately 0.2 in phase, with broad single peaks also seen. These pulse profiles are mostly consistent with outer gap and slot gap scenarios, with the polar cap gamma-ray emission scenarios possible for only a few of the light curves. The phases of the radio and the gamma-ray pulses were mostly found to be non-aligned, consistent with what was seen for the CGRO pulsars, suggesting different emission regions for the radio and gamma-ray emission. The spectra of the pulsars were found to be consistent with power laws with exponential cutoffs, with cutoff energies between 1 and 5 GeV, consistent with the outer gap and slot gap curvature

radiation gamma-ray emission scenarios. No super-exponential cutoffs were seen in the spectra, challenging polar cap gamma-ray emission scenarios.

In 2013, the LAT team published the second Fermi Large Area Telescope catalogue of gamma-ray pulsars (2PC), a catalogue of 117 gamma-ray pulsar sources which included all of the pulsars published in the 1PC [30]. The catalogue covers three years of observations, from August 4, 2008 to August 4, 2011. The catalogue is made up of 42 young radio-loud pulsars, 35 young radio-quiet pulsars, and 40 millisecond pulsars (all of which are radio-loud). 61 of the pulsars were detected by phase folding known pulsars with timing solutions obtained from observations at other wavelengths. 36 were detected using blind period searches, and 20 were discovered after radio observations of unidentified LAT sources discovered pulsations and timing solutions were produced that allowed the LAT data to be folded. Seven of the 2PC pulsars have been identified at optical, UV or IR wavelengths, and 67 have been associated with non-thermal x-ray sources. All of the pulsars in the catalogue were found to be rotation-powered pulsars, with no accretion-powered pulsars or magnetars found. Figure 3–2 shows a P - $\dot{P}$ diagram of the pulsars in the 2PC catalogue. Figure 3–3 (left) shows the positions of the pulsars in the 2PC in the sky, and Figure 3–3 (right) shows their positions in the galaxy, derived from distance measurements (see [30] for details). Most of the 2PC pulsars are double-peaked (75% for the young pulsars and 60% for the MSPs) with some showing 'bridge emission' in between the two peaks. Most of the other pulsars have one peak, and two of the pulsars (including Vela) exhibit a third peak. As in the 1PC, the phases of the radio and the gamma-ray pulses were mostly found to be non-aligned. Many of the pulse

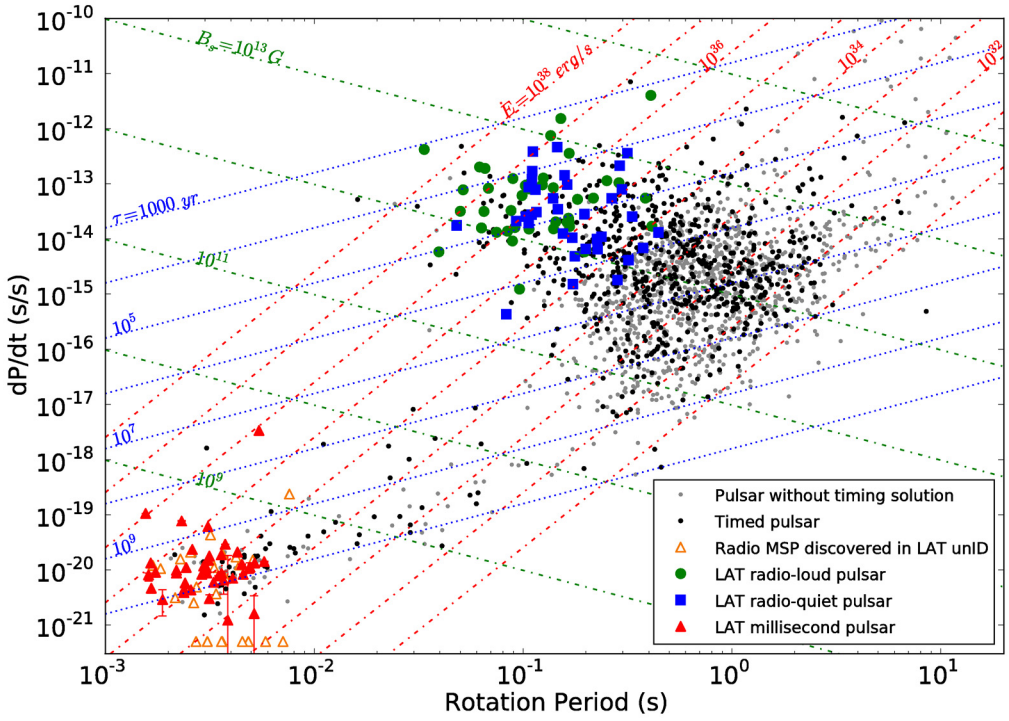

Figure 3–2: A P - $\dot{P}$ diagram showing the pulsars in the 2PC catalogue. The green dots represent the 42 young radio-loud pulsars, the blue squares represent the 35 young radio-quiet pulsars, and the red triangles represent the 40 MSPs. The black dots show known pulsars that were phase folded but not detected, and the grey dots indicate known pulsars that were not phase folded. Orange open triangles show radio MSPs detected at the positions of unidentified LAT sources. The red, green and blue dotted lines represent regions of constant spin down luminosity, magnetic field strength at the neutron star surface, and dipole age respectively. Figure from [30].

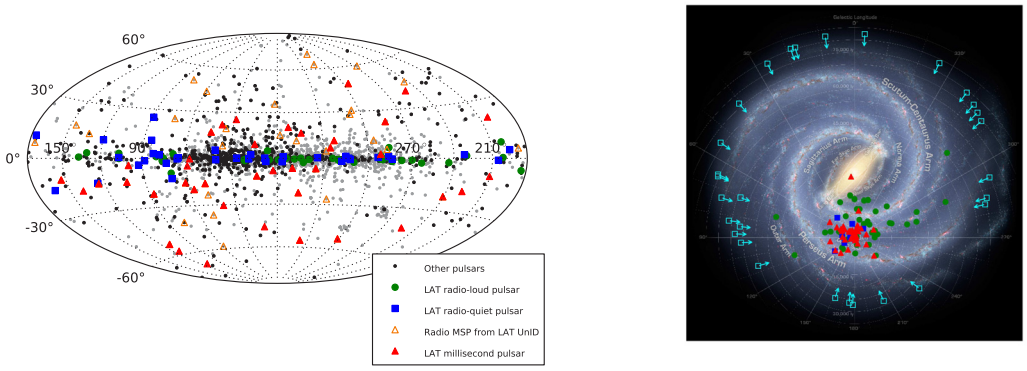

Figure 3–3: Left: An Aitoff projection showing the positions in the sky of the pulsars in the 2PC catalogue. Right: the locations of the 2PC pulsars in the galaxy. Figures from [30].

profiles may be explained by slot gap and outer gap models. However no model was able to explain all of the observations. The spectra of the 2PC pulsars were fit with power laws with exponential cutoffs of the form:

$$\frac{dN}{dE} = K\left(\frac{E}{E_0}\right)^{-\Gamma} \exp\left(-\frac{E}{E_{cut}}\right)^{b}$$

where K is a normalization constant, Γ is the spectral index at low energies, E_0 is the energy for which K is defined, E_{cut} is the cutoff energy, and b defines the steepness of the cutoff. Higher values of b correspond to steeper cutoffs. Values of $b > 1$ correspond to super-exponential cutoffs, and values of $b < 1$ correspond to sub-exponential cutoffs. The 2PC pulsar spectra were fit setting $b = 1$, called a PLEC1 fit, and fit leaving b as a free parameter, called a PLEC fit. The pulsars

were also fit with a power law (PL). For some pulsars, the PLEC1 model does not fit the data significantly better than the PL model. All of the pulsars show cutoff energies between 1 - 6 GeV, assuming $b = 1$, consistent with slot-gap and outer-gap curvature radiation gamma-ray emission scenarios. No super-exponential cutoffs are seen, challenging polar cap gamma-ray emission scenarios. In the cases where the PLEC model is favoured over the PLEC1 model, the value of b is found to be significantly less than 1, indicating a sub-exponential cutoff. This may indicate a new component at high energies for these pulsars, or that the assumption that curvature radiation is responsible for the gamma-ray emission is incorrect. Due to the limited high energy range of the LAT, it is difficult to distinguish between such scenarios using the LAT data alone. However, measurements of the pulsar spectra at higher energies with IACTs can help to distinguish between these scenarios. At the time of the writing of this thesis, the LAT has catalogued 205 gamma-ray pulsars, which includes all of the gamma-ray pulsars previously detected by other instruments [63].

3.1.2 Ground-based gamma-ray pulsar astronomy

This section briefly summarizes previous observations of gamma-ray pulsars with IACTs, presenting key results and some of the theoretical implications of the observations. As mentioned in section 3.1.1, IACTs may used to measure the high energy spectra of gamma-ray pulsars in order to distinguish between gamma-ray pulsar emission scenarios. Pulsars were first detected by an IACT by the MAGIC collaboration, which announced the detection of pulsed emission from the Crab pulsar above 25 GeV in 2008 [37]. Figure 3–4 (left) shows the pulse profiles of the Crab as measured by MAGIC above 25 and 60 GeV. The pulse profiles of the Crab pulsar determined

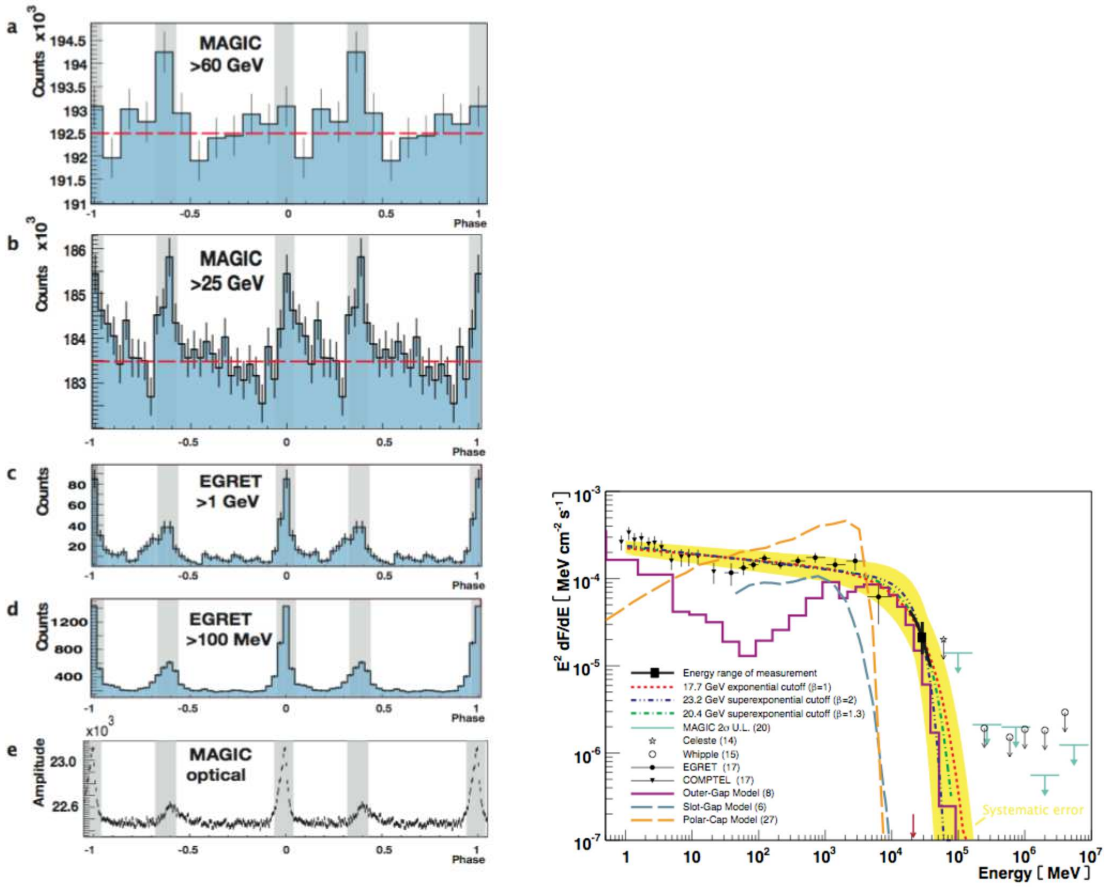

Figure 3–4: The MAGIC collaboration announced the detection of the Crab pulsar in 2008, the first detection of a pulsar by an IACT. Left: the pulse profiles of the Crab as measured by MAGIC above 25 and 60 GeV. The pulse profiles of the Crab as measured by EGRET aboard the CGRO are also shown, as is the optical profile as measured by MAGIC. Right: the spectrum of the Crab pulsar measured by various instruments, including the MAGIC spectral points. The spectrum is fit with an outer gap model, and presented a challenge for slot gap and polar cap models. Figures from [37].

by EGRET aboard the CGRO are also shown, as is the optical profile measured by MAGIC. Figure 3–4 (right) shows the spectrum of the Crab pulsar as measured by various instruments, including the MAGIC spectral points. The spectrum was fit with an outer gap model, and presented a challenge for slot gap and polar cap models.

VERITAS subsequently announced the detection of pulsed emission from the Crab above 100 GeV in 2011 [38]. Figure 3–5 (top) shows the pulse profile of the Crab as measured by VERITAS above 120 GeV. Figure 3–5 (bottom) shows the spectrum of the Crab pulsar as measured by various instruments. The red points are the VERITAS spectral points. A broken power-law fit (solid black line) was favoured over the power law with exponential cutoff fit (dashed black line) at approximately 5 σ. This challenged standard gamma-ray emission scenarios involving curvature radiation from the outer magnetosphere, leading to the proposal of new models, as described in section 2.8.4. The highest energy photons measured by VERITAS were used to constrain the height of emission to at least 10 km above the surface of the pulsar, as described in Appendix B.5.

The MAGIC collaboration announced the detection of the Crab pulsar up to 400 GeV in 2012 [35], and up to 1.5 TeV in 2015 [54]. Figure 3–6 (left) shows the pulse profile of the Crab as measured by MAGIC between 100 and 400 GeV (top) and above 400 GeV (bottom). Figure 3–6 (right) shows the Crab pulsar spectrum as measured by Fermi LAT and MAGIC, for each of the observed pulses. This result firmly rules out gamma-ray emission scenarios involving curvature radiation in the

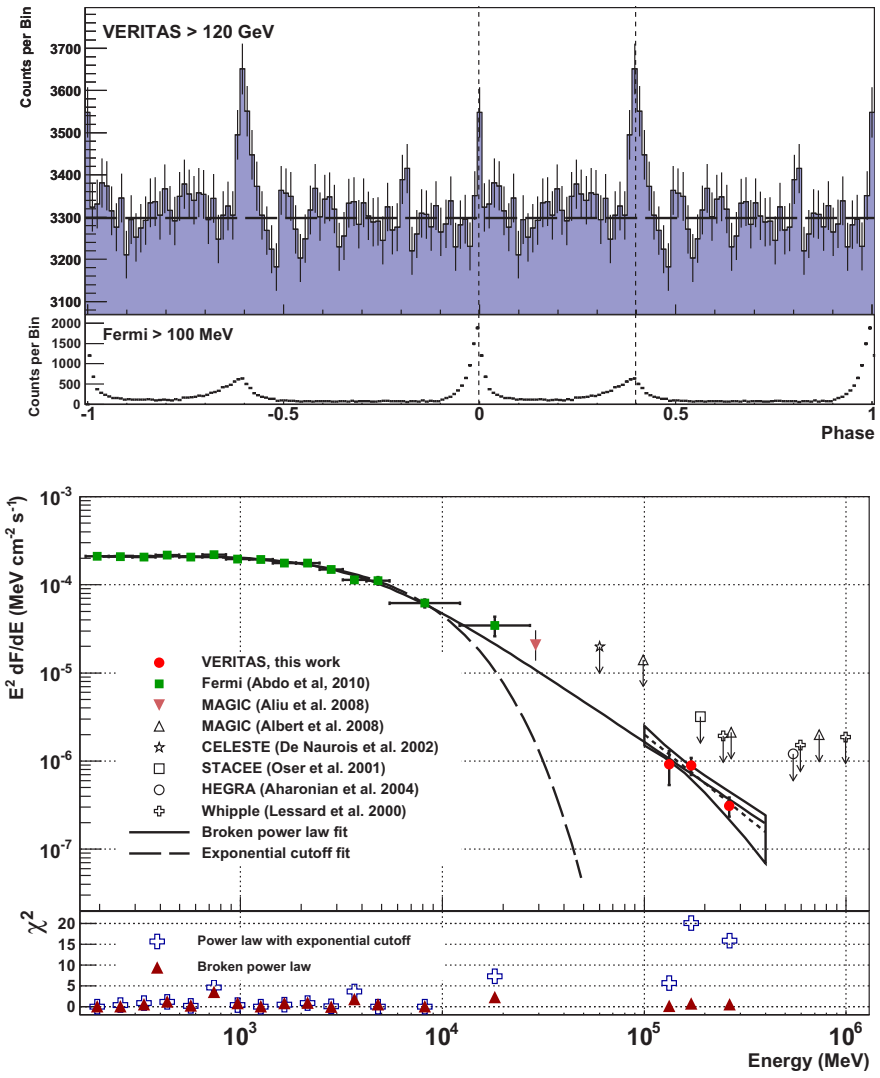

Figure 3–5: The VERITAS collaboration announced the detection of the Crab pulsar above 100 GeV in 2011 [38]. Top: the pulse profile of the Crab as measured by VERITAS above 120 GeV. Bottom: the spectrum of the Crab pulsar as measured by various instruments. The red points are the VERITAS spectral points. A broken power law fit (solid black line) was favoured over the power law with exponential cutoff fit (dashed black line) at approximately 5 σ challenging standard emission scenarios involving curvature radiation from the outer magnetosphere. Figures from [103].

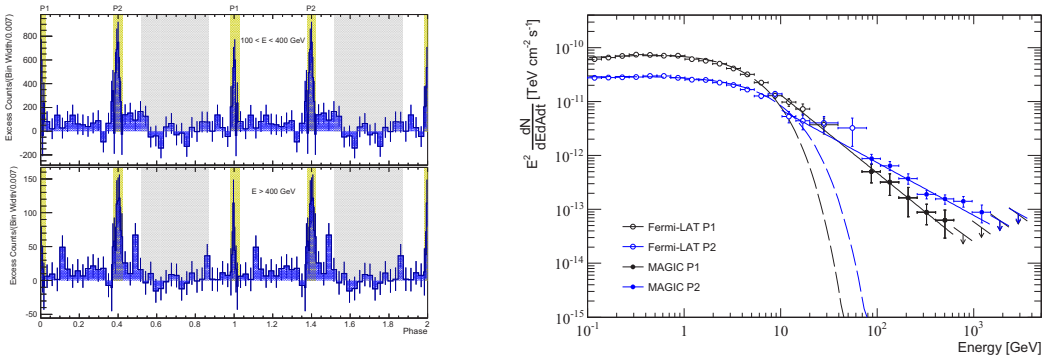

Figure 3–6: The MAGIC collaboration announced the detection of the CRAB pulsar up to 1.5 TeV in 2015 [54]. Left: the pulse profile of the Crab as measured by MAGIC between 100 and 400 GeV (top) and above 400 GeV (bottom). Right: the Crab pulsar spectrum as measured by Fermi LAT and MAGIC, for each pulse. Figures from [54].

outer magnetosphere, suggesting inverse Compton emission scenarios. The MAGIC collaboration announced the detection of bridge emission from the Crab in 2014 [111].

In 2014, the HESS collaboration announced the detection of the Vela pulsar between 20 and 120 GeV, increasing the catalogue of pulsars detected by IACTs to two [44]. Figure 3–7 (top) shows the pulse profile of the Vela pulsar as measured by HESS (top), as well as the pulse profile measured by Fermi LAT (bottom). Figure 3–7 (bottom) shows the Vela pulsar spectrum as measured by Fermi LAT and HESS. The measured spectrum favoured a power law with exponential cutoff fit over a power law fit at 2.7 σ, consistent with gamma-ray emission scenarios involving curvature radiation from the outer magnetosphere. In 2017, the HESS collaboration announced preliminary results indicating the detection of the Vela pulsar at energies above 7 TeV [2]. This result may indicate a new component at TeV energies.

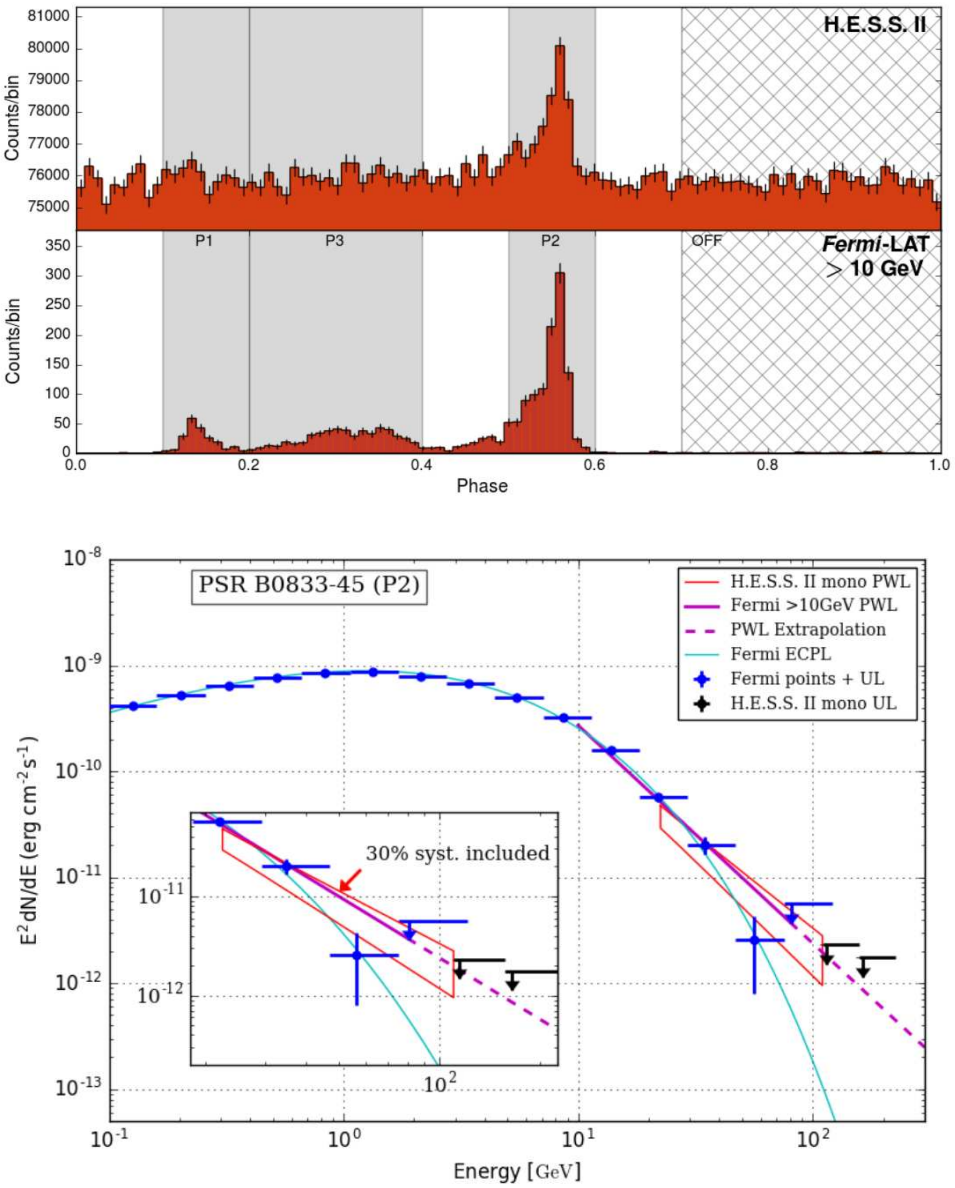

Figure 3–7: The HESS collaboration announced the detection of the Vela pulsar between 20 and 120 GeV in 2014 [44]. Top: the pulse profile of the Vela pulsar as measured by HESS (top), as well as the pulse profile measured by Fermi LAT (bottom). Bottom: the Vela pulsar spectrum as measured by Fermi LAT and HESS. Figures from [44].

VERITAS and MAGIC observed the Geminga pulsar, but did not detect significant pulsations [39] [5]. Upper limits were calculated that constrained possible hardening of the spectrum at GeV energies. VERITAS also observed PSR J1023+0038, but did not detect significant pulsations [65].

3.2 The VERITAS archival Fermi pulsar search

As mentioned in the previous section, the Crab and Vela pulsars are currently the only pulsars detected at VHE energies. The detection of the pulsars at these energies challenges standard pulsar gamma-ray emission scenarios involving curvature radiation from the outer magnetosphere. However, the spectra of most of the Fermi pulsars is consistent with these emission scenarios. The VERITAS archival pulsar search, the subject of this thesis, was undertaken in order to increase the number of pulsars detected at VHE energies, and to determine if more Fermi pulsars show indications of non-standard gamma-ray emission scenarios as described in section 2.8.4. In the case of a detection, measurements of the pulse profile and the shape of the spectrum would allow constraints to be placed on the gamma-ray emission scenarios. In the case of an MSP detection, constraints on Lorentz-invariance violation would also be possible. For non-detections, the best VHE upper limits would be obtained, constraining gamma-ray emission scenarios. Non-detections would also help with planning observations of these sources with the Cherenkov Telescope Array, currently being built.

The VERITAS archival pulsar search selected observing runs from archival VERITAS data where pulsars in the 2PC catalogue were observed directly, or present in the field of view. This search yielded 15 2PC pulsars after discarding pulsars with

no available timing solutions valid for the times the data was taken on them and pulsars where a VHE pulsar analysis had been previously performed. These pulsars were then analyzed to look for pulsed emission. The details of the VERITAS archival pulsar analyses and results are described in Chapter 6.

CHAPTER 4
IACTs and VERITAS

4.1 Introduction

This chapter describes the imaging atmospheric Cherenkov technique, and the details of the VERITAS array of imaging atmospheric Cherenkov telescopes. Cosmic rays and the particle cascades (electromagnetic and hadronic) that they create in the atmosphere called air showers are first described. A description of Cherenkov light is then presented, and the imaging atmospheric Cherenkov technique - the operating principle behind the VERITAS telescopes - is discussed. Finally, a detailed description of the VERITAS array of imaging atmospheric Cherenkov telescopes is given. The details of the VERITAS data analysis procedures are presented in the next chapter.

4.2 Cosmic rays and air showers

Cosmic rays were discovered in 1912, when Victor Hess brought an ionization detector on a balloon flight (see Figure 4–1 (left)). The purpose of this flight was to investigate the nature of a persistent ionizing radiation that had been detected at ground level. Specifically, the flight was undertaken in order to test the assumption that the radiation was terrestrial in origin. It was expected that the ionization rate measured by the detector would decrease with altitude if this assumption was correct. Instead, it was found that the ionization rate measured by the detector increased with altitude. Based on this result, it was concluded that the radiation

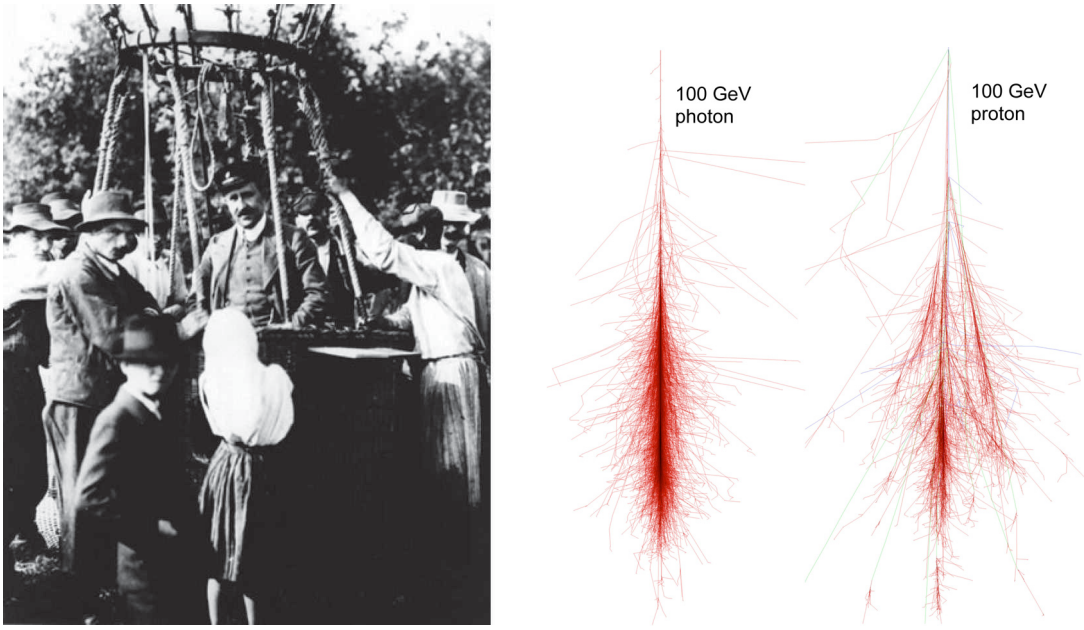

Figure 4–1: Left: Victor Hess discovered cosmic rays in 1912. Right: Simulations of photon and proton initiated air showers [79]. See text for details.

was extraterrestrial in origin. It is now known that this ionizing radiation consists of secondary particles created in particle cascades called air showers initiated by extraterrestrial high-energy particles called cosmic rays.

Air showers fall into two categories: electromagnetic and hadronic showers. Electromagnetic showers are initiated by photons, electrons and positrons and involve only electromagnetic interactions. Photon primaries interact with virtual photons emitted by the nuclei of atoms in the atmosphere, resulting in electron-positron pair production. The electron-positron pair produce additional photons via bremsstrahlung, which themselves pair produce. This process continues, forming a cascade of particles composed almost entirely of electrons, positrons and photons. When the average energy of the particles in the shower falls below the critical energy

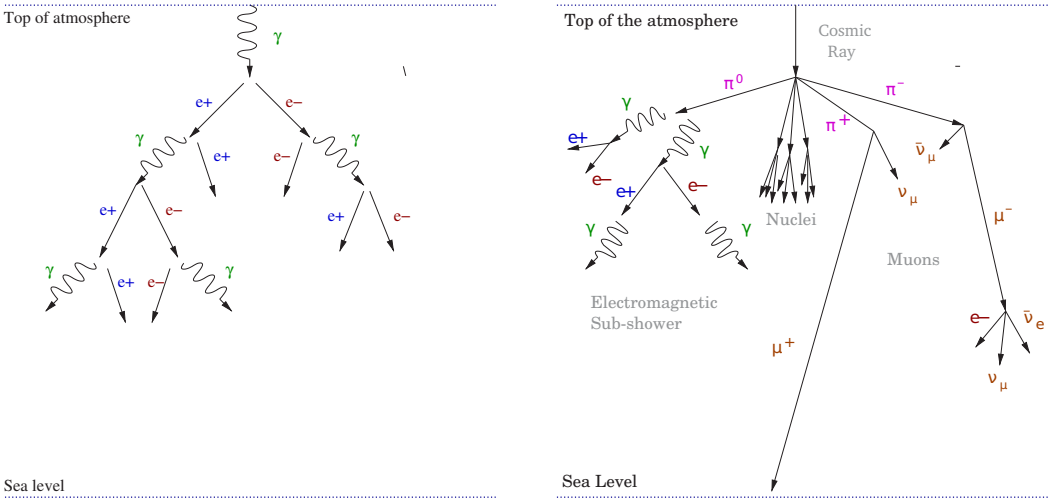

Figure 4–2: A schematic diagram of a gamma ray shower (left) and a hadronic shower (right) [91].

E_c, where energy losses from absorption processes such as ionization and excitation begin to dominate, the maximum number of particles in the shower is reached, called shower maximum. The number of particles in the shower decreases after this, as the particles are absorbed by the atmosphere. A similar process occurs for primary electrons and positrons. Due to the nature of electromagnetic interactions, electromagnetic showers are highly collimated. The first image in Figure 4–1 (right) shows a simulation of a shower initiated by a 100 GeV photon. Figure 4–2 (left) shows a schematic diagram of an electromagnetic shower.

Hadronic showers are initiated by hadronic particles such as protons and nuclei and involve hadronic interactions as well as electromagnetic interactions. Hadronic particles interact with atmospheric nuclei producing charged and neutral pions. The neutral pions decay into photons, initiating further electromagnetic sub-showers:

$$\pi^0 \rightarrow \gamma + \gamma.$$

The charged pions decay into muons and neutrinos:

$$\pi^+ \rightarrow \mu^+ + \nu_\mu$$

$$\pi^- \rightarrow \mu^- + \bar{\nu_\mu}.$$

And the muons decay into electrons and neutrinos:

$$\mu^+ \rightarrow e^+ + \bar{\nu_\mu} + \nu_e$$

$$\mu^- \rightarrow e^- + \nu_\mu + \bar{\nu_e}.$$

The second image in Figure 4–1 (right) shows a simulation of a shower initiated by a 100 GeV proton. A schematic diagram of a hadronic shower is shown in Figure 4–2 (right). High transverse momentum particles are produced in hadronic showers, resulting in showers that are less collimated than electromagnetic showers, as can be seen in Figure 4–1 (right). These differences allow the electromagnetic showers to be distinguished from hadronic showers, using a technique described in section 5.10.

4.3 Cherenkov radiation

When light propagates through a medium such as air or water, the velocity with which the light propagates is given by $v_l = c/n$ where c is the speed of light in a vacuum and n is the index of refraction of the medium. When charged particles traverse such a medium with a velocity $v_p > v_l$, electromagnetic radiation called Cherenkov radiation is emitted. This radiation was named after Pavel Cherenkov, who experimentally investigated the phenomenon in detail in 1934. The emission of Cherenkov radiation is analogous to the creation of a sonic boom created when an object travels faster than the speed of sound in air. As the charged particles travel through the medium, the atoms surrounding the charged particle become polarized in the direction of the charged particle. As the particle moves away, the atoms become

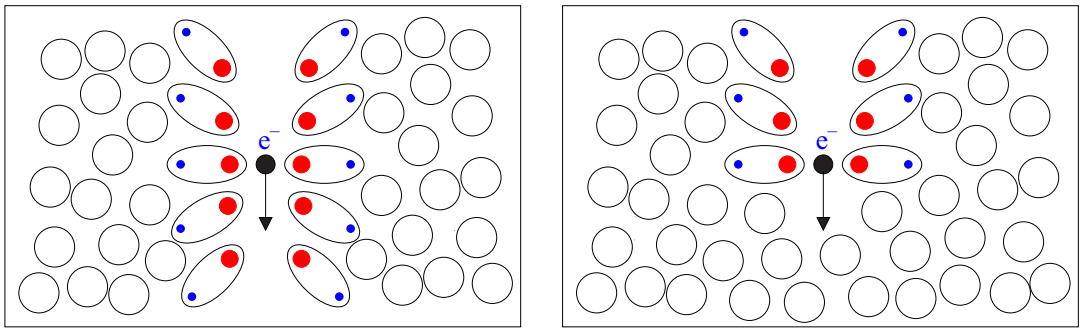

Figure 4–3: The polarization of a medium due to the passage of a charged particle. Left: when the charged particles travel at $v_p < c/n$, the polarization pattern is symmetric around the charged particle, and there is no net emission. Right: when the charged particles travel at $v_p > c/n$, the polarization pattern is asymmetric about the charged particle and Cherenkov emission occurs. Figure from [91].

de-polarized. The time variation of the polarization state of the atoms causes the atoms to radiate.

If $v_p < v_l$ the polarization pattern is symmetric around the charged particle, as shown in Figure 4–3 (left). This symmetry leads to a zero net induced dipole around the charged particle, and so no net emission occurs. If $v_p > v_l$ the polarization pattern is asymmetric around the charged particle, as shown in Figure 4–3 (right). This asymmetry leads to a non-zero net induced dipole, leading to a net emission of photons.

The angle of the emitted photons with respect to the propagation vector of the charged particle (called the Cherenkov angle) may be determined using a geometric argument (see figure 4–4). The emitted light travels a distance $t \times v_l = t \times c/n$, and the charged particle travels a distance of $t \times v_p = t \times \beta \times c$. Therefore:

$$\cos(\theta) = \frac{t \times c/n}{t \times \beta \times c} = \frac{1}{\beta n}.$$

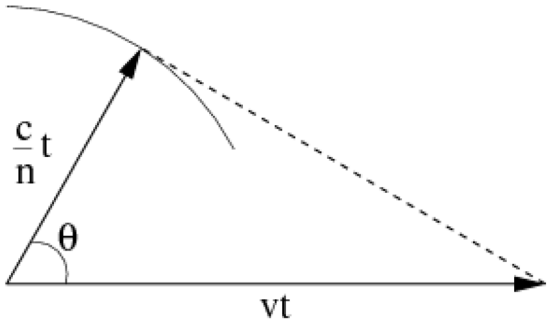

Figure 4–4: Cherenkov cone geometry: the charged particles travel a distance $t \times v_p = t \times \beta \times c$ and the Cherenkov light travels a distance $t \times v_l = t \times c/n$. See text for details.

The maximum Cherenkov angle of the particle is obtained as the velocity of the particle approaches c, and depends only on the index of refraction of the medium: $\theta_{max} = \arccos(1/n)$. The minimum velocity required for Cherenkov emission, $v_p = c/n$ can be substituted into the expression for relativistic energy in order to obtain an expression for the minimum energy required for Cherenkov emission as a function of the rest mass of the particle and the index of refraction of the medium:

$$E_{min} = \frac{m_0 c^2}{\sqrt{1 - 1/n^2}}.$$

The density, and therefore the index of refraction of the atmosphere varies as a function of altitude, and therefore the maximum Cherenkov angle and minimum energy vary with altitude as well. For electrons and muons at sea level, the minimum energy is 21 MeV and 4.4 GeV respectively. For particles travelling through air at sea level, the maximum Cherenkov angle in air is approximately 1.4 degrees.

The number of Cherenkov photons emitted per unit path length and wavelength is given by:

$$\frac{d^2N}{dxd\lambda} = \frac{2\pi\alpha Z^2}{\lambda^2}\Big(1 - \frac{1}{\beta^2(n(\lambda))^2}\Big) \tag{4.1}$$

where α is the fine structure constant, Ze is the charge of the particle, β is the velocity of the charged particle divided by the speed of light, v_p/c and λ is the wavelength of the Cherenkov radiation [58]. As can be seen from equation 4.1, the intensity of the emission is inversely proportional to the square of the wavelength. For air, the wavelength dependence of the index of refraction limits the Cherenkov emission to UV wavelengths or longer, resulting in a peak in the Cherenkov spectrum at UV wavelengths. More information regarding Cherenkov radiation can be found in [68]. The high-energy charged particles in the air showers described in the previous section cause the atmosphere to emit Cherenkov radiation. The Cherenkov radiation from the showers propagates to the ground, with the radiation emitted highest in the atmosphere arriving later than the radiation emitted near the ground, all within a duration of several nanoseconds. This radiation may be collected, and used to produce images of the showers, a technique called the imaging atmospheric Cherenkov technique, described in the next section.

4.4 The imaging atmospheric Cherenkov technique

For a given astronomical gamma-ray source, the flux of gamma-rays drops rapidly as a function of energy. Consequently, above approximately 100 GeV, the

space-based telescopes described in section 1.2 are not large enough to detect a sufficient number of particles for reasonable exposure times in order to perform useful analyses. In this regime, detectors with large effective areas are required. The Cherenkov light pools from the air showers described in sections 4.2 and 4.3 cover an area of approximately 10^5 m^2. The imaging atmospheric Cherenkov technique achieves comparable effective areas by collecting this light with telescopes on the ground. The Cherenkov light is focused by large segmented reflectors onto cameras consisting of photomultiplier tubes (described below) or solid state light detectors that enable images of the showers to be made. The shower images are digitized, assigned timestamps using GPS clocks and stored. The analysis of the shower images enables the selection and determination of the arrival directions and energies of gamma-ray candidate events. Sources of astrophysical gamma rays are discovered by detecting a statistically significant excess of gamma-ray candidate events originating from particular directions in the sky. Fluxes and upper limits are calculated using the measured excesses, observation times and instrument response functions produced from simulations. Light curve and pulsar analyses may be performed using the GPS timestamps. The details of these analysis techniques are described in the next chapter. Figure 4–5 shows a schematic diagram illustrating the imaging atmospheric Cherenkov technique.

The first imaging atmospheric Cherenkov telescope (IACT), the Whipple 10 m telescope, was constructed in 1967 at what is now the Fred Lawrence Whipple Observatory in southern Arizona. Using this telescope, the Whipple collaboration, led by Trevor C. Weekes, first detected the Crab nebula in VHE gamma rays using

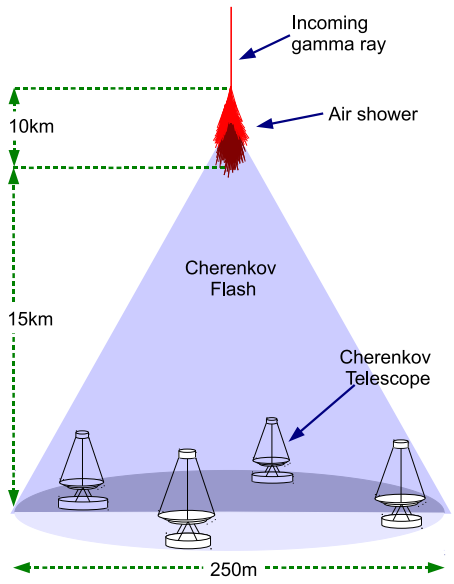

Figure 4–5: A schematic diagram illustrating the imaging atmospheric Cherenkov technique. Figure from [91].

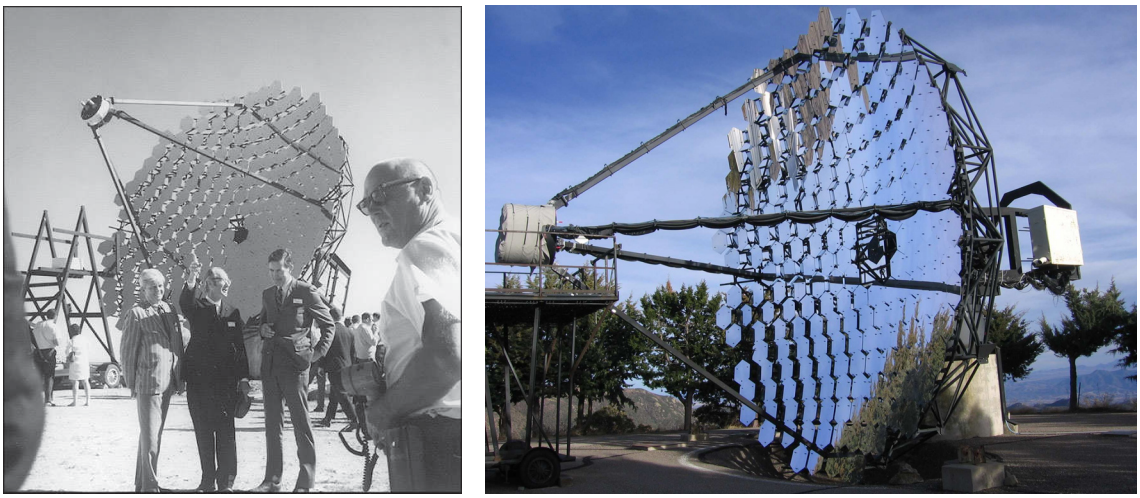

Figure 4–6: Left: A photograph of the Whipple 10 m telescope, the first IACT, on the opening day of Mount Hopkins observatory in 1968. The observatory was later renamed the Fred Lawrence Whipple observatory after the director of the observatory (center) [80]. Right: The Whipple 10 m telescope in the spring of 2011, a year before being decommissioned.

the imaging technique in 1989 [57]. Figure 4–6 (left) shows a photograph of the Whipple 10 m telescope on the opening day of the observatory in 1968. Figure 4–6 shows the Whipple 10 m telescope in the spring of 2011, approximately a year before being decommissioned in the summer of 2012. The VERITAS telescopes, described in the next section, are located at the base camp of the Fred Lawrence Whipple observatory, and resemble the original Whipple 10 m telescope. Current IACTs include VERITAS in southern Arizona, H.E.S.S. in Namibia, and MAGIC in La Palma. The next generation IACT, Cherenkov Telescope Array (CTA), is currently being built, and will consist of large arrays of telescopes of different sizes at a northern and southern site. CTA north will be built at the MAGIC site in La Palma, and CTA south will be built in Argentina. CTA south will consist of approximately 100 telescopes, while CTA north will consist of approximately 20 telescopes [90].

4.5 The VERITAS array

VERITAS is an array of four imaging atmospheric Cherenkov telescopes located approximately 1268 m above sea level at the Fred Lawrence Whipple observatory in southern Arizona. The telescopes consist of 12 meter diameter segmented optical reflectors connected to an optical support structure (OSS) attached to an alt-az positioner. A camera consisting of 499 photomultiplier tubes (PMTs) is connected to the OSS by quad arms. Counterweights in the back of the reflectors ensure that the telescopes remain balanced. Trailers located beside the telescopes house data acquisition, tracking, telescope trigger and other important systems. Platforms located beside the telescopes allow access to the cameras. The array is controlled from a central building that houses the control room, array trigger and data acquisition

Figure 4–7: A photograph of the VERITAS array [22].

systems. A photograph of the VERITAS array is shown in Figure 4–7. The first VERITAS telescope went online in the winter of 2005 and the second and third telescopes were completed in the spring and fall of 2006 respectively. VERITAS began operations as a four telescope array in the spring of 2007, and is still operating at the time of the writing of this thesis in the summer of 2018. The telescopes are named T1 to T4 following the order in which they were completed. In the summer of 2009, T1 was moved to a new location in order to increase the collecting area of the array, and to reduce the number of triggers caused by single muon events (see section 5.3.3). The epoch prior to the T1 move is designated V4, and the epoch following the move is designated V5. The PMTs in the cameras were replaced in the summer of 2012 in order to improve the sensitivity of the array to lower energy showers. The epoch following the PMT upgrade is designated V6. VERITAS is sensitive to very-high-energy gamma rays in the energy range between 85 GeV and 30 TeV, and is able to detect a source with a flux of 1 percent of the Crab Nebula in 25 hours of observations. VERITAS has an angular resolution of approximately 0.1 degrees above 1 TeV and an energy resolution of 17 percent at 1 TeV. The details of the various components of the VERITAS array are discussed in the following subsections.

4.5.1 The VERITAS Positioners

The VERITAS positioners consist of commercial altitude-azimuth type positioners, manufactured by RPM-PSI in Northridge, CA. The positioners have servo motors for moving the telescopes in azimuth and elevation that can slew the telescopes at approximately one degree per second. The positioners are controlled with custom

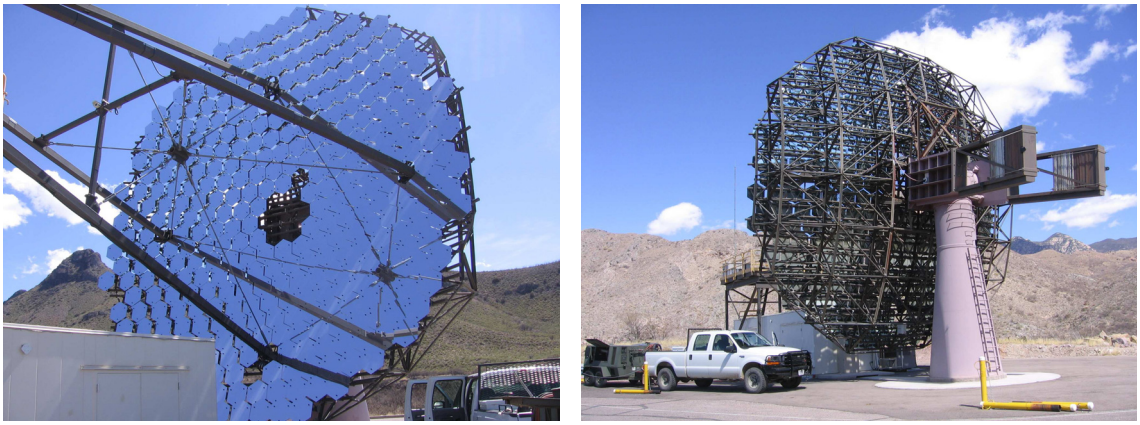

Figure 4–8: Left: a photograph of the front of the T1 reflector, showing the mirrors and quad arms. Right: a photograph of the back of T1, showing the OSS, positioner and counterweights.

software that enables the telescopes to slew to and track astronomical sources of interest. The telescopes may be moved together as an array or independently. The pointing directions of the positioners are continually monitored by encoders, and these measurements are related to positions in the sky using a software model. CCD cameras mounted to the quad arms continually capture images of the field of view during normal observations in order to measure the pointing directions of the telescopes. Offline analyses of these images is performed in order to reduce the pointing uncertainty of the array.

4.5.2 Mirrors and OSS

The VERITAS telescopes are examples of a Davies-Cotton design [24], which consists of a spherical reflector with radius of curvature r comprised of many small mirror facets with radius of curvature $2r$, and a camera supported by quad arms at the focal plane of the reflector. This design allows reflectors with large collecting

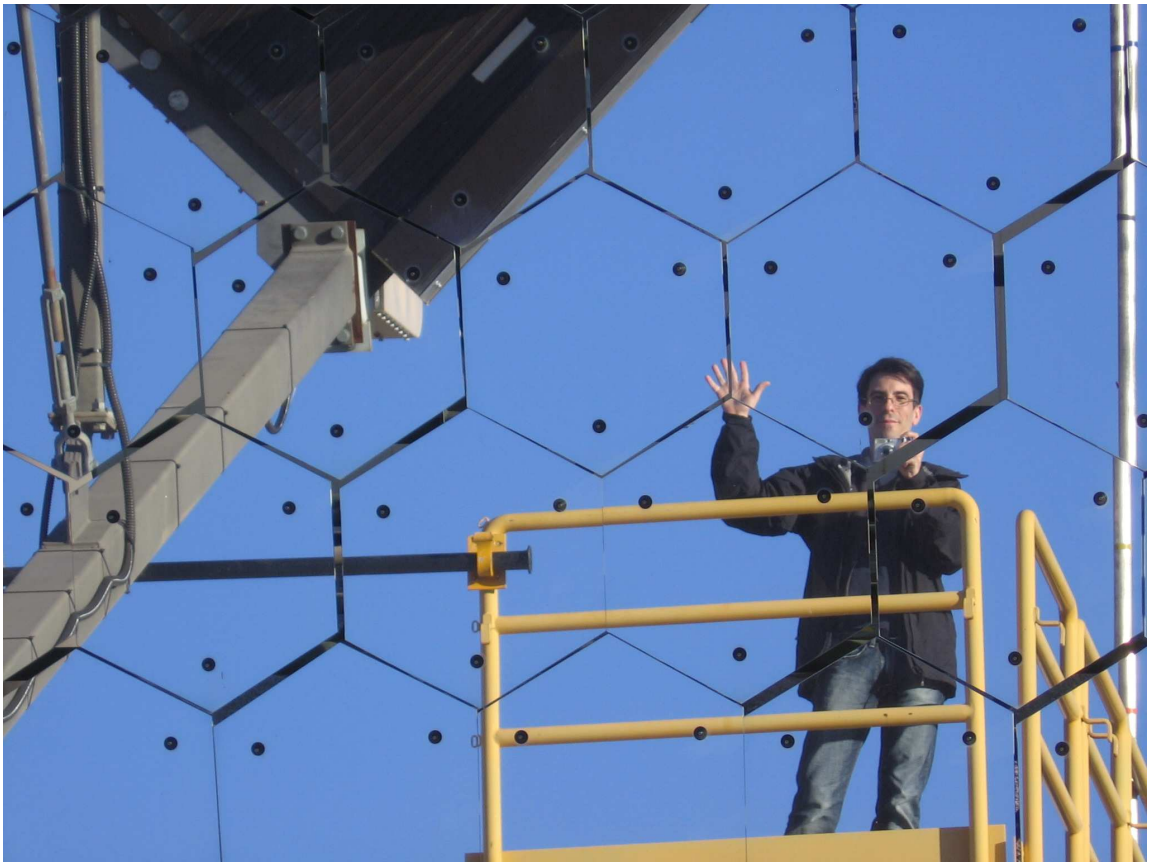

Figure 4–9: A photograph of the author reflected in the VERITAS mirrors.

areas to be made relatively inexpensively. The VERITAS reflectors consist of 345 hexagonal mirror facets attached to a steel optical support structure (OSS), which is attached to the positioner. Quad arms connect the OSS to the camera, and the uppermost quad arm connects to counterweights located in the back of the OSS. Far-infrared cameras are mounted on T2 and T3 in order to monitor the weather as part of the VERITAS data quality monitoring procedures, described in section 5.2. A photograph of the front of the T1 reflector showing the mirrors and quad arms is shown in Figure 4–8 (left). A photograph of the back of T1, showing the positioner, OSS and counterweights is presented in Figure 4–8 (right). Triangular mounts attached to the OSS support the mirrors with three threaded steel rods. Adjustment nuts allow the individual mirror facets to be aligned. The spherical mirror facets are made of glass, coated with anodized aluminium, with a 24 meter radius of curvature and an area of 0.322 square meters. The reflectivity of the mirrors is approximately 90 percent when they are first coated. Due to the harsh conditions of the Arizona desert, the reflectivity of the mirrors drops over time. The reflectivity of the reflectors is therefore monitored regularly as described in section 5.3.2, and measurements of the reflectivity of individual facets is also performed on a regular basis. The mirrors are coated on site, and old mirror facets are replaced on a regular basis with re-coated mirrors. The mirrors are also regularly washed in order to remove accumulated dust. In order to determine the optical point spread function (PSF) of the telescopes, reflective screens are placed over the PMTs at the focal plane, and the telescopes are pointed to various bright stars in the sky. The images of the stars in the focal plane are recorded with CCD cameras, and used to determine if mirror

alignment is required. In order to align the mirrors to achieve a better optical PSF, the required adjustments to the nuts on each mirror facet are determined by pointing the telescopes in a raster scan pattern around the positions of bright stars. CCD cameras placed at the focal plane of the telescopes take pictures of the mirrors for each pointing position. The pointing direction where the star is visible in a given facet is used to determine the required adjustments for that facet. A photograph of the author reflected in the VERITAS mirrors is shown in figure 4–9.

4.5.3 The VERITAS cameras

The VERITAS cameras are located 12 meters away from the reflectors at the focal plane and are connected to the OSS via the quad arms. The uppermost quad arms transfer the load of the camera to the counterweights behind the OSS using a mechanical bypass. The cameras are contained in a 1.8 m x 1.8 m square box, and consist of 499 hexagonally packed photomultiplier tubes and light cones (described below) arranged in a plane facing the reflector, perpendicular to the pointing direction of the telescope. The cameras are protected by rolling shutters, which protect the cameras from sunlight, water and dust when closed. Platforms located beside the telescopes allow access to the cameras in order to perform calibration and maintenance work. A detachable plate is placed over the PMTs during normal operations with reflective segmented parabolic light concentrators for each PMT called light cones. The light cones have a hexagonal aperture, allowing them to be close packed, maximizing the light collection area for each PMT. The light cones also restrict the arrival directions of photons to be primarily from the direction of the reflectors, reducing background light. The light cones are washed on a regular basis in order to

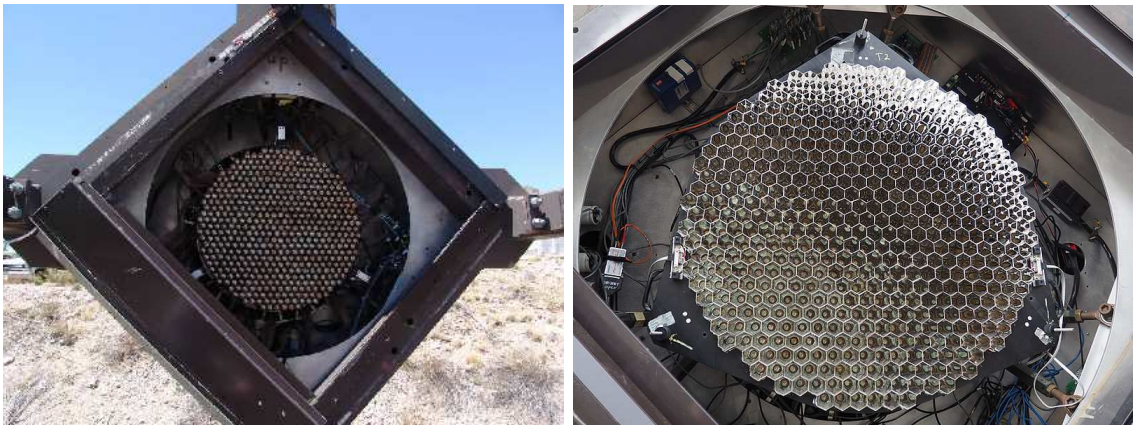

Figure 4–10: The VERITAS camera box (left) [82] and a closeup of the PMTs with light cones attached (right) [22].

improve their reflectivity by removing accumulated dust. The distance between the centers of adjacent PMTs in the cameras is 31.4mm, corresponding to an angle scale of 0.15 degrees on the sky. The total field of view of the VERITAS cameras is 3.5 degrees. Figure 4–10 shows a photograph of a VERITAS camera, showing the PMTs without light cones (left), and a closeup of the camera with the light cones attached (right).

The PMTs consist of glass vacuum tubes with a semi-transparent coating on the front called the photo-cathode, and several electrodes kept at different voltages, called the dynode chain (see Figure 4–11). Light incident on the photo-cathode will eject an electron via the photoelectric effect with a probability given by the quantum efficiency of the photo-cathode, which is a function of photon wavelength. The ejected electron (called a photoelectron) is accelerated towards the first dynode due to the applied voltage. When the photoelectron interacts with the first dynode, the kinetic energy of the electron causes additional electrons to be emitted from

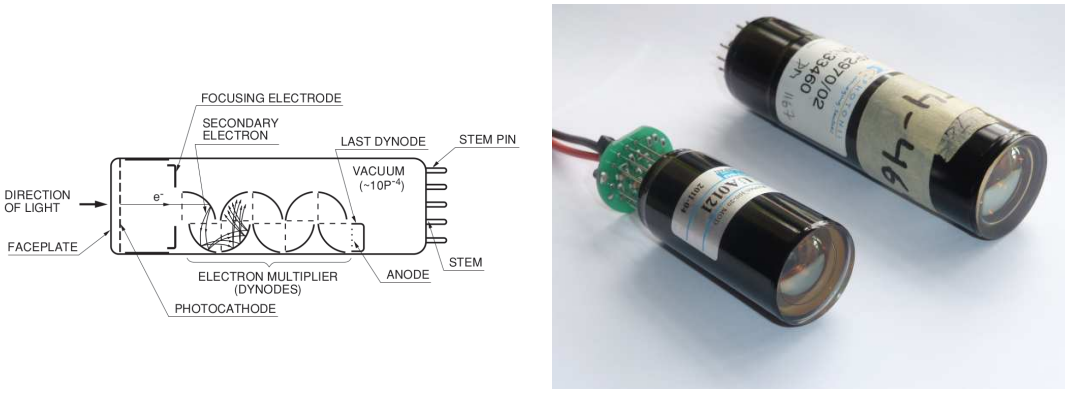

Figure 4–11: A schematic diagram of a PMT (left) [69] and a photograph of a Photonis XP2970/02 PMT (back) used in the V4 and V5 epochs and a Hamamatsu R10560-100-20 MOD PMT (front) used in the V6 epoch (right) [3].

the dynode, a process called secondary emission. These electrons are accelerated to the next dynode due to the applied voltage, and the process of secondary emission continues along the dynode chain, multiplying the original photoelectron by a factor of approximately 10^5 by the time the electrons reach the anode of the PMT. From Winter 2005 to the Spring of 2012 (the V4 and V5 epochs), VERITAS used Photonis XP2970/02 PMTs in the cameras. From the Fall of 2012 to the present (the V6 epoch), VERITAS used higher quantum efficiency Hamamatsu R10560-100-20 MOD PMTs in the cameras. The PMT upgrade resulted in an improved overall sensitivity of the array, and an improved sensitivity to lower energy showers [3]. Figure 4–11 (right) shows a photograph of a Photonis XP2970/02 PMT (back) and a Hamamatsu R10560-100-20 MOD PMT (front).

During nights with bright moonlight, filters are placed between the PMTs and the light cones in order to filter out moonlight while allowing most of the Cherenkov light from the showers to pass through. Figure 4–12 shows the quantum efficiency

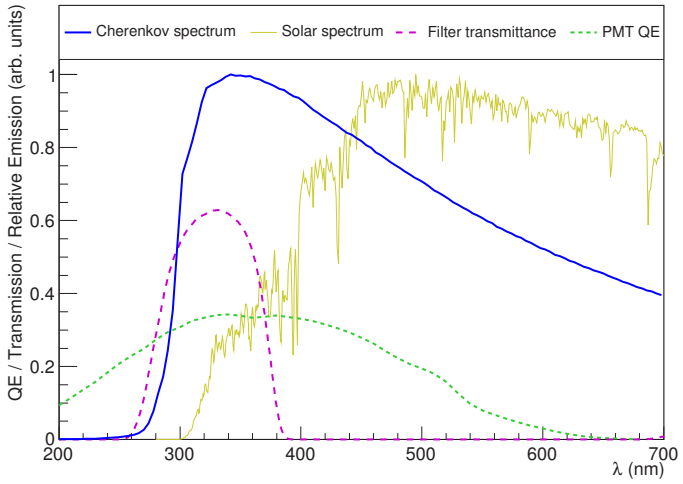

Figure 4–12: The measured quantum efficiency of the Hamamatsu R10560 PMTs (green), the Cherenkov spectrum observed from an electromagnetic shower produced from a 500 GeV gamma ray (blue), solar (moonlight) spectrum (yellow) and moonlight filter transmittance as a function of wavelength (purple) [40].

of the Hamamatsu R10560-100-20 MOD PMT(green), the Cherenkov spectrum observed from a shower initiated by a 500 GeV gamma ray (blue), the solar (moonlight) spectrum (yellow) and the transmittance of the moonlight filters as a function of wavelength (purple). As can be seen from the figure, the filters allow a sizable fraction of the Cherenkov light from showers to be transmitted while attenuating most of the moonlight. The use of the filters has allowed VERITAS to operate with an increased duty cycle by allowing observations at times when the PMT currents would be too high for normal observations [40]. Due to the attenuation of Cherenkov light by the filters, filter data has a higher energy threshold and must be analyzed differently than normal data.

The voltages for each PMT are provided by CAEN model SY1527 modular power supplies, which allow voltages to be set for each PMT individually using custom-made

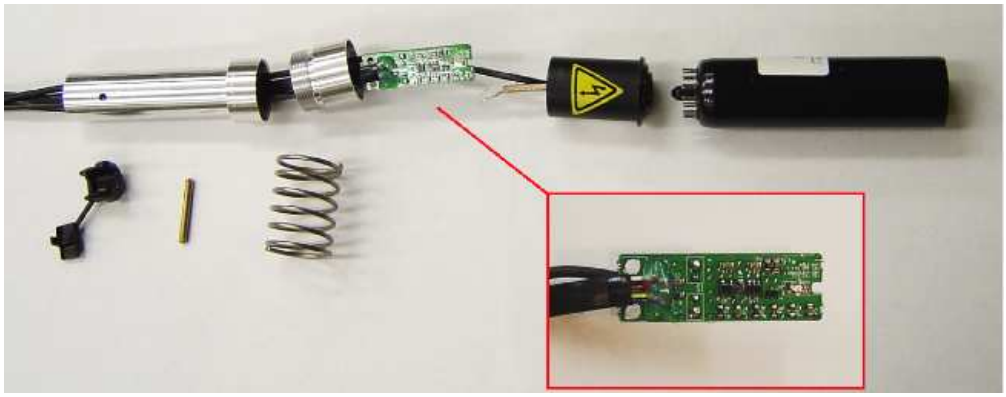

Figure 4–13: A photograph of a disassembled VERITAS pixel, showing the main components: aluminum housing, circuit board with pre-amplifier, current monitor and charge injection circuits, voltage divider and PMT [122].

software. The voltages for each dynode in the PMTs are obtained using a voltage divider circuit, the maximum voltage being determined by the set power supply voltage. The power supply voltages are set so that the gains of the PMTs are set to approximately 2×10^5, a process known as flat fielding. The anode currents from the PMTs are amplified by a factor of 6.6 by pre-amplifier circuits located at the base of the PMTs in a protective metal casing. The amplification of the signal prior to being sent to the data acquisition system improves the measured signal to noise ratio. The amplified PMT signals travel down coaxial cables threaded through the quad arms and positioners into the data acquisition system located in the trailers, described in section 4.5.5. The anode currents of each PMT are monitored in real time with a resolution of 0.5 μA using current monitor circuits located on the same board as the pre-amplifiers. The current monitors allow the observers to ensure that the PMTS are being operated with currents below approximately 20 μA in order to avoid premature ageing of the PMTs. The PMTs are typically operated with

currents of approximately 7 μA during normal operations. The current monitors also perform auto suppression of the PMT voltages when the anode currents exceed safety limits. Charge injection circuits located on the same board as the preamp and current monitor circuits allow pulses to be injected into the coaxial cables for diagnostic purposes. Figure 4–13 shows a disassembled VERITAS pixel.

4.5.4 The VERITAS trigger system

The amplified PMT anode signals are transferred from the pre-amplifiers at the base of the pixels via the coaxial cables to the data acquisition systems located in the trailers. Specifically, the coaxial cables are fed to flash analog to digital converters (FADCs), described in section 4.5.5. The signals from the PMTs are continually digitized by the FADCs with an 8-bit precision at a rate of 500 MHz. This corresponds to a data rate of approximately of 2 GB/s for all four telescopes. Without some form of data selection mechanism, this rate would lead to file sizes of approximately 3.6 TB for a 30 minute run. In order to reduce the data rate, VERITAS uses a trigger system in order to preferentially record the digitized signals from the PMTs when the Cherenkov flashes from air showers are incident on the array, rejecting the background of night-sky photons, moonlight, terrestrial light and Cherenkov light from local muons (described in section 5.3.3). In order to achieve this, the digitized samples of the amplified PMT signals are continually placed in circular 64 μs buffers, parts of which are read out when a trigger signal is received. The data from the buffers and additional information is collected by computers in each trailer called event builders, and sent to a computer called the harvester (see section 4.5.7), where it is assembled into a file. The use of this trigger system results

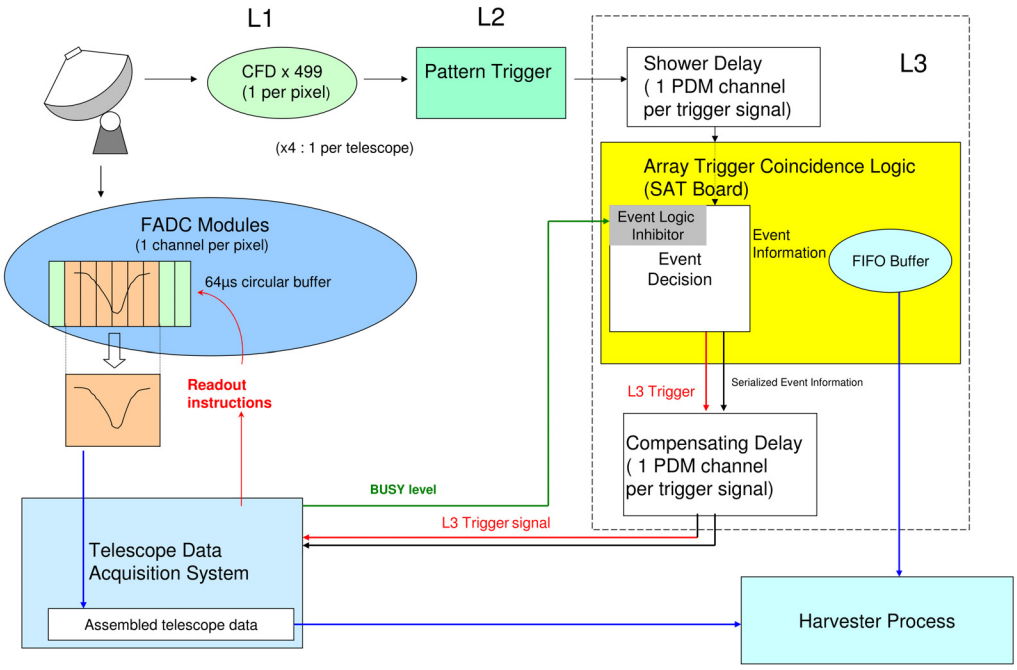

Figure 4–14: A schematic diagram of the VERITAS trigger and data acquisition systems [123]. See text for details.

in typical file sizes of approximately 10 GB for a typical 30 minute run. The details of the VERITAS data acquisition system are described in section 4.5.5.

The VERITAS trigger system consists of three levels. The level 1 trigger (L1) consists of a pixel-wise trigger system that fires when the amplified PMT anode signal exceeds a given threshold. The level 2 trigger system (L2) is a telescope-wise trigger system that fires when the L1 triggers fire for three contiguous pixels on a given telescope within a specified time interval. The level three trigger system (L3) fires when the L2 triggers of at least two telescopes fire within a specified time interval.

The details of the three levels of the VERITAS trigger system are described in subsections 4.5.4.1, 4.5.4.2 and 4.5.4.3. A schematic diagram showing the VERITAS trigger and data acquisition systems is shown in Figure 4–14.

4.5.4.1 The level 1 trigger system

The level one (L1) trigger system consists of discriminator circuits for each VERITAS PMT, which fire when the signal from the PMT meets certain intensity and timing criteria. The signals from the PMTs are fed into the analog front end of the FADC modules, and split, with one copy being sent to the L1 circuits located on the FADC modules, and the other copy being sent to the FADC circuits in order to digitize the signal. The L1 discriminator circuits consist of constant fraction discriminators (CFDs), which have the advantageous property that the time required for the discriminator to fire is not strongly dependent on the intensity of the signal. In order to achieve this, CFDs make use of a threshold discriminator (TD), and a zero crossing discriminator (ZCD). The VERITAS CFDs also employ a rate feedback (RFB) mechanism in order to limit the trigger rate for high intensity signals. The threshold discriminator fires when the signal from the PMT exceeds a programmable threshold. Normal VERITAS observations use a threshold of 45 mV. Moonlight observations without the moonlight filter use raised thresholds of 60 mV in order to reduce the rate of triggers due to moonlight. When the moonlight filters are in use, a reduced threshold of 25 mV is used due to the light attenuation associated with the use of the filters. For simple threshold discriminators, the time required for the discriminator to fire depends strongly on the intensity of the signal. A zero crossing discriminator is an example of a discriminator with a firing time not strongly

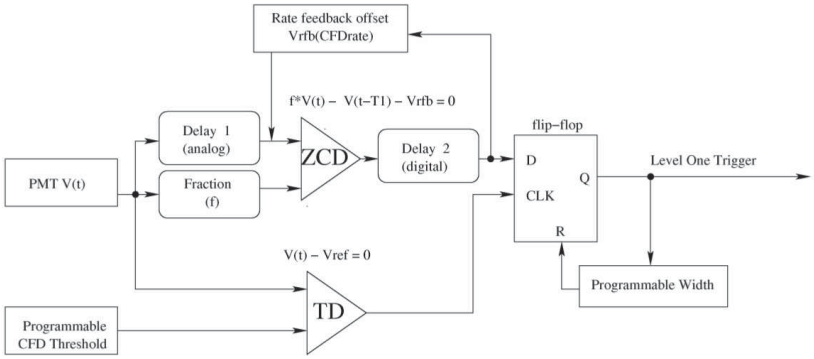

Figure 4–15: A schematic diagram of a VERITAS CFD [46]. See text for details.

dependent on pulse height. The zero crossing discriminator splits the signal, scaling one copy by a fraction f, and inverting and delaying the other copy by time $T1$ using an analog delay. These signals are combined, and the ZCD fires when the resulting signal crosses zero volts. When the ZCD condition is satisfied while the TD is over the threshold, the L1 condition for the channel is satisfied and a 10 ns ECL pulse is sent to the L2 trigger system (described below). The use of CFDs instead of a simple TD reduces the coincidence time required for the L2 trigger, which has the effect of lowering the energy threshold of the array. The CFD configuration also has the effect of being insensitive to night sky background photons, as such signals are much faster than the signals from air showers, and the TD falls below threshold before the ZCD can fire. In order to limit the L1 trigger rates when the PMT anode currents are high, the VERITAS CFDs use a rate feedback circuit that applies a DC offset voltage to the delayed and inverted signal of the ZCD proportional to the measured trigger rate. This has the effect of reducing the trigger efficiency of the CFDs as the trigger rate increases. The VERITAS CFDs use an offset voltage of 52

mV/MHz. During normal operations, typical VERITAS CFD trigger rates are of the order of several MHz. Figure 4–15 shows a schematic diagram of a CFD circuit.

4.5.4.2 The level 2 trigger system

The L2 system consists of a pattern trigger that fires when the L1 condition for three contiguous pixels is met within a specified time coincidence window. When the L2 trigger criteria is met, a pulse is sent to the L3 trigger system, described in section 4.5.4.3. The main purpose of the L2 trigger system is to increase the likelihood that triggers are due to the Cherenkov flashes from air showers as opposed to random night sky background fluctuations. The trigger pulses from the CFDs for a given telescope are sent from the FADC modules to the level 2 (L2) trigger system via ribbon cables. Delays are applied to each channel in order to correct for the different delays caused by varying PMT cable lengths, L1 cable lengths and the details of the internal electronics of the L2 system. Prior to the summer of 2010, VERITAS used a CAMAC based trigger system with a co-incidence window of 8 ns. The trigger system was upgraded in the summer of 2010 [64], and uses custom-made VME modules based on FPGA technology in order to process the trigger logic. The current L2 trigger system is now operated with a coincidence window of 5ns, which has resulted in improved background rejection, and a lower energy threshold. Typical L2 rates for normal operations are on the order of several kHz.

4.5.4.3 The level 3 trigger system

The L3 trigger system ensures that the array triggers on showers seen by multiple telescopes. This reduces triggers caused by NSB, and greatly reduces triggers caused by local muons, which are mostly seen by only one telescope at a time. The

level three (L3) trigger criteria is met when two or more telescopes issue an L2 signal within a coincidence window of 50 ns. When the L3 trigger criteria is met, the L3 system sends event information to the data acquisition computers in the trailers and a signal to the FADC modules to read out a portion of the buffers. The VERITAS L3 system has various components, including digital asynchronous transceiver modules (DATs), programmable delay modules (PDMs), time to digital converters (TDCs), and a sub-array trigger board (SAT). The DATs consist of VME based optical-electrical converters that transmit the signals from the L2 trigger systems to the L3 system and transmit the L3 trigger pulses to the data acquisition systems in the trailers via fiber optic cables. The DATs also transmit event information such as event number to the data acquisition computers located in the trailers. The PDMs consist of VME modules that delay the L2 and L3 signals in order to compensate for the different travel times of the pulses. Additional telescope pointing-dependent delays are applied to the L2 pulses to compensate for the different Cherenkov photon travel times from the showers to the telescopes. The use of the PDMs allows the use of a narrow L3 coincidence window, optimizing background rejection and energy threshold. The trigger coincidence logic is evaluated on the SAT board, a custom-made VME module based on FPGA technology located in the control building. The delayed L2 pulses are fed into TDCs located on the SAT module, which determines the arrival times of the pulses. These times are fed to the FPGA module, which implements the trigger logic. If two of the delayed L2 pulses are found to occur within 50ns, an L3 trigger signal and event information is sent via the PDMs and DATs to the data acquisition systems located in the trailers. During normal observations,

VERITAS operates with a typical L3 trigger rate of approximately 400 Hz. These triggers are primarily due to the Cherenkov light from air showers, while most of the background of night-sky photons, moonlight, terrestrial light and Cherenkov light from local muons is rejected by the trigger system.

4.5.5 The VERITAS data acquisition system

VERITAS data is taken in 30 minute observing runs while the array tracks a particular location in the sky. Each observing run is assigned a unique run number, which is incremented by one for each new run. As mentioned in the previous section, when an L3 trigger occurs, a signal is sent to the data acquisition system to read out a part of the FADC buffers. This, and other information is assembled into an 'event' - a digital record of the shower observation by the array. Each event for a given observing run is assigned a unique event number, and assembled into a file, identified by the run number, containing all of the events recorded during the run. All of this is accomplished by the VERITAS data acquisition system, which consists of the FADC modules and associated support hardware, four computers called Event Builders that assemble the FADC information from each telescope into 'telescope events', and a computer located in the control building called the Harvester, that assembles the telescope events into array events, and assembles them into the data files.

4.5.6 The VERITAS FADCs

The VERITAS flash analog-to-digital converter (FADC) modules consist of an analog front end, the CFDs, described in section 4.5.4 and the FADCs themselves, which continually digitize the signals from the PMTs with an 8-bit precision at a

rate of 500 MHz. The 2 ns samples of the amplified PMT signals are put into 64 μs circular buffers, parts of which are read out when an L3 signal is received. When the readout signal is received by the FADC modules, the buffering process stops, and a busy signal is sent to the L3 trigger while the readout process takes place. During this time, the array is unable to record shower events. The fraction of the total observing time where this is the case is called the dead time, and is approximately 15 percent when VERITAS is operating with a typical L3 rate of 400 Hz. The portion of the buffers read out as a result of the trigger (the readout window) is set so that the samples corresponding to the Cherenkov pulses from the the shower that initiated the L3 trigger, called 'traces', are recorded. During the V4 and V5 epochs, a 20 sample readout window was used. For the V6 era, a 16 sample readout window was used.

The analog front end of the FADC modules includes a 1 kΩ resistor that allows measurements of the currents via the induced IR voltage drop, a high pass filter, and high gain and low gain amplifiers. In order to extend the dynamic range of the digitizers, the signal from the PMTs is split in three, with one copy being sent to a high gain amplifier, one copy being sent to a delay module followed by a low gain amplifier, and the third copy being sent to a discriminator. If the high gain signal exceeds the dynamic range of the digitizer, the discriminator fires, causing the delayed signal from the low gain amplifier to be digitized. This mechanism, called the high/low gain switch, also sends a flag to the event builder so that the readout window corresponds to the location of the low gain pulse, and keeps a record of the switch having fired, which is used by the analysis software. The use of the high/low

gain switch increases the dynamic range of the system by a factor of approximately 6.

The inputs to the FADC modules are biased with a constant voltage so that both positive and negative fluctuations are recorded. This voltage, in addition to the signal produced from ambient background light constitutes the 'pedestal', the signal recorded by a given PMT in the absence of Cherenkov light. In order to measure the pedestal during normal operations, forced L3 triggers occur at a rate of 3 Hz. The resulting events are called pedestal events, and are used by the data analysis software to characterize the background signal. The 50 10-channel FADC modules for each telescope are hosted in four VME crates located in each telescope trailer. The FADC crates also each host a crate computer that controls the modules. The FADC modules generate a large amount of heat during data taking, and are therefore cooled using a water-based cooling system.

4.5.7 The event builders and harvester

The event builders consist of dedicated computers in each telescope trailer that collect the traces from the FADC modules, trigger information, the high/low gain flags, information from the L3 system such as the event number and the times recorded by the GPS clocks in each trailer. This information is assembled into telescope events, and sent to the harvester in the control building via standard network cables. The harvester consists of a dedicated computer that collects the telescope events and additional information from the L3 system into array events, and assembles them into a file format called compressed VERITAS bank format (.cvbf). The harvester also runs an online analysis process called quicklook, that performs a crude

analysis of the incoming data in order to monitor the recorded signals in real time. Once the .cvbf files are assembled, they are named according to their run number and transferred to a repository located at UCLA, where they are made available for download. The next chapter describes the VERITAS data analysis procedures that are performed on these files.

CHAPTER 5
VERITAS data analysis techniques

5.1 Introduction

In order to produce science results from the information stored in the VBF files, the data must be analyzed. This is accomplished by the use of custom-made VERITAS data analysis packages, VEGAS (VEritas Gamma ray Analysis Suite) and Event Display. These packages are written in C++ and make use of the ROOT framework, a set of analysis tools for particle physics [14]. The use of two separate analysis packages allows independent analyses of the data in order to verify the science results. This chapter describes the VERITAS data analysis procedures as implemented by Event Display, although the analysis methodology for VEGAS is quite similar.

The data stored in the VBF files consists of events, containing the data read out as a result of an L3 trigger. VERITAS runs are typically 30 minutes in duration, and a typical trigger rate of 400 Hz leads to VBF files consisting of approximately 7×10^5 events. Each event consists of digitized 'traces' of the currents from each PMT, consisting of a set of 8-bit samples (20 samples for the V4 and V5 epochs and 16 samples for the V6 epoch) taken in 2 ns intervals by the FADCs, as well as GPS timestamps and trigger information. Additional information about the observing runs is stored in the VERITAS database, including pointing information, information regarding weather conditions and references to associated calibration runs. The

Event Display analysis procedures use all of this information to detect sources and produce skymaps, light curves, flux measurements and spectra, an overview of which is presented here:

- Prior to the analysis, the data runs on a given source are selected, and the quality of those runs is evaluated. Based on the quality evaluations, entire runs or sections of runs are excluded from the analysis.
- The analysis begins by analyzing events in the data runs that are produced by forced L3 triggers occurring at 3 Hz, called pedestal events. The analysis of these events allows the determination of the signal recorded for each PMT channel in the absence of Cherenkov light, called the pedestal.
- The trace samples of the shower events are summed in order to obtain an intensity value or *charge* for each pixel, expressed in units of 'digital counts' (DC).
- The pedestal is subtracted from the *charge* of the pixels to produce images of pedestal-subtracted *charge*.
- Pixels that are not likely to be part of the shower image are suppressed in a process known as image cleaning.
- The sum of the *charge* of the pixels in the cleaned images is calculated, resulting in a parameter proportional to the amount of Cherenkov light incident on the cameras, called *size*, also expressed in units of DC.
- The cleaned shower images are then analyzed with a moment analysis, resulting in elliptical parametrizations of the shower images, from which various quantities are derived. The parametrizations allow the arrival directions of the

gamma-ray candidate primaries to be determined, as well as the shower core locations (see section 5.8).

- Certain image parameters are compared to those of simulated gamma-ray showers, resulting in parameters that quantify the extent to which the showers resemble gamma-ray showers. Cuts on these parameters are used to remove most of the dominant background of hadronic showers.
- In order to estimate the energies of the gamma-ray candidate events, lookup tables produced by gamma-ray shower simulations are used to relate the measured *size* values and shower core locations to the energies of the primaries.
- Sky maps are produced using the calculated arrival directions of the gamma-ray candidate events and the telescope pointing information stored in the VERITAS database.
- Sources are found by finding a statistically significant excess number of gamma-ray candidate events from certain directions of the sky compared to others.
- The fluxes and spectra (or upper limits) from such sources (or putative sources) are determined using the measured gamma-ray candidate event rates and energies and instrument response functions called effective areas, produced from simulated gamma rays.
- Pulsar analyses may be performed using the GPS timestamps.

This chapter describes these procedures in detail.

5.2 VERITAS data quality monitoring

The evaluation of the quality of the data runs taken by VERITAS is accomplished with a web-based tool, the VERITAS data quality monitoring (DQM) website. The VERITAS DQM website displays plots of various quantities of interest, including trigger rates, currents, dead time and telescope pointing information. The plots are produced using an automated analysis pipeline that performs a VEGAS analysis on recently acquired runs and produces the plots using macros designed for this purpose. Analysts may then evaluate the quality of the data by looking at the plots, and use the website to write data quality evaluations to the VERITAS database. Problems with the hardware are often identified in this process. The VERITAS DQM website is generally used prior to an analysis to remove runs and time intervals within runs deemed to be of poor quality due to hardware failures and atmospheric conditions such as clouds.

5.3 VERITAS calibration measurements

In order to produce useful science results from the VBF files, calibration measurements must be performed. This section will briefly describe the various calibration measurements that are taken.

5.3.1 Flasher runs

Each pixel of the VERITAS cameras has different light response and timing properties due to varying cable lengths, PMT properties and FADC channel properties. In order to calibrate out these effects, calibration runs are taken regularly where the cameras are illuminated uniformly with flashes of light produced by LED light sources called flashers [71]. Flasher runs trigger both the flasher and the data

acquisition system at a rate of 300 Hz, ensuring that the flashes occur within the FADC readout widow. When triggered, the flasher emits a flash of blue light several nanoseconds in duration, comparable to the properties of the Cherenkov light emitted by air showers. The light level emitted by the flasher is varied for each new trigger, cycling through seven intensity levels. The assumption underlying the analysis of these runs is that each channel receives the same amount of light, and the light arrives at all the channels simultaneously. Using this assumption, the different light responses and timing properties of the channels can be determined. The light responses (relative gains) of the PMTs are used to flat-field the camera by adjusting the voltage of each PMT in order equalize the gains. The relative gains are also used to correct the light response of the PMTs as part of the standard data analysis procedures. The timing response of the PMTs as determined from the analysis of the flasher runs is also corrected for as part of the standard analysis procedures.

5.3.2 Reflectivity monitoring

The full-dish reflectivity of the VERITAS reflectors is monitored regularly using optical reflectivity cameras that are mounted to the OSS at one of the mirror facet locations. For these measurements, a plate is mounted to the VERITAS cameras with a highly reflective spectralon screen attached. The telescope is pointed to a star and the reflectivity camera takes images of both the star and the reflection of the star on the spectralon screen in the camera plane. Using simple geometrical arguments, one can derive the full-dish reflectivity from these measurements. A filter wheel allows red, green and blue filters to be placed in front of the reflectivity camera, which allows the wavelength dependence of the full-dish reflectivity to be measured.

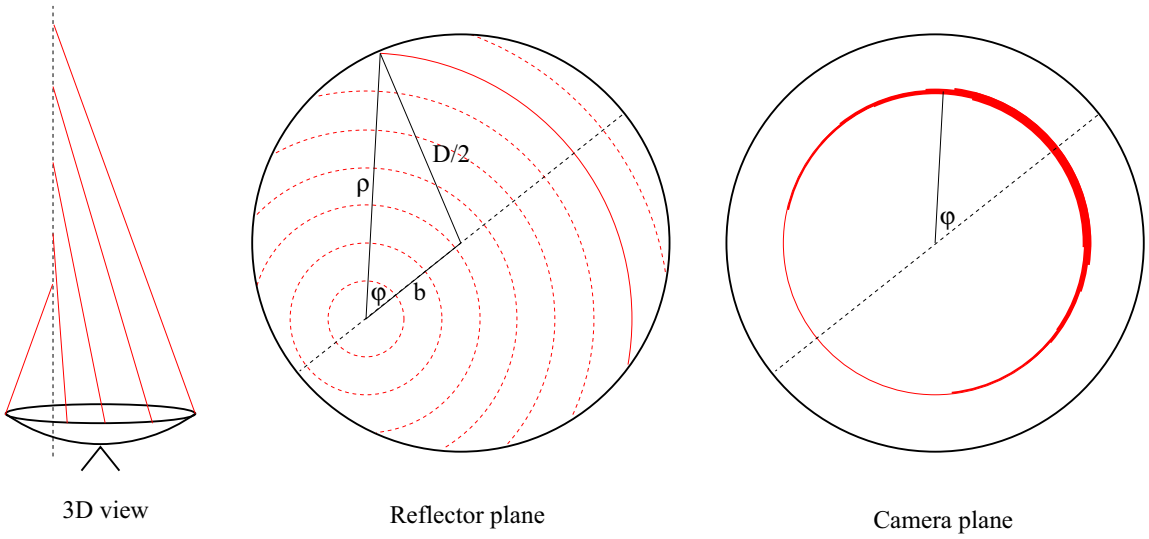

Figure 5–1: Muon event geometry for a muon hitting the reflector, parallel to the optical axis. Figure modified from [60].

The wavelength-dependent reflectivity of individual mirror facets is also periodically monitored using the on-site VERITAS mirror laboratory. Reflectivity measurements are used to model the reflectors in the VERITAS detector simulations, which are discussed in section 5.9.

5.3.3 Muons

VERITAS regularly detects single muons as part of normal data taking. The Cherenkov light emitted by muons is emitted in a cone at an approximately constant angle as the muon travels through the atmosphere. Since the VERITAS reflectors convert angles of incidence into positions in the camera plane, muons produce ring shaped images in the camera plane (see Figure 5–1). Muons with impact parameters b less than the radius of the reflectors produce full rings in the camera plane. Muons with impact parameters greater than the radius of the reflectors produce incomplete

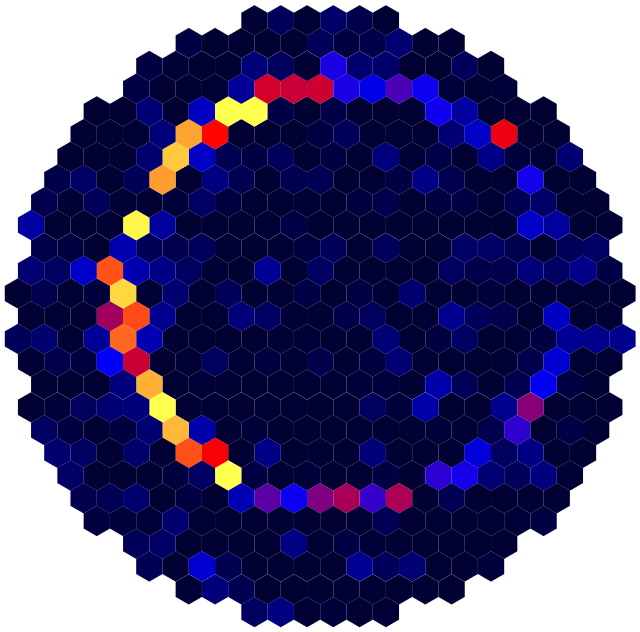

Figure 5–2: A muon event recorded by VERITAS. The colour of the pixels represents the *charge* calculated for each PMT. Lighter colours correspond to higher *charge* values. Figure from [60].

rings or arcs. Figure 5–2 shows a muon event recorded by VERITAS. The radius of the ring in degrees corresponds to the Cherenkov angle of the muon. The circular images produced by muons may be identified using various techniques [112] [121]. Muons may be used for calibration purposes, since the amount of Cherenkov light received from a muon with a given Cherenkov angle and impact parameter is expected to be constant, and can be related to the *size* of the muon ring images [55]. Muon calibration information provides measurements of the average optical response of a given telescope, and can be used to verify other calibration measurements such as full-dish mirror reflectivity.

5.3.4 High/low gain ratio calibration

As mentioned in section 4.5.5, the dynamic range of the VERITAS FADCs is extended by use of the high/low gain switch. In order to measure the low-gain pedestals and the ratio of the gains of the high-gain and low-gain amplifiers (called the high/low gain ratio), special flasher runs are taken. For these runs, half of the PMTs in the cameras are set to a low voltage so that no channels switch into low gain mode, and half of the camera is set to a high voltage so that a combination of gain states is achieved as a result of the flashes. For each channel placed at high voltage, the *charge* values obtained as a result of the flashes are plotted vs. the average *charge* value recorded by the low voltage PMTs. Another run is taken with the high and low voltages reversed in order to obtain measurements for all of the channels. Two distributions appear on the plots with distinct slopes corresponding to the high and low gain states. For a given channel, the ratio of the slopes of the two distributions corresponds to the high/low gain ratio. The readout window for these runs is increased to 128 samples in order to obtain low-gain pedestal measurements, far from the flasher pulses in the readout window. Array-averaged high/low gain ratio measurements are used in the analysis software to correct for the attenuation of the signal due to passing through the low gain amplifier.

5.3.5 Single photoelectron runs

The response of the PMTs, cables and data acquisition electronics of each channel to a single photoelectron, called the DC/PE ratio, is determined with special calibration runs [70]. Flasher runs are taken with metal plates in front of the cameras with small holes at the positions of the PMTs, in order to attenuate the light

from the flashes and night sky background such that single photons are frequently incident on the PMTs. Histograms can be made of the *charge* values obtained as a result of the flashes for each channel. Analysis of these histograms allows the DC/PE ratio for each channel to be determined. These measurements are used as part of the VERITAS detector simulations.

5.3.6 Optical monitoring

An optical monitoring system, the VERITAS pointing monitors, is used to measure the pointing of the VERITAS telescopes during observations. The pointing monitors consist of a computer mounted on each OSS, an optical camera facing the PMTs, and an optical camera facing the sky, in the pointing direction of the telescopes. Images taken regularly of the stars in the pointing directions of the telescopes during observations are used to derive the pointing directions of the telescopes to arcsecond precision. The pointing directions obtained from the images are saved to the VERITAS database every two seconds, and are used by the VERITAS analysis software to make skymaps. The pointing monitors are also used to characterize the optical point spread function (PSF) of the telescopes by taking images of the reflections of stars on a reflective screen placed over the PMTs. The image of the star in the focal plane consists of 350 superimposed images of the star, one from each mirror facet. If the measured optical PSF determined from the images becomes too broad (approximately the size of a VERITAS PMT), this indicates the need for mirror alignment. Finally, the pointing monitors are used to measure and correct the pointing calibration of the VERITAS tracking software.

5.4 Analysis of pedestal events

As mentioned in section 4.5.5, the data acquisition system forces L3 triggers at a rate of 3 Hz. The resulting events, called pedestal events, are tagged so that they may be identified by the analysis software. The analysis of these events allows the determination of the signal recorded for each PMT channel in the absence of Cherenkov light, called the pedestal. The traces of the pedestal events are summed over various numbers of samples (integration window lengths) in order to obtain an integrated pedestal value for each integration window length for each channel. The mean integrated pedestal values and the standard deviation of the integrated pedestal values (integrated *pedvar*) for each integration window length are computed from these quantities using the pedestal events, in three minute time bins. The mean pedestal and *pedvar* values for the channels may vary considerably throughout the run due to changing observing conditions. These values are used later for pedestal subtraction and image cleaning, which are described in section 5.6. As mentioned in section 5.3.4, low-gain pedestal values are determined from the high/low gain calibration runs.

5.5 FADC trace analysis

Once the pedestal events have been analyzed, the FADC traces of the non-pedestal events are analyzed in order to determine the magnitude of the signals recorded by each PMT. For channels where the high/low gain switch fired, the low gain pedestal value for the channel is first subtracted from each sample of the trace. Each sample is then multiplied by an array-averaged high/low gain ratio measurement (see section 5.3.4) in order to correct for the attenuation of the signal due to

having passed through the low gain amplifier. The low gain pedestal value is then added back to the trace. For each channel, a subset of the trace samples (called the integration window), are then summed in order to obtain a parameter proportional to the amount of light incident on each PMT in the time interval corresponding to the integration window, the *charge*. Event Display uses a double-pass procedure to determine optimal integration windows for the channels, which maximizes the signal to noise ratio of the Cherenkov signal. In the first pass, the times t_0 at which the traces reach 50 percent of their maximum values are determined, and the traces are then integrated using a 10-sample integration window, starting at t_0. Pedestal subtraction, cleaning and relative gain adjustments are then performed, as described in section 5.6. This results in a first-pass shower image, which is analyzed to determine the location of the shower axis in the image. The timing corrections determined by a flasher run (described in section 5.3.1) are applied to the t_0 values, and a linear fit of the corrected t_0 values for the shower image pixels as a function of position along the shower axis is performed. This fit and the flasher timing corrections are used to calculate the optimal start of the integration windows for the second pass. The second pass integration is performed using a 6-sample integration window, starting at the time determined from the aforementioned timing analysis, resulting in a *charge* value calculated for each PMT. Figure 5–3 (left) shows the resulting raw shower image, where the colours of the pixels represent the *charge* of the PMTs.

5.6 Pedestal subtraction, image cleaning and *charge* calibration

Following the trace analysis, the images are processed in order to produce background subtracted, cleaned and calibrated images. The background signal for each

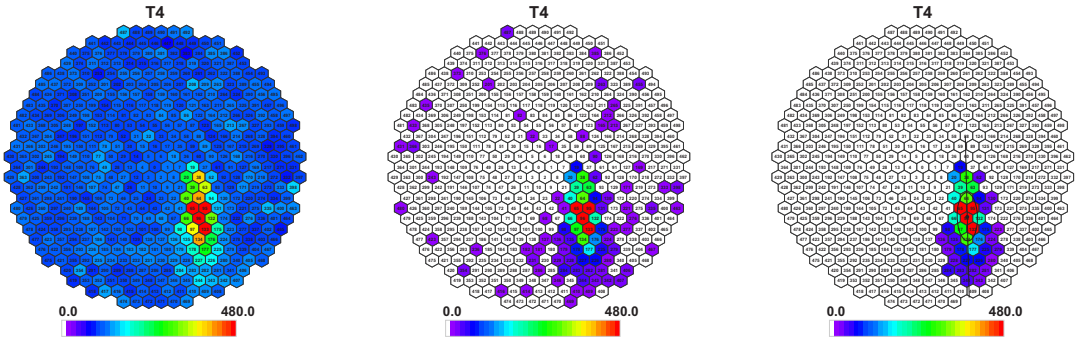

Figure 5–3: A raw shower image (left), after pedestal subtraction (middle) and after image cleaning (right). Figures from [91].

pixel is first removed by subtracting the 6-sample integrated pedestal values determined for each pixel from the *charge* values, resulting in pedestal-subtracted *charge* values for each pixel. Figure 5–3 (middle) shows a shower image after pedestal subtraction, where the colours of the pixels represent the pedestal subtracted *charge* values calculated for each pixel. Following the pedestal subtraction, pixels that are not likely to be part of the shower image are suppressed, a process called image cleaning. Several cleaning methods have been devised, including *charge* threshold cleaning and signal-to-noise cleaning, where the cleaning threshold for each channel is calculated based on the integrated *pedvar* value for that channel. The standard Event Display analysis uses the latter method, which has the advantage of being less sensitive to changing night sky brightness. For the purposes of cleaning, two types of pixels are defined: image and border pixels. Image pixels are defined as pixels with pedestal-subtracted *charge* values greater than 5 σ, where σ is the 6-sample integrated *pedvar* value defined for that pixel. Border pixels are defined as pixels

adjacent to image pixels with pedestal-subtracted *charge* values between 2.5 σ and 5 σ. Pixels that are found to be neither image or border pixels have their *charge* set to zero. Figure 5–3 (right) shows a shower image after image cleaning. Following cleaning, the *charge* values of the image and border pixels are adjusted using the relative gain measurements from a flasher run to obtain calibrated shower images. Pixels are also removed from the analysis based on the measured pedestal values, pedestal variations, relative gains, relative gain variances and timing corrections. These pixels are assigned *charge* values based on the average *charge* values of their neighbouring image and border pixels.

5.7 Image parametrization

Following pedestal subtraction, image cleaning and calibration, a moment analysis is performed on each shower image, resulting in elliptical parametrizations of the shower images. Figure 5–4 shows the geometry of an elliptical parametrization of a shower image. Parameters such as the location of the image centroid, the orientations of the major and minor axes, the RMS spread of the pixel distribution along the minor axis (*width*) and the RMS spread of the pixel distribution along the major axis (*length*) are determined from the moment analysis. The *charge* values of the image and border pixels are summed in order to calculate the *size* parameter, a measure of the total amount of Cherenkov light detected from the shower for a given telescope. In addition, an averaged *pedvar* value for each shower image is calculated using the image and border pixels, and one layer of pixels surrounding them. These parameters are used later in the analysis for direction and core location reconstruction, gamma/hadron separation and energy reconstruction. This technique

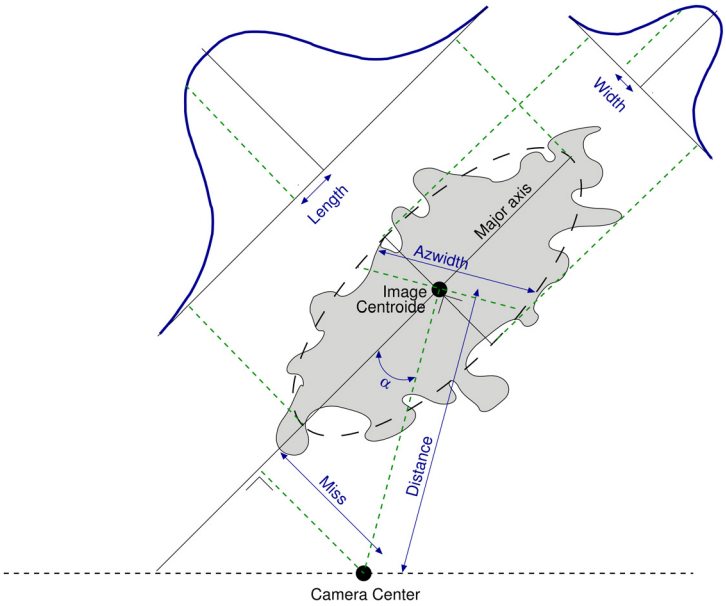

Figure 5–4: A diagram of an elliptical parametrization of an air shower image, showing the *length* and *width* parameters. Figure from [91].

of shower image parametrization was developed by Hillas in 1985 [76] and led to the first discovery of an astronomical source of gamma rays using a ground based instrument [57].

5.8 Event reconstruction

Event reconstruction refers to the reconstruction of the arrival direction and core location of the shower, which together define the 3D location of the shower axis with respect to the array. Several image quality cuts are implemented prior to event reconstruction in order to improve the reconstruction accuracy by discarding low quality images. Image quality cuts implemented in Event Display include cuts on *size*, *width*, the total number of image and border pixels, the fraction of the *size* of the image located at the edge of the camera, and the distance of the image centroid

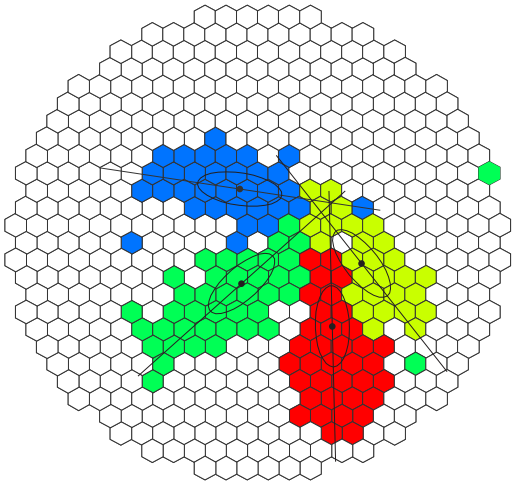

Figure 5–5: A diagram showing the direction reconstruction technique used in Event Display. The images from multiple telescopes are superimposed, and the best-fit convergence point of the lines extending from the major axes of the elliptical image parametrizations corresponds to the reconstructed arrival direction of the shower with respect to the pointing position of the array. Figure from [91].

from the center of the camera. A minimum of two telescope images remaining after these quality cuts have been applied is required for the event to be reconstructed and used in the analysis. For events with two images, a minimum angle between the two major axes is required in order to ensure that the direction and core location are accurately reconstructed.

Following the image quality cuts, the parametrizations of the remaining images for each event are used to reconstruct the arrival direction and core location of the shower. The arrival direction of the shower with respect to the array pointing direction is determined by superimposing the shower images and determining the best-fit convergence point of the lines extending from the major axes of the elliptical parametrizations (see Figure 5–5). The best-fit convergence point is found by taking

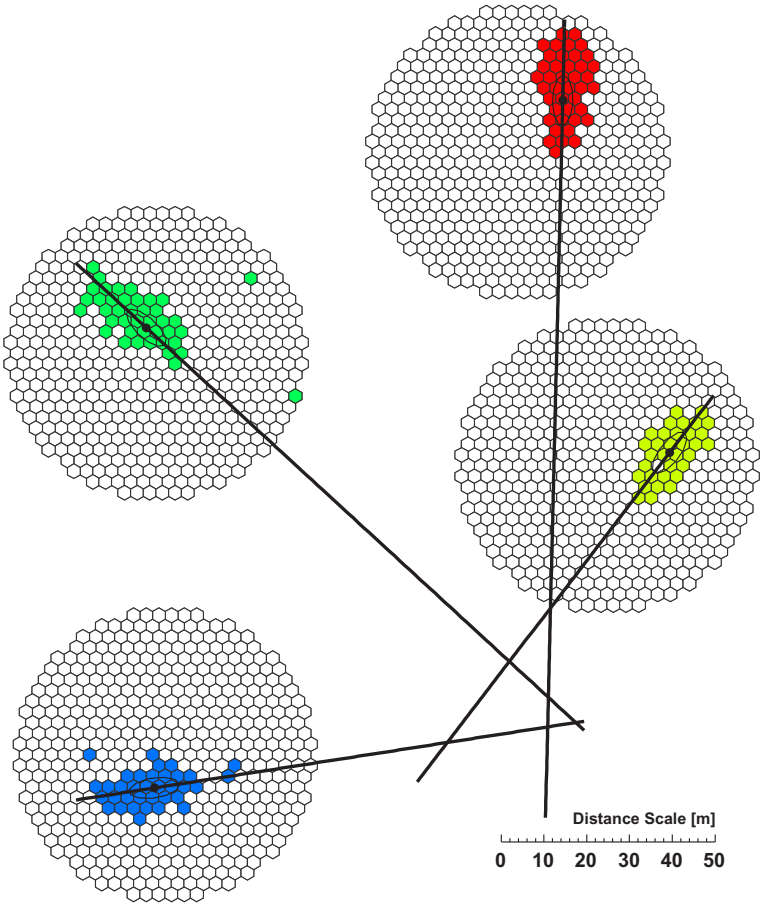

Figure 5–6: A diagram showing the shower core location reconstruction technique used in Event Display. The telescope locations on the ground are projected onto a plane perpendicular to the reconstructed arrival direction (the shower plane), and lines following the major axes of the shower images are projected onto this plane, at the locations of the telescopes. The location of the best-fit convergence point of the lines corresponds to the reconstructed core location. See text for details. Figure from [91].

a weighted average of the intersection points of each pair of lines. The weights are determined by the *size*, and $\frac{length}{width}$ values of the two shower images, and the sine of the angles between the lines. The shower core location is determined from the image parameters and the reconstructed arrival direction of the shower. Improved estimates of the shower image axis orientations are first obtained by using the lines that pass through the centroids of the shower images and the reconstructed arrival direction as the new major axes. The telescope locations on the ground are then projected onto a plane perpendicular to the reconstructed arrival direction (the shower plane), and lines following the major axes of the shower images are projected onto this plane, at the locations of the telescopes. The location of the best-fit convergence point of the lines corresponds to the core location (see Figure 5–6). The best fit convergence point is found by taking a weighted average of the intersection points of each pair of projected lines, using the same weights that are used in the direction reconstruction. The distance in the shower plane from a given telescope to the core location is called the impact parameter, and is calculated for each telescope. The impact parameters are used later in the analysis to estimate the energies of the showers.

5.9 VERITAS simulations

Simulations are used in order to develop criteria to distinguish gamma-ray-initiated showers from the background of hadronic showers, estimate the energies of the gamma-ray showers and estimate fluxes from detection rates. For the Event Display analyses described in this thesis, electromagnetic and hadronic air showers and the Cherenkov photons emitted by the atmosphere as a result of them are simulated with a program called CORSIKA [48]. The propagation of the simulated Cherenkov

photons through a model of the detector and data acquisition system is accomplished with a program called GRISUdet [88] [27]. CORSIKA implements detailed simulations of air showers by tracking the creation, propagation and interactions of the air shower particles in the atmosphere. The showers are generated randomly over a 750 m x 750 m area, at random azimuthal angles and at particular zenith angles: 0°, 20°, 30°, 35°, 40°, 45°, 50°, 55°, 60°, 65°, with five million showers generated for each zenith angle. The showers are generated between the energies of 30 GeV and 200 TeV, following a power law spectrum with a spectral index of 2. The VERITAS simulations use atmospheric density and light transmission profiles calculated using the MODTRAN [41] program, and local radiosonde measurements in order to model the interaction of the shower particles with the atmosphere and the emission and propagation of the Cherenkov photons to the ground. The output of the CORSIKA simulations consists of files that contain the wavelengths, arrival directions and locations on the ground of the Cherenkov photons emitted by the atmosphere as a result of the simulated showers. Each Cherenkov photon is also tagged with the identity of the particle that initiated the air shower responsible for that photon. These files are used as input for the VERITAS detector simulations, which propagate the simulated Cherenkov photons though a model of the VERITAS detector. The detector simulation used for the analysis described in this thesis, GRISUdet, simulates the telescope optics, light cones, PMTs, cables, trigger systems and data acquisition systems in order to produce VBF files from the simulated Cherenkov photons produced by CORSIKA. The VBF files may be then analyzed with the standard VERITAS analysis software in order to produce instrument response functions (IRFs) that

allow background rejection, energy estimation and flux calculations, described in sections 5.10, 5.11 and 5.14. The limitations of the simulations include the use of the same reflectivity and quantum efficiency curves for multiple mirror facets and PMTs, as well as simplified models of the trigger and data acquisition systems. Important sources of systematic uncertainty include the amount of Cherenkov light production and extinction in the atmosphere, mirror reflectivities, PMT quantum efficiencies and gains, the data acquisition system model and the analysis methods. The total systematic uncertainty on the light collection efficiency is estimated to be approximately 20%. This leads to a systematic uncertainty of approximately 20% on the energy estimates of the showers (see section 5.11). The systematic uncertainty on the flux measurements is estimated to be approximately 20% for a source with a power-law spectrum with a spectral index of 2.4 and approximately 40% for a source with a power-law spectrum with a spectral index of 3.8 (see section 5.14).

5.10 Gamma/Hadron separation

In order to discriminate electromagnetic showers from the background of hadronic showers (called gamma-hadron separation), shower image parameters are compared to parameters obtained from simulated electromagnetic shower images. This is accomplished by using lookup tables produced from the analysis of electromagnetic shower simulations (see section 5.9). The lookup tables for each telescope consist of histograms of *size* vs impact parameter for various observation zenith and azimuth angles, direction offset angles from the camera center and averaged *pedvar* values. The bin values of these histograms correspond to the median *length* and *width* values, $length_{MC}$ and $width_{MC}$, calculated for the simulated showers for various *size*,

impact parameter, offset angle and averaged *pedvar* bins. Similar lookup tables are made for the standard deviations of the distributions of the *length* and *width* values used to determine the $length_{MC}$ and $width_{MC}$ values, $\sigma_{length_{MC}}$ and $\sigma_{width_{MC}}$. For observational shower data, the calculated *length* and *width* values of the showers are compared to the $length_{MC}$ and $width_{MC}$ values from the lookup tables in order to quantify the extent to which the shower images resemble electromagnetic shower images. Specifically, the parameters *mean scaled width* (*mscw*), and *mean scaled length* (*mscl*) are calculated for each event in the following way:

$$mscl = \frac{1}{N_{images}} \sum_{i}^{N_{images}} \frac{length_i \; - \; length_{MCi}}{\sigma_{length_{MCi}}}$$

$$mscw = \frac{1}{N_{images}} \sum_{i}^{N_{images}} \frac{width_i \; - \; width_{MCi}}{\sigma_{width_{MCi}}}.$$

Figure 5–7 shows the distributions of *mscl* (left) and *mscw* (right) values for simulated electromagnetic and hadronic showers as well as data consisting of gamma rays from the Crab nebula and cosmic rays. Cuts on these parameters allow the preferential selection of electromagnetic showers over the dominant background of hadronic showers. The mean scaled parameters have proven to be the most useful parameters devised for accomplishing this, and were first described in [50]. Other cuts used for gamma-hadron separation include the calculated height of shower maximum, which is calculated using simple geometrical arguments, and the *size* of the second brightest shower image of an event, *2ndSizeMax*.

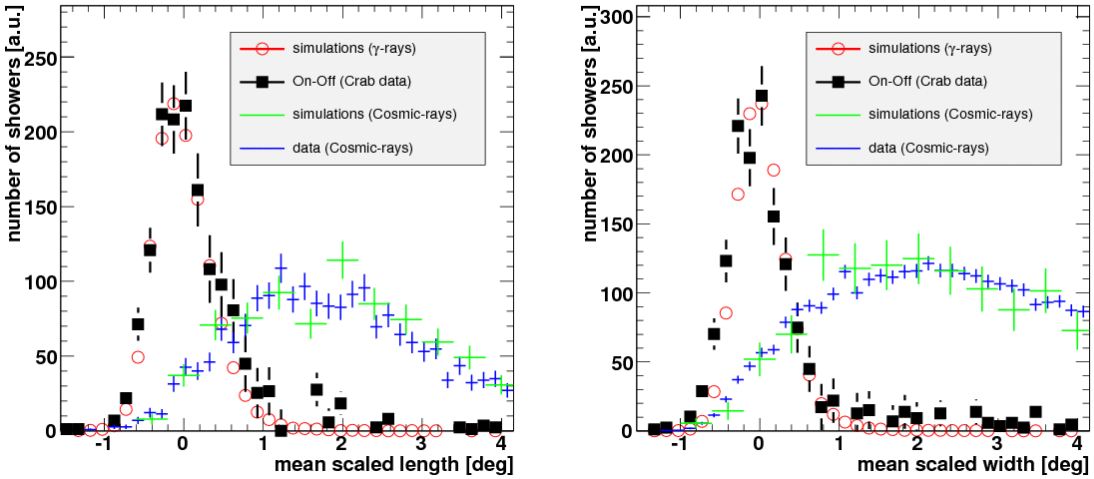

Figure 5–7: The distributions of *mscl* (left) and *mscw* (right) values for simulated electromagnetic and hadronic showers as well as data consisting of gamma rays from the Crab nebula and cosmic rays. The red circles represent simulated electromagnetic showers and the green crosses represent simulated hadronic showers. The black squares represent showers from the direction of the Crab nebula with the expected cosmic ray background subtracted, and the blue crosses represent cosmic ray data. Cuts on these parameters allow the preferential selection of electromagnetic showers over the dominant background of hadronic showers. Image credit: Gernot Maier.

5.11 Energy estimation

The energies of the showers are estimated in a similar way as the procedure described in the previous section: by using lookup tables produced from the analysis of electromagnetic shower simulations (see section 5.9). The lookup tables for each telescope consist of histograms of *size* vs impact parameter for various observation zenith and azimuth angles, direction offset angles from the camera center and averaged *pedvar* values. The bin values of these histograms correspond to the median energy $< E >$ calculated for the simulated showers for various *size*, impact parameter, offset angle and averaged *pedvar* bins. Similar lookup tables are made for the standard deviations of the distributions of the energy values used to determine the $< E >$ values, σ_E. In order to estimate the energy of a shower using the information from all of the images, a weighted mean of the $< E >$ values determined for each image is calculated, where the σ_E values are used as weights:

$$E = \frac{\sum_{i}^{N_{images}} (< E_i >)(\sigma_{E_i})^{-2}}{\sum_{i}^{N_{images}} (\sigma_{E_i})^{-2}}.$$

5.12 Signal extraction

Once gamma-ray candidate events have been identified and their arrival directions and energies estimated, a search is performed for a statistically significant excess number of showers from particular directions in the field of view; such an excess may represent a gamma-ray signal. Specifically, regions of the sky may be defined where a gamma-ray signal is expected (the signal or 'on' region), and other regions of the

sky where no signal is expected, from which the background signal is estimated (the background or 'off' regions). The signal region consists of a circular region around a putative gamma-ray source, with an area defined by the Θ^2 parameter, the square of the angle subtended by the radius of the circular signal region in degrees. The background region can be defined in various ways, the most common being the reflected region and ring background methods, discussed later in this section.

In order to determine the number of excess gamma-ray candidate events in the signal region if any, the number of counts in the background region is scaled by the ratio of the acceptances of the signal and background regions and subtracted from the number of counts in the signal region:

$$N_{Excess} = N_{On} - \alpha N_{Off}$$

where N_{Excess} is the calculated excess in the signal region, N_{On} is the number of counts in the signal region, α is the ratio of the acceptances of the signal and background regions, and N_{Off} is the number of counts in the background regions. Since N_{On} and N_{Off} are independent measurements, the variance of the excess can be calculated as: $\sigma^2(N_{Excess}) = \sigma^2(N_{On}) + \alpha^2\sigma^2(N_{Off})$. Assuming Poisson statistics, an estimate for the standard deviation of the excess can be approximated as:

$$\sigma(N_{Excess}) = \sqrt{\sigma^2(N_{On}) + \alpha^2\sigma^2(N_{Off})} = \sqrt{N_{On} + \alpha^2 N_{Off}}.$$

The significance may be approximated by the ratio of the number of excess counts divided by the standard deviation of the number of excess counts [83]:

$$S \quad = \quad \frac{N_{Excess}}{\sigma(N_{Excess})} \quad = \quad \frac{N_{On} - \alpha N_{Off}}{\sqrt{N_{On} + \alpha^2 N_{Off}}}.$$

A more sophisticated treatment by Li and Ma [83] using a maximum likelihood method gives:

$$S = \sqrt{2}\Big\{ N_{on} \ln \Big[\frac{1+\alpha}{\alpha} \Big(\frac{N_{on}}{N_{on} + N_{off}} \Big) \Big] \; + \; N_{off} \ln \Big[(1+\alpha) \Big(\frac{N_{off}}{N_{on} + N_{off}} \Big) \Big] \Big\}^{\frac{1}{2}} \quad (5.1)$$

where the sign of the significance is given by the sign of $N_{On} - \alpha N_{Off}$. This equation is used to calculate the significance of gamma-ray signals measured by VERITAS. A significance of five standard deviations or above is generally required to claim a detection.

The acceptance of gamma-ray candidate events varies as a function of the reconstructed arrival directions in the field of view. Specifically, the acceptance decreases as a function of the distance from the center of the camera, and to a lesser extent, varies as a function of zenith angle. In order to model the acceptance variations across the camera, acceptance functions derived from the analysis of data or simulations may be used. Event Display currently uses acceptance functions that assume azimuthal symmetry (radial acceptances) that are produced from observations with no strong gamma-ray source present in the field of view.

In order to take advantage of the approximate azimuthal symmetry of the camera acceptance to simplify α calculations, runs are taken with the putative gamma-ray source offset from the center of the camera by a fixed angle, a configuration called wobble observation mode. Observing runs alternate between positive and negative offsets in elevation and azimuth called north, south, east and west wobbles. As the wobbles are alternated, regions of the camera that were previously signal regions become background regions, reducing any systematic effects associated with particular regions of the camera. The offset angle, called the wobble offset, is typically 0.5 degrees.

The reflected-region background method uses several circular regions, each of which have the same area as the signal region, placed at the same offset from the center of the camera as the wobble offset, as shown in Figure 5–8, (right). The alpha calculation then proceeds with the assumption that the circular background regions all have the same acceptance as the signal region. This simplifies the alpha calculation to $\alpha = \frac{1}{N_{BR}}$, where N_{BR} is the number of background regions, and does not require the use of radial acceptances. The ring background method uses an annular background region surrounding the signal region, as shown in Figure 5–8, (left). In this case, α is calculated by taking the ratio of the integral of the radial acceptance over the signal region to the integral of the radial acceptance over the background region:

$$\alpha = \frac{\int_{On} A(r)dA}{\int_{Off} A(r)dA}$$

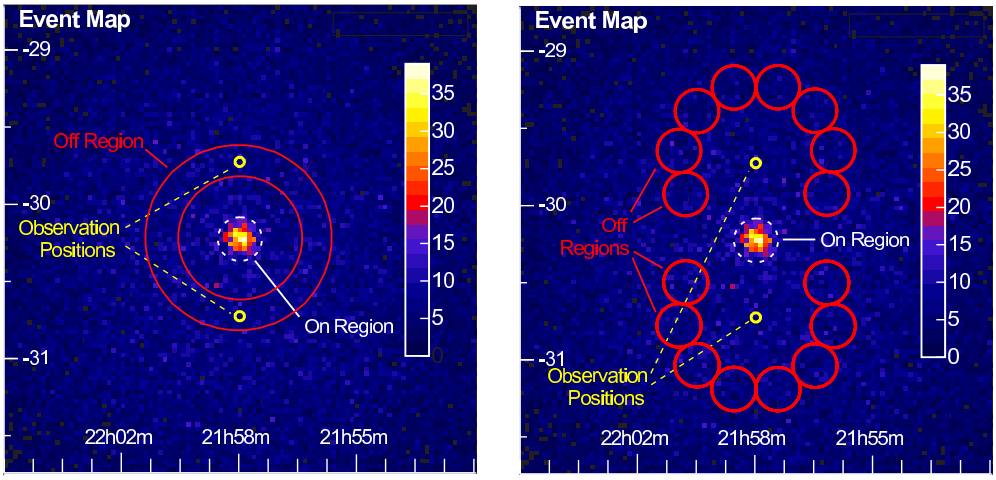

Figure 5–8: Background estimation methods. Left: the ring background method. The background region is an annular region surrounding the signal region. Right: The reflected regions method. The background region consists of several circular Θ^2-sized regions offset from the telescope pointing direction by the same angle as the wobble offset. Figure from [11].

where $A(r)$ is the radial acceptance.

5.13 Skymaps

The gamma-ray candidate events may be used to produce skymaps, 2D histograms of the arrival directions of the gamma-ray candidate events in right ascension (RA) and declination (dec), where the value of the bins is proportional to the gamma-ray signal from that direction of the sky. The arrival directions of the gamma-ray candidate events calculated with respect to the pointing direction are converted into RA and dec using pointing information stored in the database by the VERITAS pointing monitors. Simple skymaps can be made by counting the number of gamma ray candidate events that fall into each RA and dec bin. This kind of skymap is called an uncorrelated counts map, as the values of the bins correspond to the number of

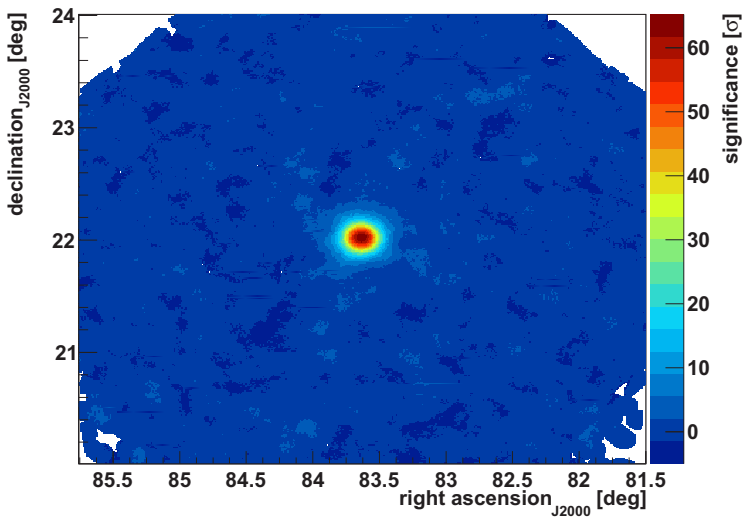

Figure 5–9: A correlated significance skymap produced with six hours of VERITAS Crab nebula data.

gamma-ray candidate events in the bin, and the bin values are independent. Uncorrelated significance maps can be made by using either of the background estimation methods described in section 5.12. Uncorrelated skymaps can be useful for the analysis of extended sources, however the bins are much smaller than the gamma-ray point spread function (PSF) and they can be quite sparse, with many unfilled bins. The standard skymaps produced by VERITAS analyses are smoothed using the Θ^2 parameter, where all of the events within a Θ^2-sized circle around each bin center are counted in the bin. These are called correlated skymaps, because the value of a particular bin is correlated with the values of the neighboring bins. Correlated significance maps can be made using either of the background estimation methods described in section 5.12. *Event display* uses 400x400 2D histograms by default to produce skymaps, although this may be modified by the user. Figure 5–9 shows a

correlated significance map of the Crab nebula produced with data from six hours of observations using the reflected regions background method. The Crab nebula can clearly be seen in the middle of the skymap, with a significance of $\sim 65\ \sigma$. The size of the Crab nebula in the skymap corresponds to the VERITAS PSF, as the extension of the Crab nebula in VHE gamma rays is smaller than the PSF.

5.14 Spectral reconstruction and upper limits

In order to calculate fluxes or flux upper limits from excess gamma-ray candidate events or excess upper limits, instrument response functions called effective areas are used. Effective areas can be thought of as gamma-ray reconstruction efficiencies, and are a function of energy, zenith angle, averaged *pedvar*, cuts and source spectral index. Effective areas are produced from the analysis of electromagnetic shower simulations by multiplying the area over which the showers are generated by the ratio of the number of reconstructed showers to the number of thrown showers:

$$A_{Eff}(E) = A_{Thrown}\frac{N(E)_{Reconstructed}}{N(E)_{Thrown}}$$

The effective areas can then be used to calculate a differential energy spectrum in the case of a detection:

$$\frac{dF(E)}{dE} = \frac{N(E)_{Excess}}{A_{Eff}(E)T_{Live}dE}$$

where $\frac{dF(E)}{dE}$, (sometimes expressed as $\frac{dN(E)}{dE}$) is the differential flux in the spectral bin at energy E, $N(E)_{Excess}$ is the number of excess events (or upper limit) in the

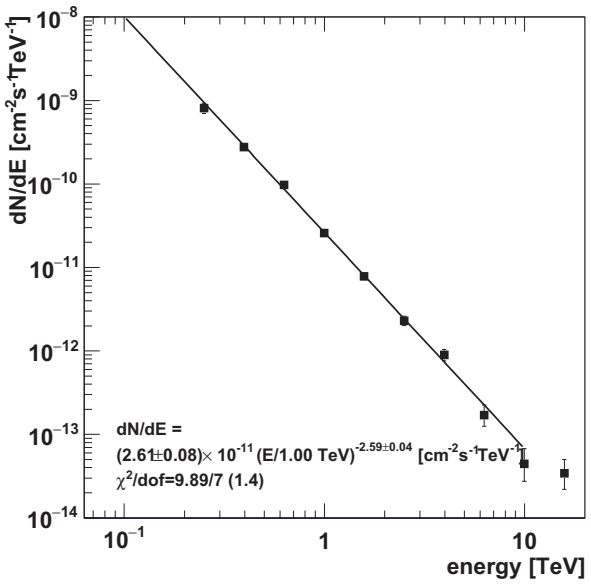

Figure 5–10: A differential energy spectrum produced from six hours of Crab nebula data. The solid line represents a power law fit to the data.

energy bin, $A_{Eff}(E)$ is the effective area at energy E (a time weighted average over the observing runs), T_{Live} is the live time (the observing time minus the dead time), and dE is the bin width. Generally, when the significance of the excess for a given energy bin is below 3 σ, an upper limit is calculated. A spectrum produced in this way can be fit with an assumed spectral shape, such as a power law or power law with an exponential cutoff, in order to obtain parameters of interest such as spectral indices and break energies. Figure 5–10 shows a spectrum of the Crab nebula produced by this method. In order to calculate the integral flux above a certain energy, the fitted spectral shape is integrated. For the case of a power law fit, where $\frac{dF}{dE} = F_0\Big(\frac{E}{E_0}\Big)^{-\Gamma}$, the integral flux is calculated in the following way:

$$F(E > E_{Th}) = \int_{Eth}^{\infty} \Big(\frac{dF}{dE}\Big) dE = \int_{Eth}^{\infty} F_0 \Big(\frac{E}{E_0}\Big)^{-\Gamma} dE.$$

In the case where no signal is detected, an upper limit on the number of excess events is calculated and a spectral shape is assumed (generally, a power law with an assumed spectral index) in order to calculate differential and integral flux upper limits. Number upper limits can be calculated using the N_{On}, N_{Off} and α values and a specified confidence level. Different methodologies, such as the methods of Helene [75], Feldman-Cousins [61] and Rolke [106] are available and can be specified by the user. In the case of a power law, an upper limit on the differential flux normalization constant, $F_{0(Ul)}$ is calculated in the following way:

$$F_{0(Ul)} = \frac{N_{(Ul)}(E > E_{Th})}{\int_{Eth}^{\infty} \Big(\frac{E}{E_0}\Big)^{-\Gamma} A_{Eff}(E) dE \ \cdot T_{Live}}$$

where E_{Th} is an energy threshold above which to perform the analysis and $N_{(Ul)}(E > E_{Th})$ is the upper limit on the number of excess events above E_{Th}. Various definitions of E_{Th} exist, such as the energy where the effective area falls to a specified value, the energy where a specified energy bias condition is met, or the energy where a peak in the convolution of the spectrum with the effective area curve occurs. With $F_{0(Ul)}$, E_{Th} and the assumed spectral index Γ, the power law spectrum can be integrated in order to calculate an integral flux upper limit:

$$F_{(Ul)}(E > E_{Th}) = \int_{Eth}^{\infty} \Big(\frac{dF}{dE}\Big) dE = \int_{Eth}^{\infty} F_{0(Ul)} \Big(\frac{E}{E_0}\Big)^{-\Gamma} dE.$$

5.15 Pulsar analysis

Pulsar analysis with VERITAS involves searching for the periodic signals emitted by pulsars using the GPS timestamps assigned to the events. As mentioned in section 4.5.7, the events include the timestamps from the GPS clocks installed in each telescope trailer. Although the GPS clocks have a timing resolution of 100 ns, the times recorded for each telescope for a given event vary on the order of several μs due to the array configuration. The array timing resolution is therefore on the order of μs, which is sufficient resolution for performing timing analyses for all the known pulsars. The pulsar analysis implemented in Event Display begins by passing the event times of the gamma-ray candidate events from the signal region to TEMPO2, a pulsar timing software package [78] [28] that assigns a pulsar rotational phase between zero and one to the events based on the event times and the measured pulsar parameters. TEMPO2 determines the rotational phase of the pulsar in two steps, barycentering and phase folding.

In the barycentering step, the photon arrival times recorded at the observatory are converted to arrival times that would have been measured at the solar system barycenter (SSB), the center of mass of the solar system. This is done to remove any timing effects due to the orbit of the earth around the sun, the rotation of the earth, and other effects. The first step of the barycentering calculations involves converting the UTC times measured at the observatory to barycentric coordinate time (TCB), a convenient time standard used as the independent variable for equations describing the motions of astronomical bodies in the solar system. The next step involves calculating time of flight corrections required to convert the photon

arrival times recorded at the observatory to times that would have been recorded at the SSB. The most important calculations in this step are converting the times recorded at the observatory to times that would have been measured at the center of the earth, and converting those times to the times that would be measured at the SSB, t_{SSB}. Additional time corrections are implemented, including corrections for Einstein and Shapiro delays due to relativistic effects. The full details of the barycentering calculations are described in [78] and [28].

The second step of the TEMPO2 analysis involves assigning a rotational phase of the pulsar based on the t_{SSB} times calculated in the previous step. This is accomplished with the use of pulsar timing solutions, which consist of measurements of the pulsar frequency, f_0 and one or more frequency derivatives, $\dot{f}$, $\ddot{f}$, etc corresponding to a particular time, t_0. A brief description of phase folding for the simplified case where $\ddot{f} = 0$ is described below.

The angular frequency of the pulsar at time t is defined as:

$$\omega(t) = \frac{d\theta}{dt} = \omega_0 + \dot{\omega}t$$

therefore,

$$\theta(t) = \int_{t_0}^{t} \omega(t)\ dt = \int_{t_0}^{t} (\omega_0 + \dot{\omega}t)dt = \omega_0(t - t_0) + \frac{1}{2}\dot{\omega}(t - t_0)^2.$$

The rotational phase of the pulsar at time t is defined as:

$$\phi(t) = \theta(t)\ mod\ 2\pi$$

therefore,

$$\phi(t) = (\omega_0(t - t_0) + \frac{1}{2}\dot{\omega}(t - t_0)^2)\ mod\ 2\pi$$

$$\phi(t) = (2\pi f_0(t - t_0) + \frac{1}{2}2\pi\dot{f}(t - t_0)^2)\ mod\ 2\pi$$

$$\phi(t) = (f_0(t - t_0) + \frac{1}{2}\dot{f}(t - t_0)^2)\ mod\ 1.$$

As can be seen from the above expression for $\phi(t)$, a rotational phase for the pulsar can be calculated using the arrival times of the photons (t_{SSB}), and f_0, $\dot{f}$ and t_0 from the timing solution.

In order to visualize any periodic signal that might be present in the data, a histogram called a phaseogram of the phases of the gamma-ray candidate events can be made. Figure 5–11 shows a phaseogram made with VERITAS Crab pulsar data using the techniques described above. Two peaks can clearly be seen at phases 0 and 0.35, corresponding to the pulsar signal.

One way to quantify the significance of such a signal is to define phase intervals (or gates) prior to analyzing the data, corresponding to signal regions where pulses are expected, and a background region where no pulses are expected. This technique

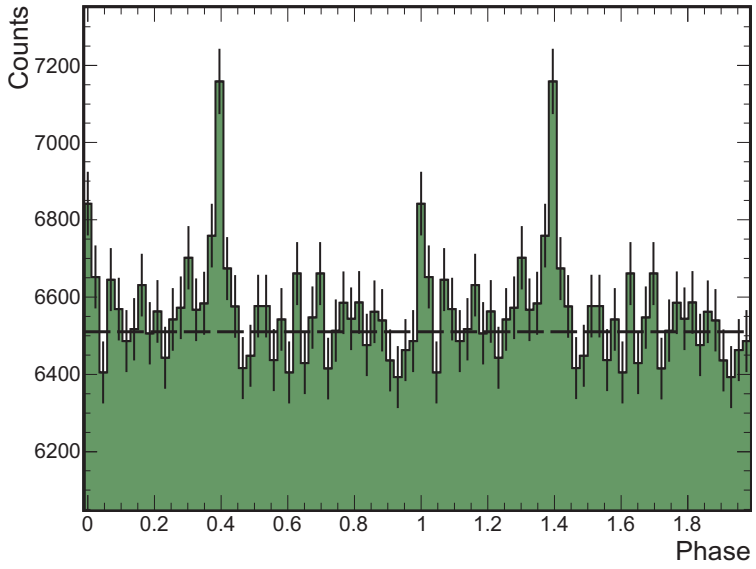

Figure 5–11: A phaseogram made with VERITAS Crab pulsar data. The pulsar signal consists of the two peaks at phases 0 and 0.35. Figure from [91]. The phase region between 1 and 2 is duplicated from the region between 0 and 1 by convention.

is used to avoid a statistical trials penalty and relies on prior knowledge of the phase profile of the pulsar. Specifically, the technique assumes that the peaks detected at lower energies (in Fermi LAT data in this work) remain at the same phases at VHE energies, as is the case for the Crab pulsar. This assumption may be incorrect for other VHE pulsars. For that reason, other periodicity tests that do not rely on prior knowledge of the phase profile are also used, such as the H-test (which is used in this work and described below). The number of counts in the signal and background phase regions, N_{On}, N_{Off} and the ratio of the sizes of the signal and background regions, α are used to calculate the significance of the signal using equation 5.1. In the same way, spectra and flux upper limits can be produced for the signal regions using the techniques described in section 5.14.

Another way to quantify the significance of a possible periodic signal is to use the H-test. The H-test is an unbinned test for periodic signals that does not rely on prior information about the shape of the phase profile of the pulsar [26]. The H-test is based on the Z_m^2 test:

$$Z_m^2 = \frac{2}{n} \sum_{k=1}^{m} \Big[\Big(\sum_{j=1}^{n} cos(2\pi k \phi_j) \Big)^2 + \Big(\sum_{j=1}^{n} sin(2\pi k \phi_j) \Big)^2 \Big]$$

where n is the number of events, and ϕ_j is the phase of event j. The H-test statistic is defined as:

$$H \; = \; \underset{1<m<20}{Max} \; (Z_m^2 - 4m + 4)$$

The probability for obtaining an H-test value above h has been determined to be: $P(H > h) = exp(-0.398h)$, which may be converted to a significance assuming a normal distribution. The H-test can also be used to calculate flux upper limits for pulsar signals, as described in [25].

CHAPTER 6
Archival pulsar analysis and results

6.1 Introduction

Archival VERITAS data was searched for pulsed emission from pulsars detected by the Fermi gamma-ray space telescope which were observed by VERITAS or present in the field of view during observations of other sources. As mentioned in section 3.2, this search was undertaken in order to attempt to expand the VHE gamma-ray pulsar catalogue, and constrain pulsar gamma-ray emission models. The details of the analyses performed for the VERITAS archival pulsar search are described in this chapter, and the results of these analyses are presented. The interpretation of the results is discussed in the next chapter.

6.2 Data selection

In order to find candidates for the VERITAS archival pulsar search, a VERITAS database tool was used that generates a list of data runs in which a given position in the sky is present in the field of view. A run list was generated for each of the positions of the sources listed in the second Fermi pulsar catalogue (2PC). This process resulted in 18 2PC sources with non-zero run lists, after excluding sources where a VERITAS pulsar analysis had been previously performed. Three additional pulsars were excluded due to the VERITAS data being taken outside the dates where the available timing solutions (described in section 6.4) were valid. This resulted in 15 pulsars from the Fermi 2PC catalogue being selected for the VERITAS archival

pulsar search. One of these pulsars is excluded here, as the analysis is currently ongoing. The remaining pulsars are listed in Table 6–1. This data was filtered further to exclude runs and portions of runs taken under poor observing conditions, using the VERITAS DQM website, described in section 5.2.

6.3 Phase gate selection

As described in section 5.15, in order to calculate the significance of potential pulsed signals in the data, signal and background phase regions (phase gates) may be defined prior to the analysis. This method relies on knowledge of the phase profile of the pulsar at lower energies, and assumes that the peaks remain at the same phase locations at VHE energies. For the VERITAS archival pulsar search, a procedure was developed whereby simulated VHE phase profiles of the archival pulsars were produced using their 2PC phase profiles in order to determine the optimal signal and background phase gates for the VERITAS analysis.

The first step of the procedure estimates the VERITAS signal and background event rates associated with an assumed VHE flux and set of event selection cuts. This is accomplished by obtaining the signal and α-scaled background event rates from a reflected region analysis of the Crab nebula using a specified set of cuts, where α is the ratio of the acceptances of the signal and the background regions (see section 5.12). For the analysis presented here, the event rates associated with a standard Crab nebula analysis using soft cuts (see section 6.4) were used, and were found to be approximately 16.1 events per minute for the signal event rate and 3.75 events per minute for the α-scaled background event rate. These rates are multiplied by a specified exposure time in order to obtain the expected number of signal counts

and α-scaled background counts for the given exposure time. For each of the archival pulsars, the total VERITAS exposure time for the pulsar was used. The number of excess counts is then computed by subtracting the number of α-scaled background counts from the number of signal counts. This excess is then scaled by a specified fraction of the Crab nebula flux corresponding to the assumed VHE source flux. For the analysis presented in this thesis, the assumed VHE source flux was set to 1% of the Crab nebula flux for all of the pulsars. This assumption was motivated by the fact that the differential flux of the Crab pulsar was measured to be approximately equal to 1% of the differential flux of the Crab nebula at 200 GeV [33][38]. The choice of assumed VHE source flux was found to not affect the phase gate locations significantly.

The scaled excess is then distributed according to the phase profile of the pulsar published in the second Fermi pulsar catalogue (2PC). This is accomplished by first subtracting the background of the Fermi phaseogram by subtracting the value of the bin with the lowest value from all of the bins of the phaseogram. The background-subtracted Fermi phaseogram is then normalized, so that the bin contents add up to one. Each bin of the background-subtracted normalized phaseogram is then multiplied by the scaled excess. The expected number of background counts for the VHE analysis is then added to each bin by adding the number of α-scaled background counts divided by the number of bins in the phaseogram to each bin of the phaseogram.

The number of signal gates for each pulsar is chosen based on a visual inspection of the 2PC phaseogram. All non-overlapping phase gate bin combinations are tested,

with optional constraints on minimum and maximum phases and minimum and maximum gate widths for each phase gate. For each combination of gates, the number of events in the signal and background regions are used to calculate a significance using equation 5.1. The combination of gates that results in the highest significance is used for the pulsar analysis in most cases. For cases where two signal phase gates are initially defined but were found to be contiguous, the number of signal gates is reduced to one, and the procedure is performed again.

For some cases where the phase profile showed two clear non overlapping peaks, the maximum significance obtained using the above procedure resulted in only one signal phase gate being defined. In order to define signal phase gates for each peak in these circumstances, a three-pass procedure was developed. The first pass simply consists of the method described above. The second pass defines only one signal phase gate, and excludes the signal gate defined in the first pass from the signal gate search region. This ensures that a signal phase gate is defined for the peak not found in the first pass. The third pass defines two signal phase gates but constrains one of the signal gates to be the one defined in the second pass. The three-pass procedure was used to define the phase gates for PSRJ0205+6449 and PSRJ2021+4026.

In order to save computing time when analyzing the 100 bin Fermi phaseograms, the maximum signal gate widths were constrained to be marginally larger than the full width of the largest visually identified peak in the phaseogram. Likewise, the maximum background gate widths were constrained to be marginally larger than the largest visually-identified background region. The gate widths determined for these cases were all found to be less wide than the constraints.

Source	Time (min)	P1	P2	Background
J0007+7303	2125	0.05 - 0.36	None	0.41 - 0.01
J0205+6449	2043	0.04 - 0.11	0.51 - 0.59	0.60 - 0.04
J0218+4232	1706	0.42 - 0.78	None	0.82 - 0.22
J0248+6021	4035	0.28 - 0.50	None	0.54 - 0.24
J0357+3205	563	0.02 - 0.24	None	0.33 - 0.96
J0631+1036	832	0.36 - 0.54	None	0.64 - 0.24
J0633+0632	7663	0.56 - 0.60	0.09 - 0.16	0.63 - 0.06
J1907+0602	3577	0.52 - 0.62	0.19 - 0.27	0.64 - 0.15
J1954+2836	457	0.52 - 0.58	0.08 - 0.16	0.64 - 0.02
J1958+2846	1544	0.46 - 0.58	0.10 - 0.12	0.62 - 0.08
J2021+3651	5393	0.58 - 0.62	0.11 - 0.15	0.66 - 0.07
J2021+4026	2069	0.00 - 0.16	0.50 - 0.66	0.20 - 0.48
J2032+4127	3842	0.60 - 0.62	0.09 - 0.13	0.64 - 0.04
J2229+6114	3884	0.38 - 0.53	None	0.59 - 0.15

Table 6–1: A summary of the results obtained from the method described in the text. From left to right: source name, VERITAS exposure time in minutes, signal gates (designated P1 and P2) and background gates for the simulated phaseograms.

The results of these procedures are summarized in Table 6–1 and shown in Figure 6–1.

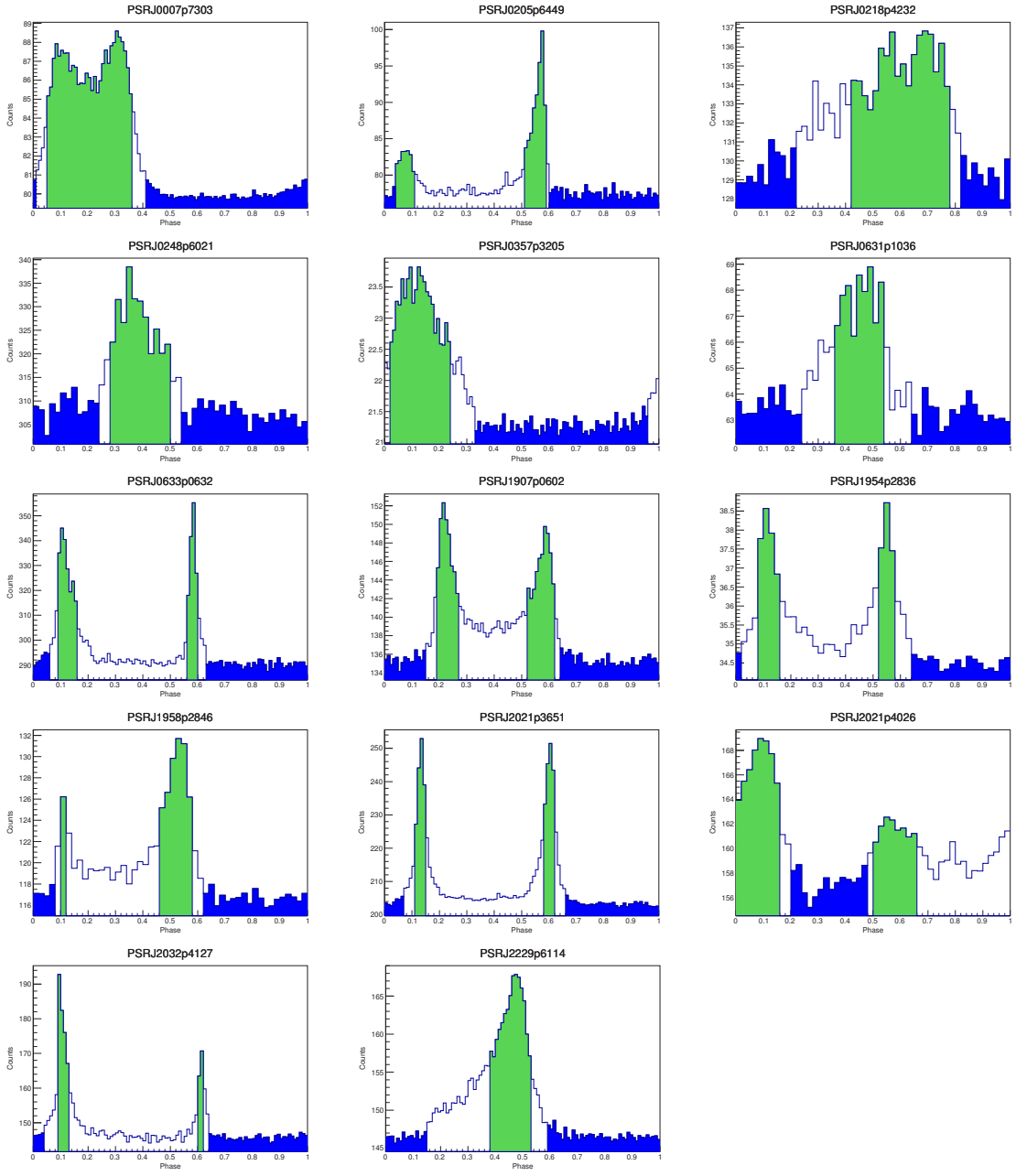

Figure 6–1: Simulated phaseograms of the VERITAS archival pulsars with phase gates defined by the method described in the text. The signal gates are shown in green and background gates are shown in blue.

Cuts	*2ndSizeMax* (V4,V5)	*2ndSizeMax* (V6)	Height	E thresh
Soft	200 DC	200 DC	> 6 km	150-170 GeV
Moderate	400 DC	600 DC	> 6 km	250-270 GeV
Hard	1000 DC	1400 DC	> 0 km	450-550 GeV

Table 6–2: Sets of cuts used for the VERITAS archival pulsar searches. See text for details.

6.4 Data analysis and results

The data for the VERITAS archival pulsar search was processed with the *Event Display* v4.80 analysis package using the techniques described in the previous chapter. The data was obtained from the VERITAS data repository at UCLA and processed at McGill University. Three sets of event selection cuts called soft, moderate and hard with energy thresholds increasing from soft to hard were used in order to maximize the sensitivity for different spectral emission scenarios. Standard *Event Display* cuts were used in order to take advantage of available instrument response functions. Each of these sets of cuts uses an *mscw* range of -1.2 to 0.5, an *mscl* range of -1.2 to 0.7 (see Figure 5–7), and a shower core distance of less than 350m from the center of the V4 array. These sets differ mostly in the cut on the value of the *Size* of the second-brightest shower image recorded by the array, *2ndSizeMax*. A summary of the differences between these sets is shown in Table 6–2. For moderate and hard cuts, the *2ndSizeMax* values are different for the V6 epoch due to the increased light sensitivity of the VERITAS cameras following the PMT upgrade described in section 4.5.3. The cut on emission height is a good method for selecting gamma-ray candidate events at low energies, but is not needed for the hard cuts. The energy

thresholds reported in the table are defined as the peak in the differential counting rate for a Crab-nebula-like spectrum.

The locations of the pulsars as reported in the timing solutions used to phase fold the data (see below) were used as the source locations for the VERITAS analyses. Circular signal regions centered on the source locations with Θ^2 values of 0.008°^2} (see section 5.12) were used in order to select gamma-ray candidate events for the analyses. The selected gamma-ray candidate events were then barycentered and phase folded with TEMPO2, as described in section 5.15. The 2PC timing solutions [21] of the selected pulsars were not valid for many of the dates when VERITAS data was taken on them. Timing solutions from the LAT Gamma-ray Pulsar Timing Models web page [20] were found to be valid for more of the dates when VERITAS data was taken, and were used instead if possible. For the pulsars where the timing solutions from [20] were used, the different phase definitions between the two timing solutions required the phase offsets between them to be determined in order to use the gates presented in Table 6–1 with the phase-folded data. These phase-offsets were calculated using cross correlation analyses of phaseograms produced with Fermi LAT data using both timing solutions, and are presented in Table 6–3. A phase offset of 0.0 indicates that the 2PC timing solution was used to fold the VERITAS data for that pulsar. For the significance calculations, the phase offsets were added to the gamma-ray candidate event phases in order to use the gates defined in Table 6–1. For the flux upper-limit analyses described below, due to the manner in which the Event Display analysis package calculates flux upper limits, the phases of the gamma-ray candidate events were left un-modified, and the phase offsets were subtracted from

Source	Phase offset	P1	P2	Background
J0007+7303	0.9275	0.1225 - 0.4325	None	0.4825 - 0.0825
J0205+6449	0.8545	0.1855 - 0.2555	0.6555 - 0.7355	0.7455 - 0.1855
J0218+4232	0.0	0.42 - 0.78	None	0.82 - 0.22
J0248+6021	0.033	0.247 - 0.467	None	0.507 - 0.207
J0357+3205	0.003	0.017 - 0.237	None	0.327 - 0.957
J0631+1036	0.023	0.337 - 0.517	None	0.617 - 0.217
J0633+0632	0.0145	0.5455 - 0.5855	0.0755 - 0.1455	0.6155 - 0.0455
J1907+0602	0.002	0.518 - 0.618	0.188 - 0.268	0.638 - 0.148
J1954+2836	0.0125	0.5075 - 0.5675	0.0675 - 0.1475	0.6275 - 0.0075
J1958+2846	0.0135	0.4465 - 0.5665	0.0865 - 0.1065	0.6065 - 0.0665
J2021+3651	0.0355	0.5445 - 0.5845	0.0745 - 0.1145	0.6245 - 0.0345
J2021+4026	0.9505	0.0495 - 0.2095	0.5495 - 0.7095	0.2495 - 0.5295
J2032+4127	0.1585	0.4415 - 0.4615	0.9315 - 0.9715	0.4815 - 0.8815
J2229+6114	0.9365	0.4435 - 0.5935	None	0.6535 - 0.2135

Table 6–3: Phase offsets between the 2PC timing solutions [21] and timing solutions obtained from the LAT Gamma-ray Pulsar Timing Models web page [20] that were used to fold most of the VERITAS data. A phase offset of 0.0 indicates that the 2PC timing solution was used to fold the VERITAS data for that pulsar. For the significance calculations, the phase offsets were added to the gamma-ray candidate event phases in order to use the gates defined in Table 6–1. For the flux upper-limit analyses, due to the manner in which the Event Display analysis package calculates flux upper limits, the phases of the gamma-ray candidate events were left un-modified, and the phase offsets were subtracted from the gates instead. The numbers of signal and background events between the significance and upper limits calculations were found to be identical for each source and set of cuts, as expected. The corrected phase gates used for the flux upper-limit analyses calculated by subtracting the phase offsets from the gate phases presented in Table 6–1 are also shown.

the gates instead. The numbers of signal and background events between the significance and upper limits calculations were found to be identical for each source and set of cuts, as expected. The significance of potential pulsed signals was calculated from the number of events found in the signal regions(s), the number of events found in the background region, and the ratio of the size of the signal region(s) to the background region, α using equation 5.1 for each source for each set of cuts. Significances were also calculated using the calculated H-test statistics, as described in section 5.15 for each source and set of cuts. No pulsed emission was detected with a significance of greater than 3 σ for any of the analyses. Energy thresholds for each observing run were obtained for each set of cuts by determining the energy at which the energy reconstruction bias of the phase-folded events dropped below ten percent. The energy threshold for a given source and set of cuts was determined by calculating the time weighted average of the energy thresholds determined for each run. Runs where no events passed selection cuts were not assigned energy thresholds and were eliminated from this calculation. For each set of cuts, integral flux upper limits were calculated at the 95% confidence level above these energy thresholds assuming a power-law spectrum with a spectral index of 3.8 (the same as for the Crab pulsar measured by [38]), using the method of Rolke [106] for the gated analyses, and with the method described in [25] using H-test values calculated for events above the energy thresholds and an assumed pulse duty cycle of 0.1 (see [25] for details). Phaseograms for each source and set of cuts are shown in Figures 6–2 to 6–15, and tables 6–4 to 6–6 summarize the results of these analyses.

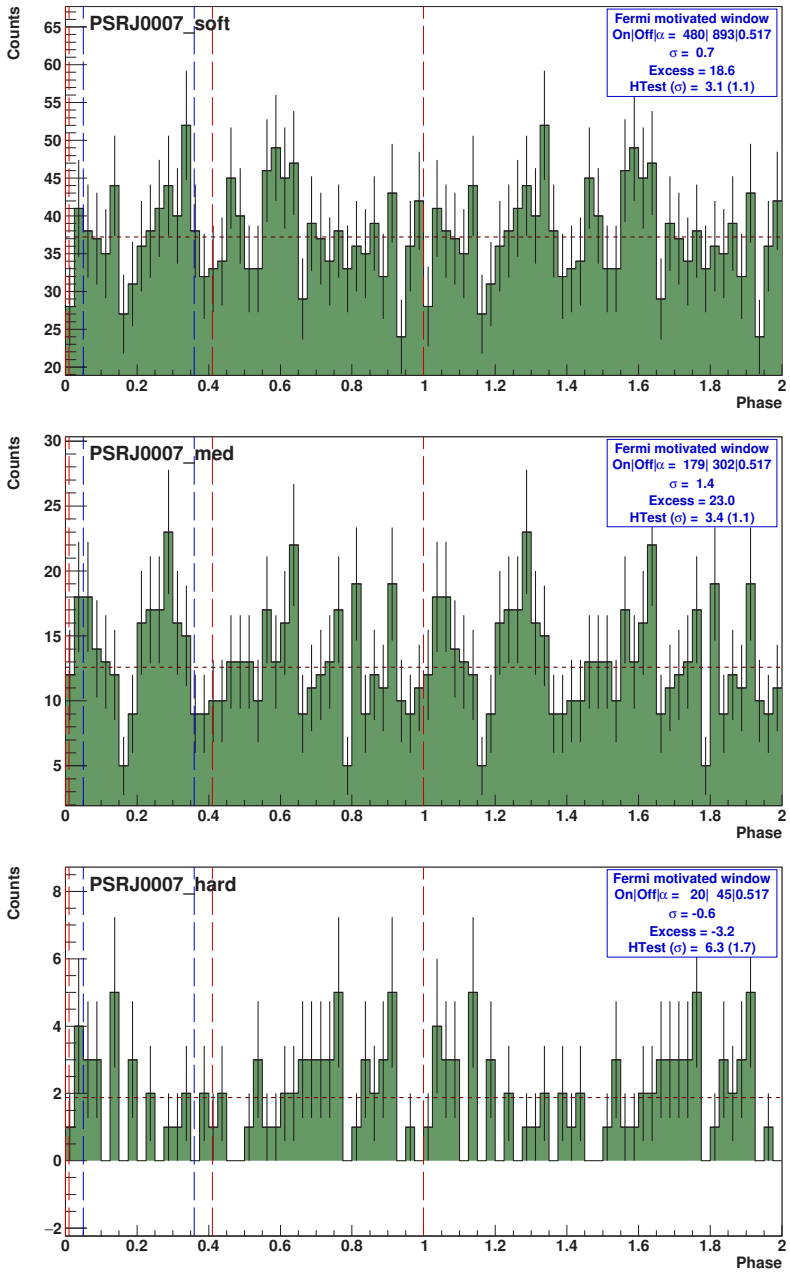

Figure 6–2: Phase profiles for PSRJ0007+7303. Soft cuts (top), moderate cuts (middle), hard cuts (bottom). The blue dashed lines indicate the location(s) of the signal regions(s), the red dashed lines indicate the location of the background region and the black dashed lines indicate the average number of counts per bin. The text box summarizes the information presented in Tables 6–4, 6–5 and 6–6 as well as the H-test values and excess counts.

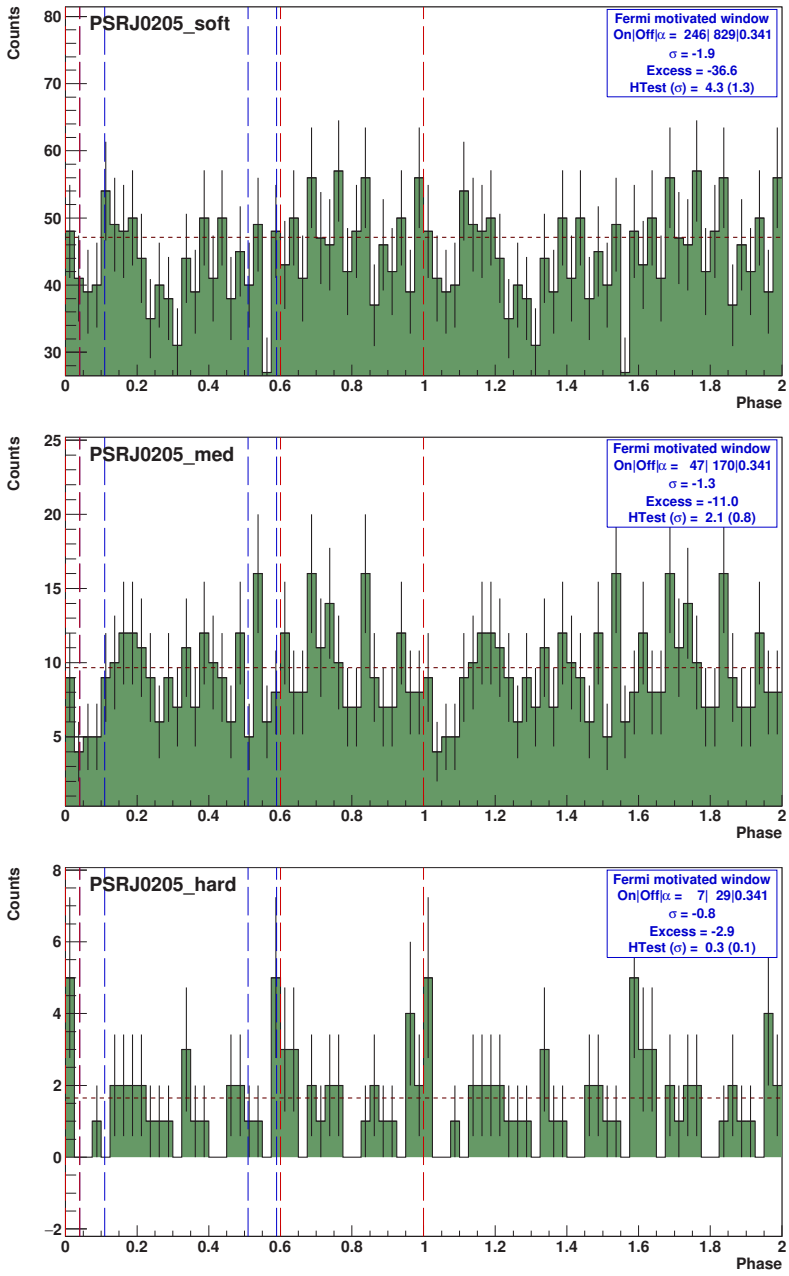

Figure 6–3: Phase profiles for PSRJ0205+6449. See Figure 6–2 caption for details.

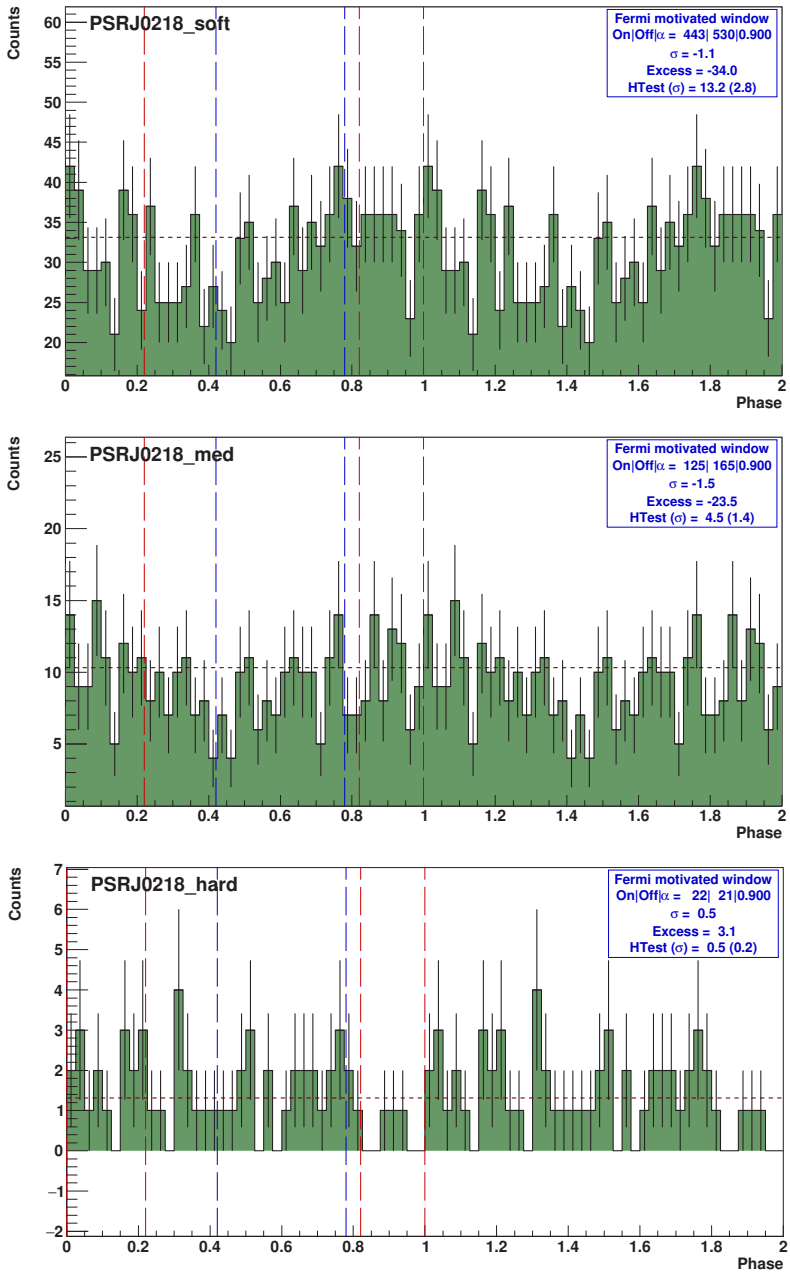

Figure 6–4: Phase profiles for PSRJ0218+4232. See Figure 6–2 caption for details.

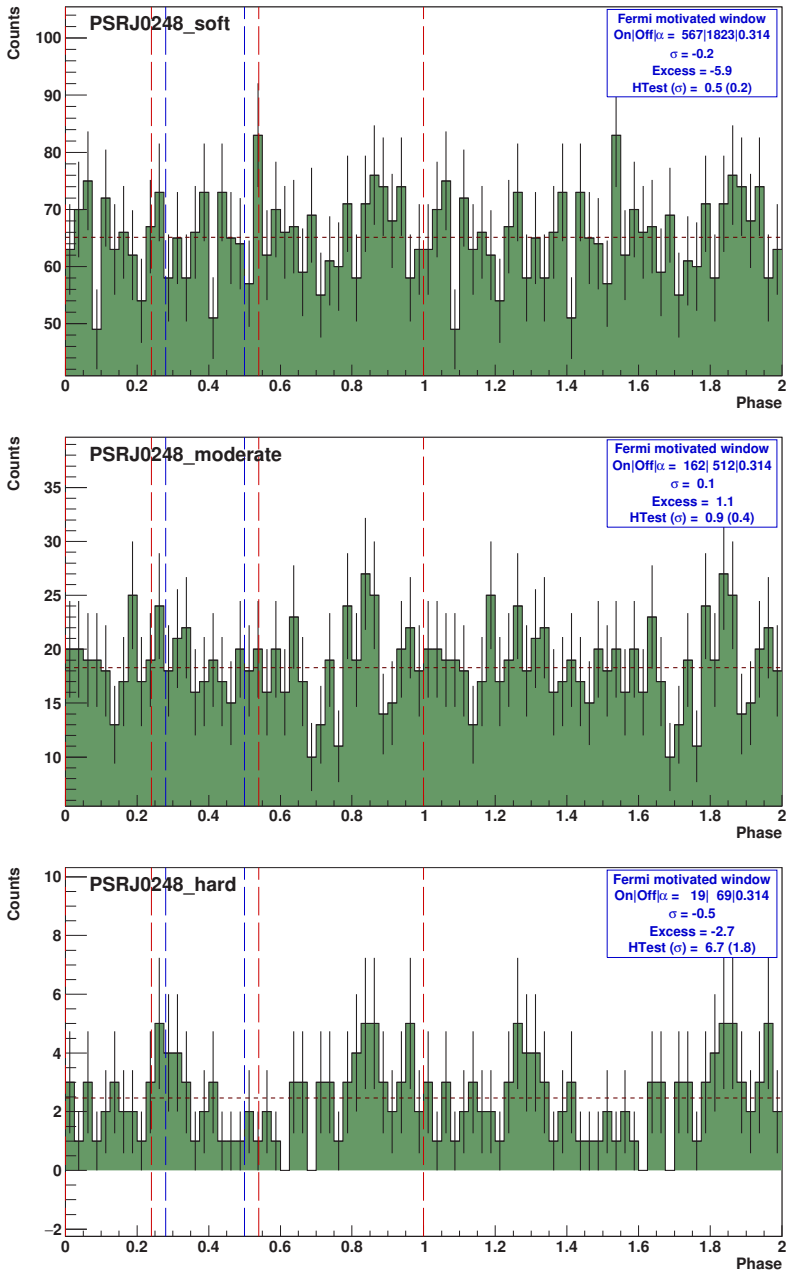

Figure 6–5: Phase profiles for PSRJ0248+6021. See Figure 6–2 caption for details.

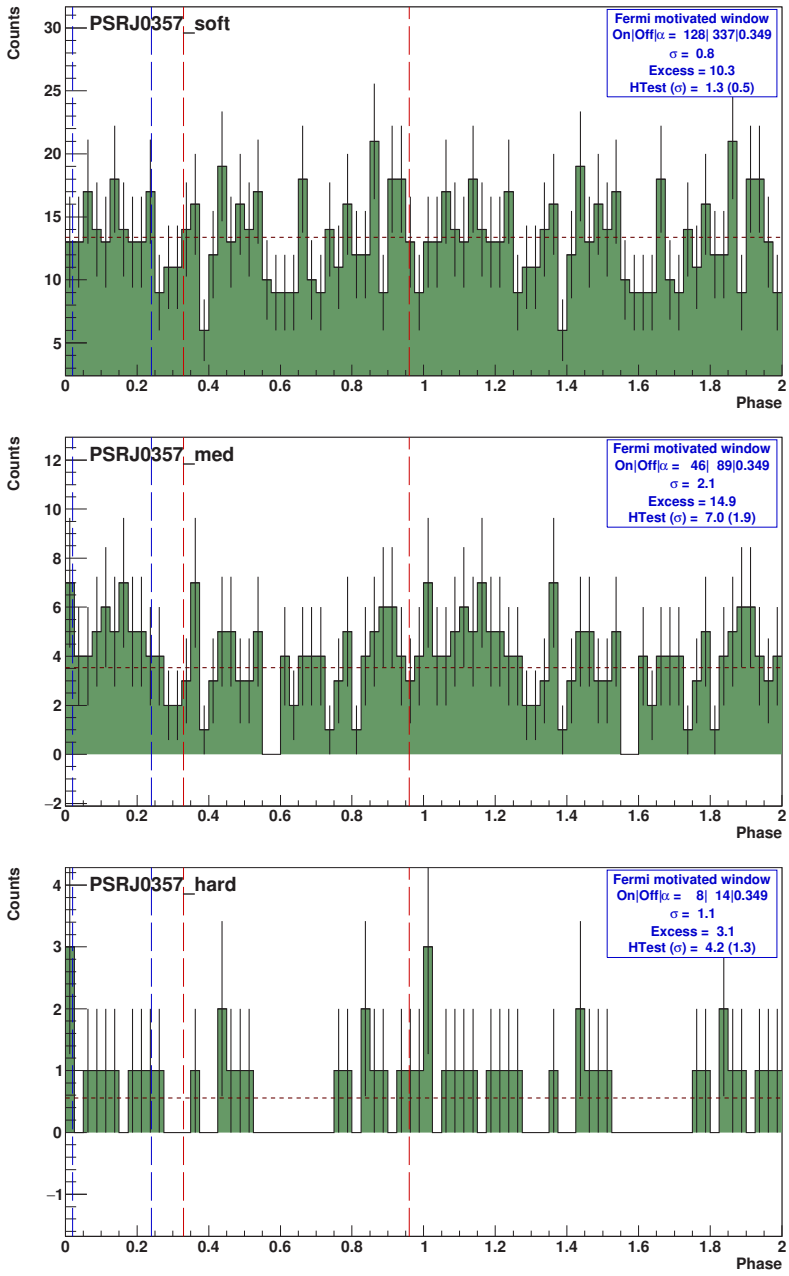

Figure 6–6: Phase profiles for PSRJ0357+3205. See Figure 6–2 caption for details.

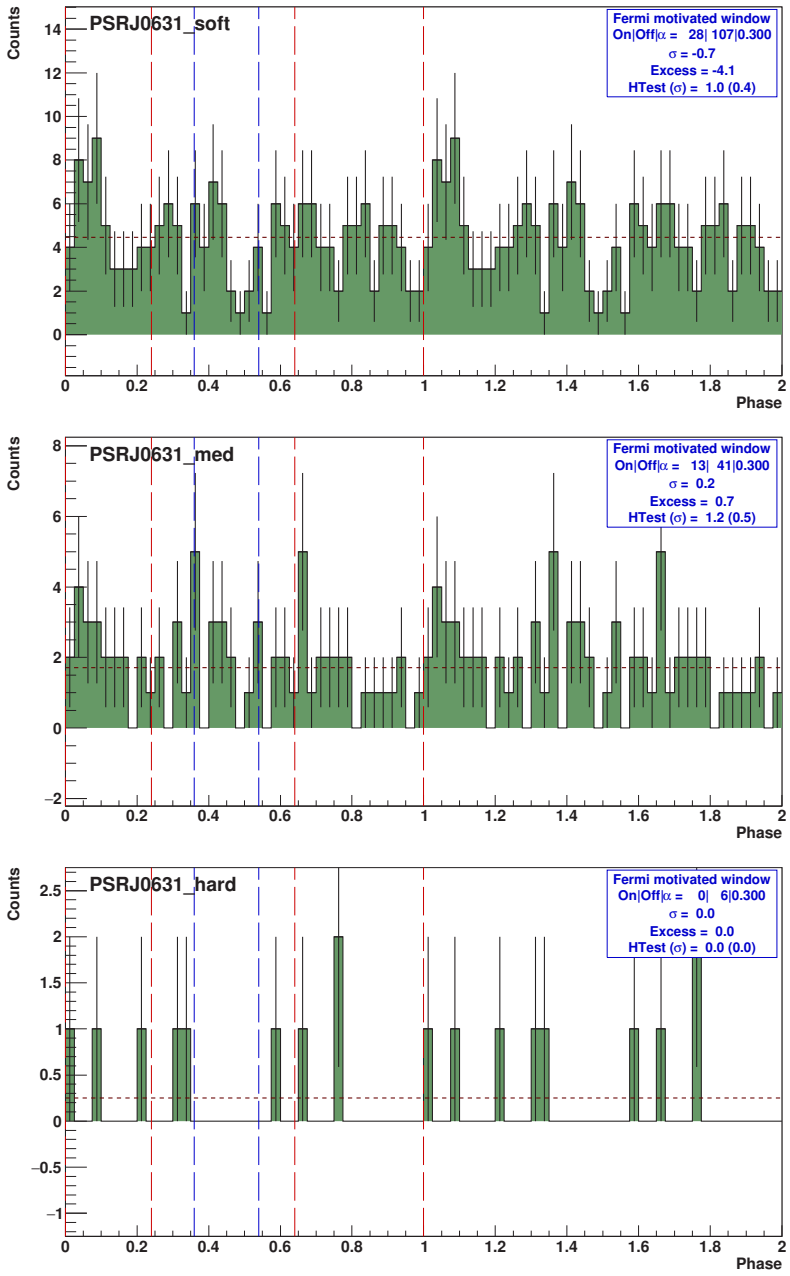

Figure 6–7: Phase profiles for PSRJ0631+1036. See Figure 6–2 caption for details.

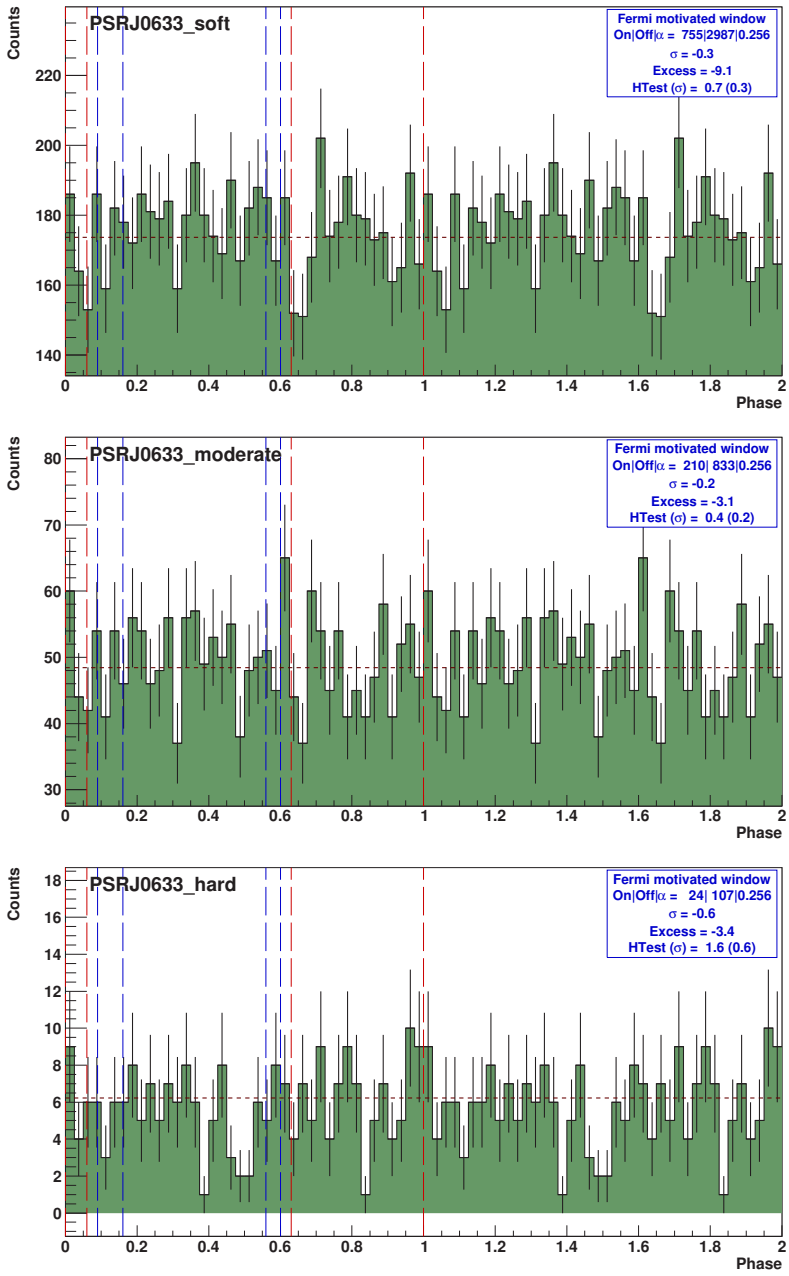

Figure 6–8: Phase profiles for PSRJ0633+0632. See Figure 6–2 caption for details.

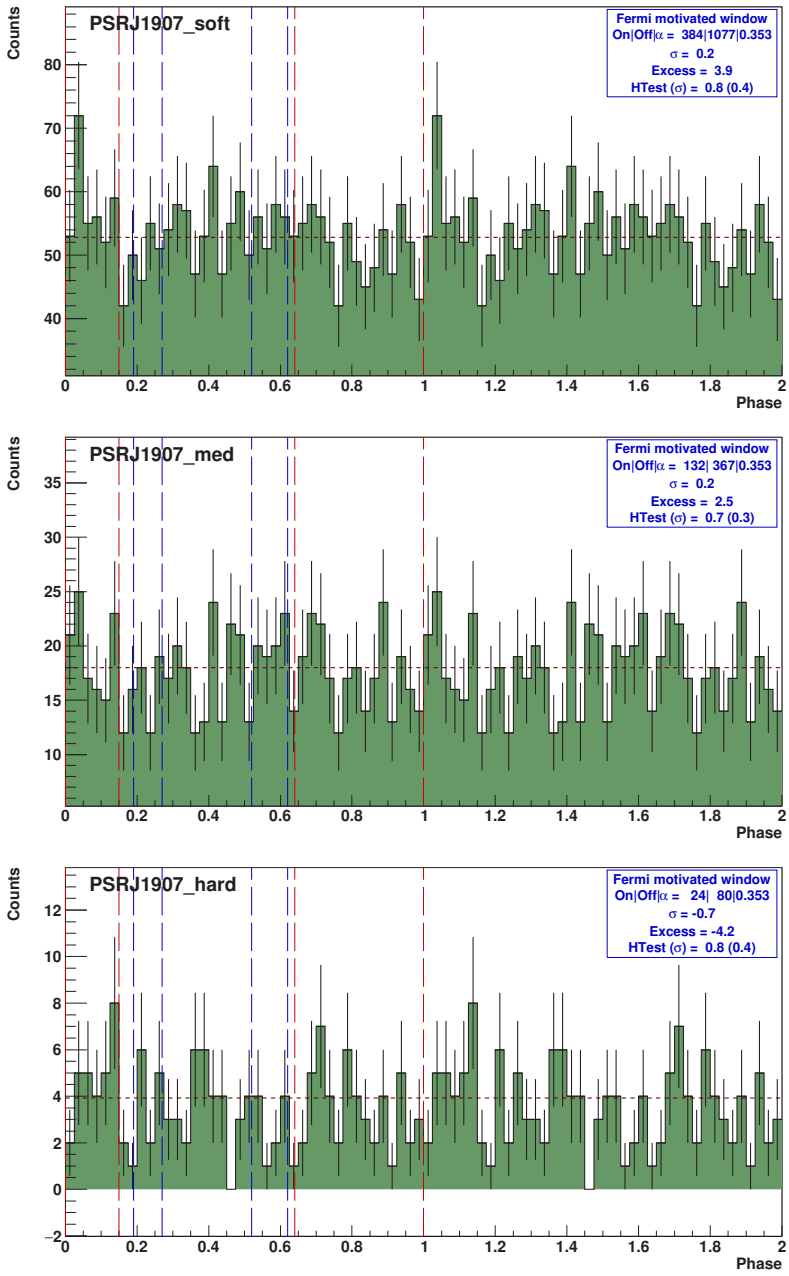

Figure 6–9: Phase profiles for PSRJ1907+0602. See Figure 6–2 caption for details.

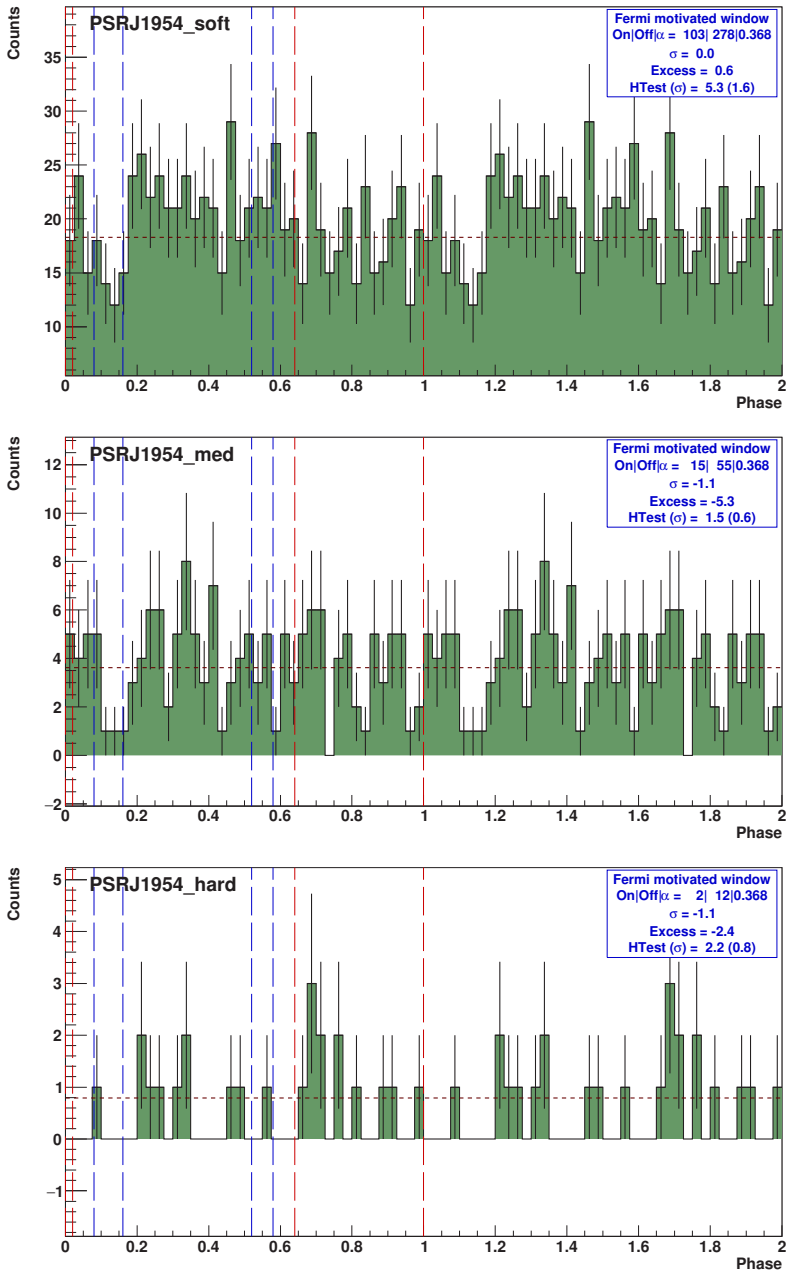

Figure 6–10: Phase profiles for PSRJ1954+2836. See Figure 6–2 caption for details.

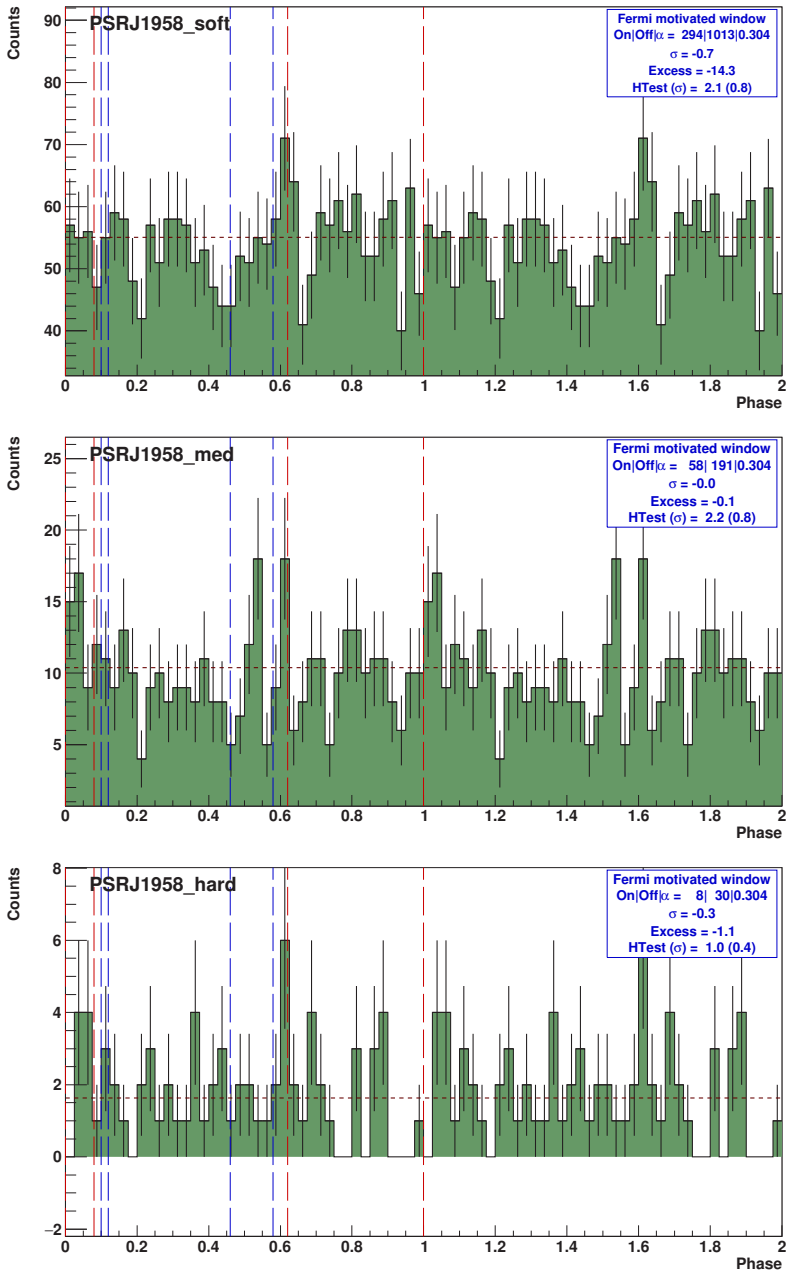

Figure 6–11: Phase profiles for PSRJ1958+2846. See Figure 6–2 caption for details.

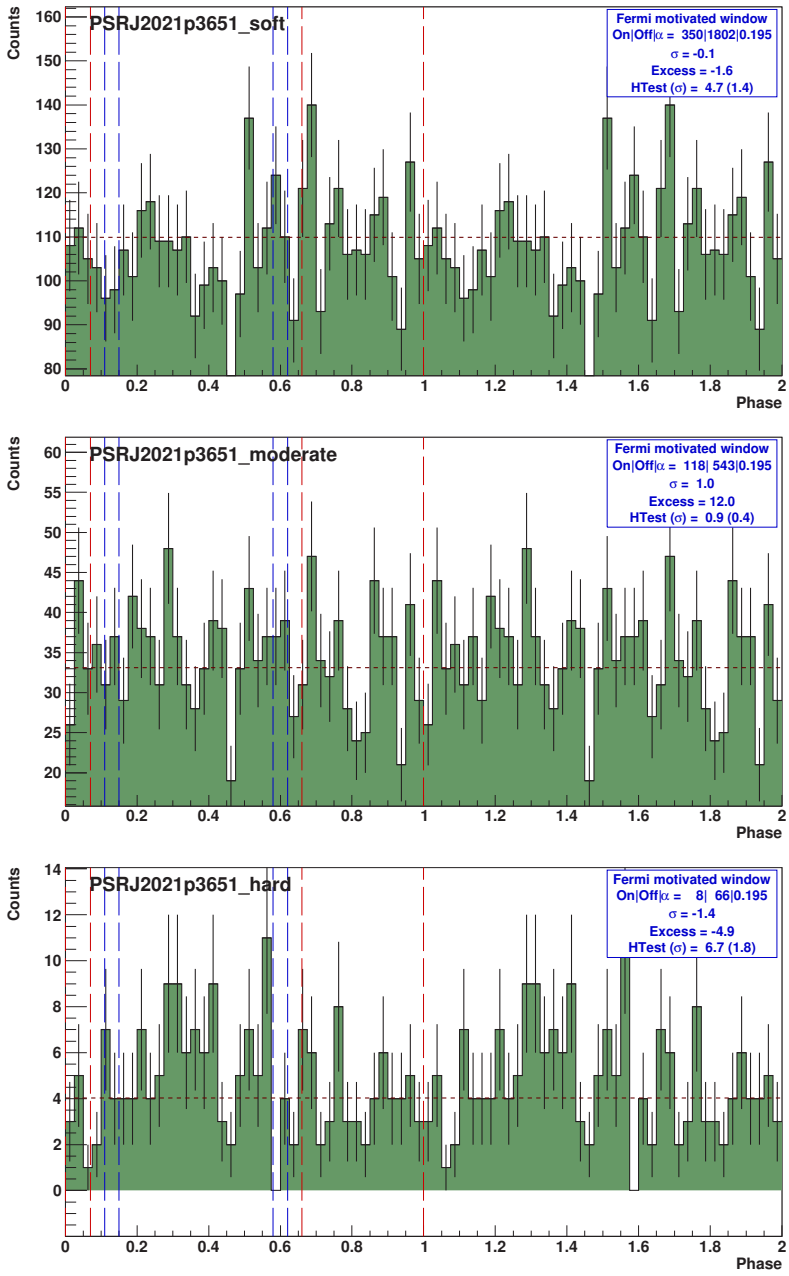

Figure 6–12: Phase profiles for PSRJ2021+3651. See Figure 6–2 caption for details.

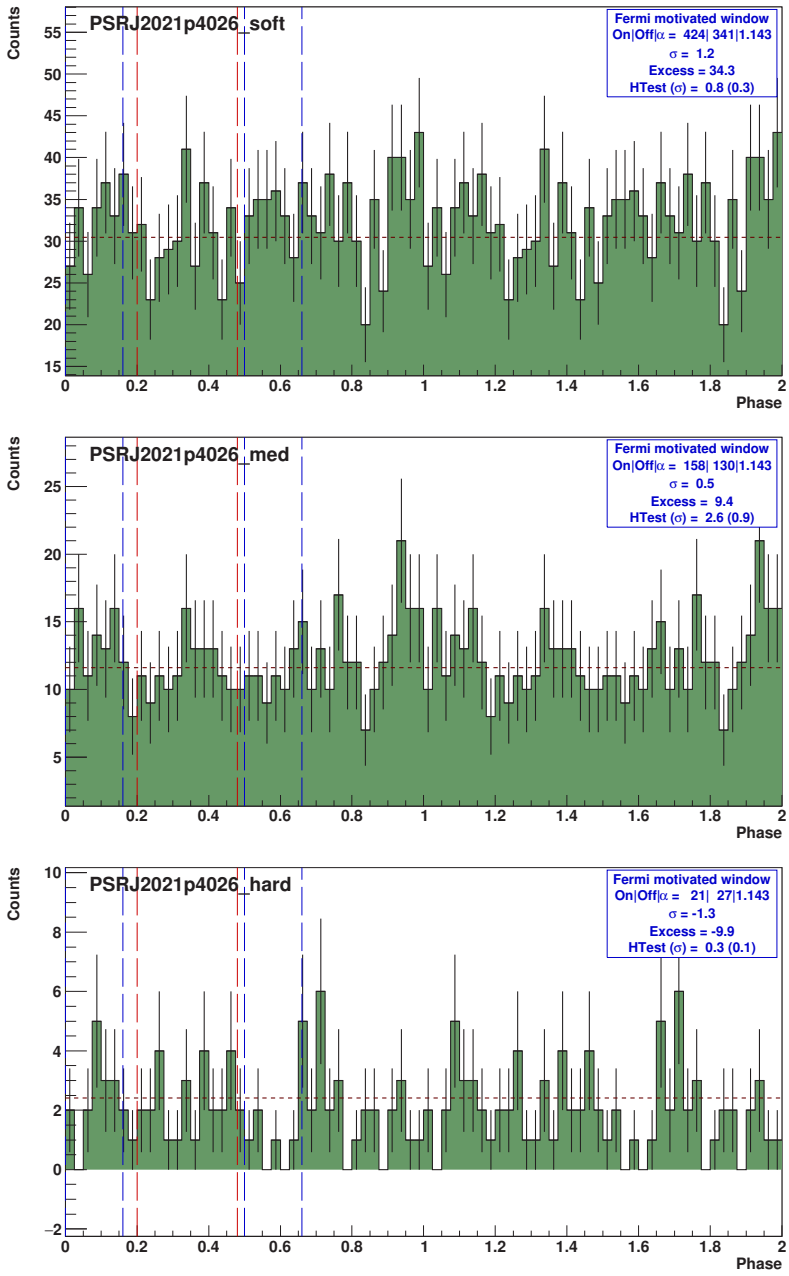

Figure 6–13: Phase profiles for PSRJ2021+4026. See Figure 6–2 caption for details.

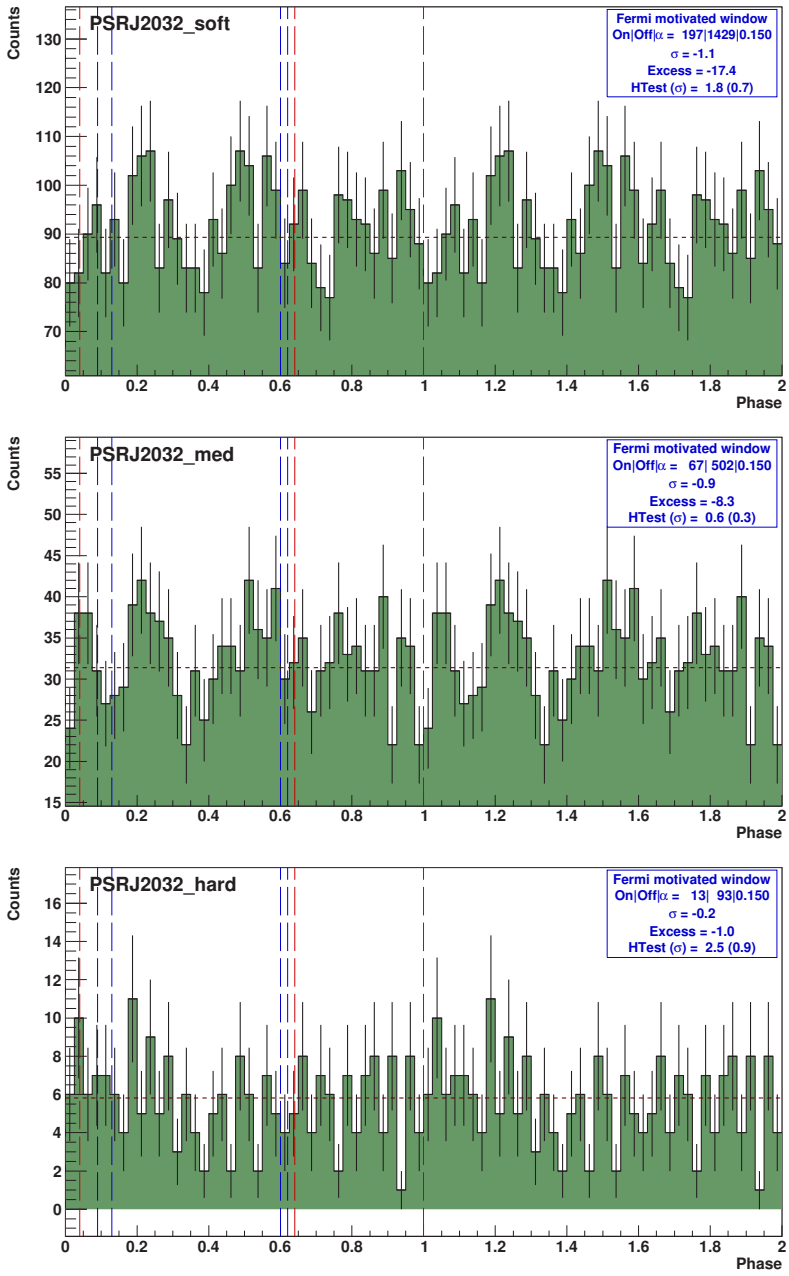

Figure 6–14: Phase profiles for PSRJ2032+4127. See Figure 6–2 caption for details.

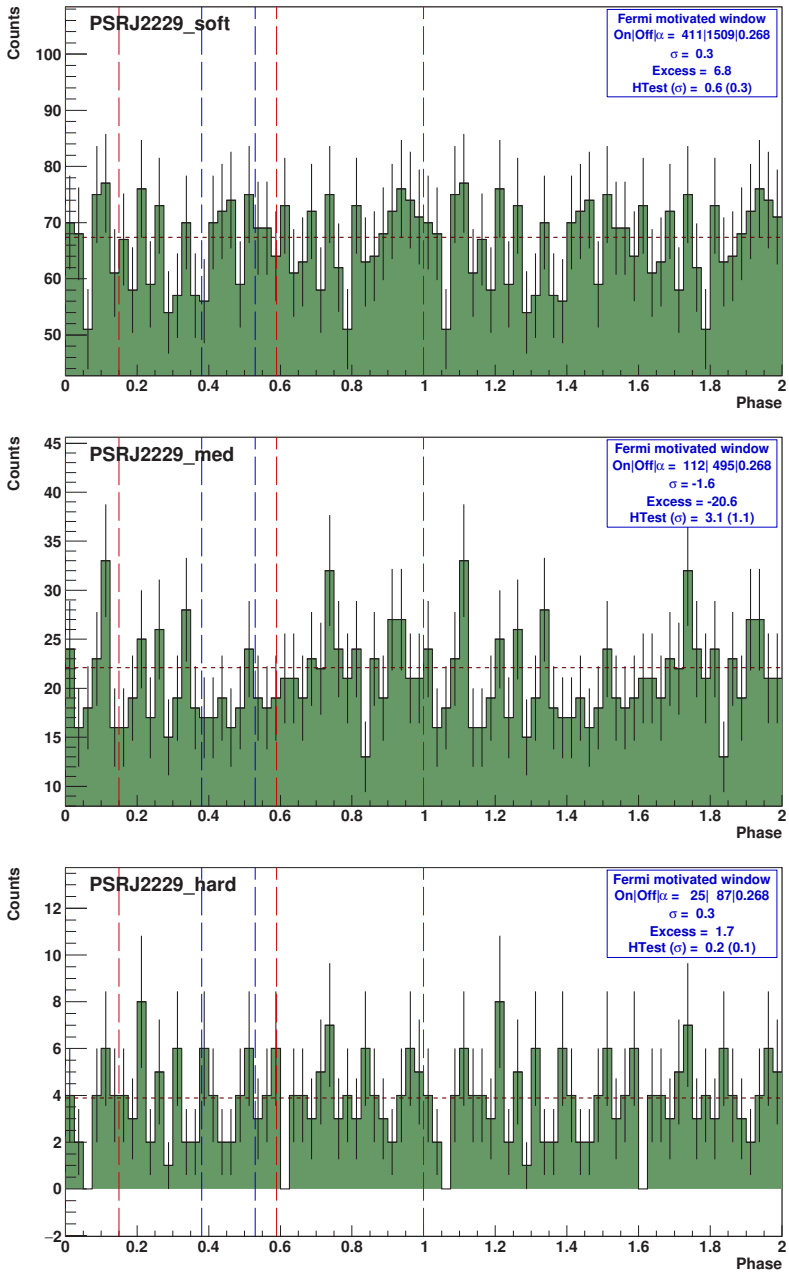

Figure 6–15: Phase profiles for PSRJ2229+6114. See Figure 6–2 caption for details.

Source	On	Off	α	Sig σ	H-test σ	E_{th} TeV	Rolke UL $m^{-2}s^{-1}$	H-test UL $m^{-2}s^{-1}$
J0007+7303	480	893	0.517	0.7	1.1	0.521	6.41×10^{-09}	2.96×10^{-09}
J0205+6449	246	829	0.341	-1.9	1.3	0.328	1.21×10^{-09}	8.63×10^{-09}
J0218+4232	443	530	0.900	-1.1	2.8	0.204	7.27×10^{-09}	2.03×10^{-08}
J0248+6021	567	1823	0.314	-0.2	0.2	0.302	9.03×10^{-09}	7.64×10^{-09}
J0357+3205	128	337	0.349	0.8	0.5	0.181	2.65×10^{-08}	3.40×10^{-08}
J0631+1036	28	107	0.300	-0.7	0.4	0.253	8.96×10^{-09}	2.23×10^{-08}
J0633+0632	755	2987	0.256	-0.3	0.3	0.239	2.19×10^{-09}	3.95×10^{-09}
J1907+0602	384	1077	0.353	0.2	0.4	0.229	2.01×10^{-09}	6.61×10^{-09}
J1954+2836	103	278	0.368	0.0	1.6	0.165	3.08×10^{-08}	4.58×10^{-08}
J1958+2846	294	1013	0.304	-0.7	0.8	0.149	1.75×10^{-08}	2.81×10^{-08}
J2021+3651	350	1802	0.195	-0.1	1.4	0.214	2.57×10^{-09}	5.22×10^{-09}
J2021+4026	424	341	1.143	1.2	0.3	0.230	2.66×10^{-08}	1.78×10^{-08}
J2032+4127	197	1429	0.150	-1.1	0.7	0.262	2.77×10^{-09}	5.31×10^{-09}
J2229+6114	411	1509	0.268	0.3	0.3	0.340	8.92×10^{-11}	9.76×10^{-09}

Table 6–4: Soft cuts results. From left to right: source name, number of signal counts obtained from the signal phase region(s), number of background counts obtained from the background phase region, the size of the signal region(s) relative to the size of the background region, significance in σ calculated using equation 5.1, H-test significance, the energy threshold in TeV above which the integral flux upper limits are calculated, integral flux upper limits in $m^{-2}s^{-1}$ determined using the Rolke method [106], and integral flux upper limits in $m^{-2}s^{-1}$ obtained using the H-test [25].

Source	On	Off	α	Sig σ	H-test σ	E_{th} TeV	Rolke UL $m^{-2}s^{-1}$	H-test UL $m^{-2}s^{-1}$
J0007+7303	179	302	0.517	1.4	1.1	0.578	5.65×10^{-09}	2.43×10^{-09}
J0205+6449	47	170	0.341	-1.3	0.8	0.398	1.30×10^{-09}	5.28×10^{-09}
J0218+4232	125	165	0.900	-1.5	1.4	0.248	3.75×10^{-09}	1.37×10^{-08}
J0248+6021	162	512	0.314	0.1	0.4	0.358	3.96×10^{-09}	7.72×10^{-09}
J0357+3205	46	89	0.349	2.1	1.9	0.217	2.06×10^{-08}	1.74×10^{-08}
J0631+1036	13	41	0.300	0.2	0.5	0.276	8.67×10^{-09}	1.73×10^{-08}
J0633+0632	210	833	0.256	-0.2	0.2	0.276	6.67×10^{-10}	3.02×10^{-09}
J1907+0602	132	367	0.353	0.2	0.3	0.268	3.23×10^{-09}	4.58×10^{-09}
J1954+2836	15	55	0.368	-1.1	0.6	0.214	1.68×10^{-09}	2.00×10^{-08}
J1958+2846	58	191	0.304	0.0	0.8	0.195	8.04×10^{-09}	1.46×10^{-08}
J2021+3651	118	543	0.195	1.0	0.4	0.242	3.98×10^{-09}	8.88×10^{-09}
J2021+4026	158	130	1.143	0.5	0.9	0.274	7.65×10^{-09}	7.81×10^{-09}
J2032+4127	67	502	0.150	-0.9	0.3	0.299	1.09×10^{-09}	2.27×10^{-09}
J2229+6114	112	495	0.268	-1.6	1.1	0.404	4.66×10^{-10}	3.83×10^{-09}

Table 6–5: Same as table 6–4 but for moderate cuts results.

Source	On	Off	α	Sig σ	H-test σ	E_{th} TeV	Rolke UL $m^{-2}s^{-1}$	H-test UL $m^{-2}s^{-1}$
J0007+7303	20	45	0.517	-0.6	1.7	1.03	8.03×10^{-10}	1.93×10^{-09}
J0205+6449	7	29	0.341	-0.8	0.1	0.687	6.34×10^{-10}	1.91×10^{-09}
J0218+4232	22	21	0.900	0.5	0.2	0.474	3.25×10^{-09}	2.59×10^{-09}
J0248+6021	19	69	0.314	-0.5	1.8	0.630	1.77×10^{-09}	2.69×10^{-09}
J0357+3205	8	14	0.349	1.1	1.3	0.400	4.56×10^{-09}	4.86×10^{-09}
J0631+1036	0	6	0.300	0.0	0.0	0.507	2.82×10^{-09}	2.77×10^{-09}
J0633+0632	24	107	0.256	-0.6	0.6	0.504	4.50×10^{-10}	7.68×10^{-10}
J1907+0602	24	80	0.353	-0.7	0.4	0.517	9.07×10^{-10}	8.98×10^{-10}
J1954+2836	2	12	0.368	-1.1	0.8	0.371	2.99×10^{-09}	8.61×10^{-09}
J1958+2846	8	30	0.304	-0.3	0.4	0.346	3.63×10^{-09}	5.06×10^{-09}
J2021+3651	8	66	0.195	-1.4	1.8	0.445	2.71×10^{-10}	2.66×10^{-09}
J2021+4026	21	27	1.143	-1.3	0.1	0.506	2.72×10^{-10}	2.19×10^{-09}
J2032+4127	13	93	0.150	-0.2	0.9	0.495	4.30×10^{-10}	2.24×10^{-09}
J2229+6114	25	87	0.268	0.3	0.1	0.728	1.58×10^{-09}	1.91×10^{-09}

Table 6–6: Same as table 6–4 but for hard cuts results.

In order to contextualize the calculated upper limits, Fermi LAT spectra were produced for each of the archival pulsars, using 7.6 years of LAT data. The Fermi LAT Science Tools (version v10r0p5) were used with the standard quality cuts described in [52]. Source class events with energies between 100 MeV and 300 GeV were collected within a region of interest (ROI) of 20 degrees from the location of the pulsar as reported in the third Fermi LAT source catalogue [32]. These events were processed with the maximum likelihood fitting technique using the Pass 8 instrument response functions. The spectral reconstruction follows the same methods as those described in the 2PC catalogue. A maximum likelihood analysis was performed in 12 logarithmically spaced energy bins, spanning energies from 100 MeV to 300 GeV. The spectra of the 3FGL sources in the ROI as well as the galactic and isotropic diffuse backgrounds (gll_iem_v06.fits and iso_p8r2_source_V6_v06.txt) were included in the likelihood fit. The normalization parameters of the galactic and isotropic diffuse backgrounds, and the spectral parameters of the 3FGL sources within 4 degrees of the source location were left free, while the other sources had their parameters fixed to their 3FGL values. In each bin of the spectrum, the pulsar was modelled as a point source with a power law spectrum, with the flux normalization and spectral index left as free parameters in the fit.

The VERITAS integral flux upper limits presented in Tables 6–4, 6–5 and 6–6 were used to calculate differential flux upper limits at the energy thresholds, assuming a power law spectrum with a spectral index of 3.8. Figures 6–16 to 6–19 show the Fermi LAT spectra of the archival pulsars with the VERITAS differential flux upper limits multiplied by E^2, plotted at the energy thresholds calculated using

the two methods described earlier for each set of cuts. The Fermi LAT spectral points are shown in black. The VERITAS flux upper limits for the gated analyses calculated using the method of Rolke are represented by the blue vertical arrows and the VERITAS flux upper limits determined from the H-test statistics using the method described in [25] are represented by the red vertical arrows. The slope of the diagonal arrows above the VERITAS upper limit arrows represents the assumed spectral index of 3.8. The black lines represent the spectral shape of the Crab nebula as measured by [33], scaled to 1%, and the grey bow ties represent the spectrum of the Crab pulsar as measured by [38]. The interpretation of these results is discussed in the next chapter.

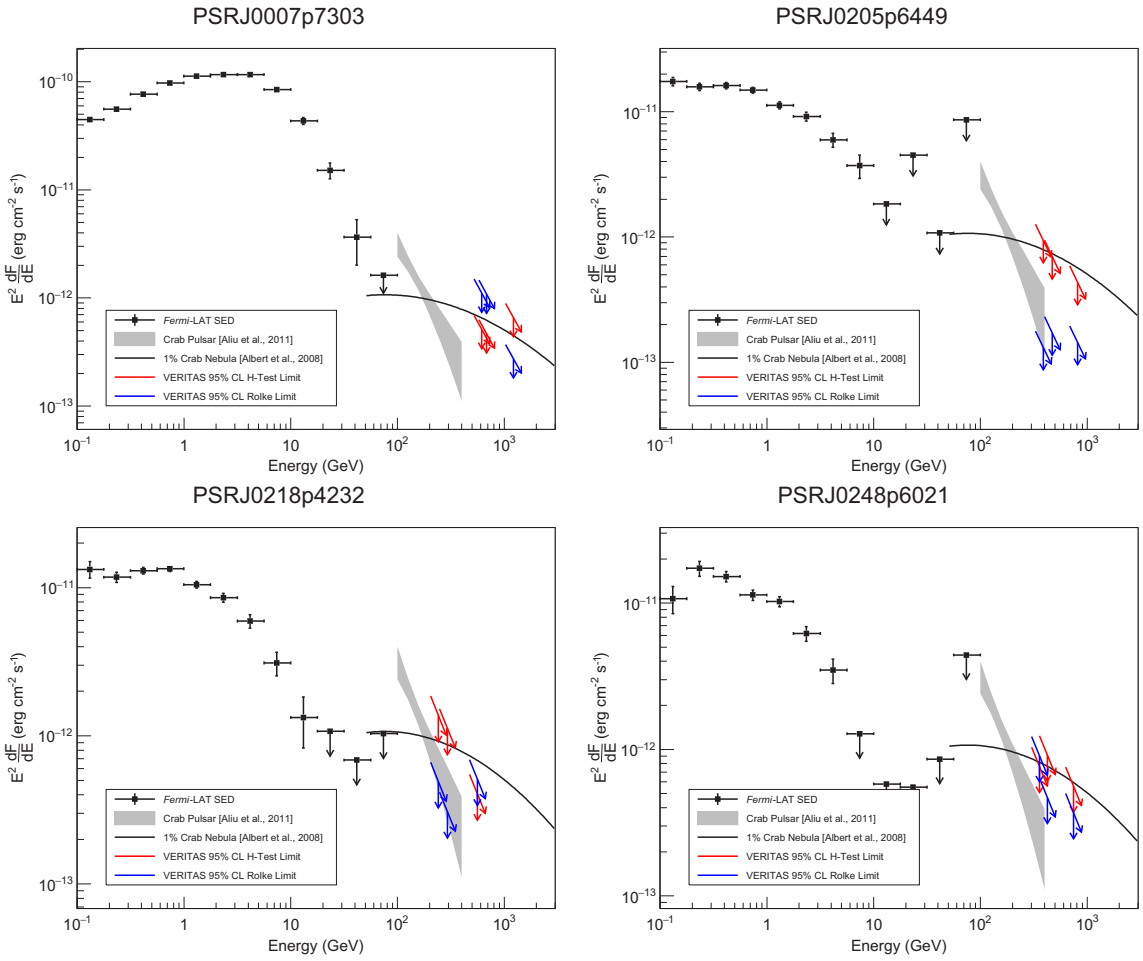

Figure 6–16: Fermi LAT spectra with VERITAS differential flux upper limits multiplied by E^2 calculated using two separate methods plotted at the energy thresholds for each set of cuts. The Fermi LAT spectral points are shown in black. The VERITAS flux upper limits for the gated analyses calculated using the method of Rolke are represented by the blue vertical arrows and the VERITAS flux upper limits determined from the H-test statistics using the method described in [25] are represented by the red vertical arrows. The slope of the diagonal arrows above the VERITAS upper limit arrows represents the assumed spectral index of 3.8. The black lines represent the spectral shape of the Crab nebula as measured by [33], scaled to 1%, and the grey bow ties represent the spectrum of the Crab pulsar as measured by [38].

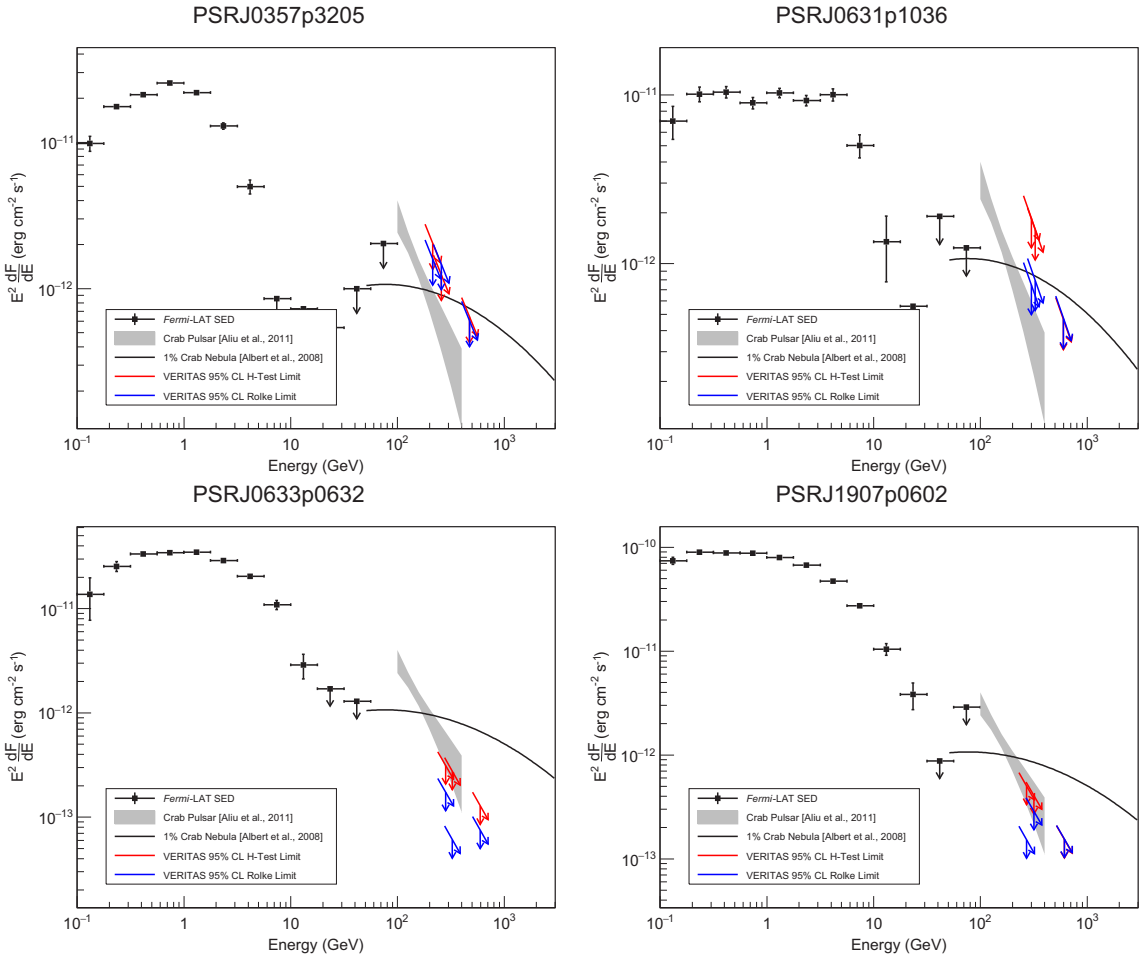

Figure 6–17: Continuation of Figure 6–16.

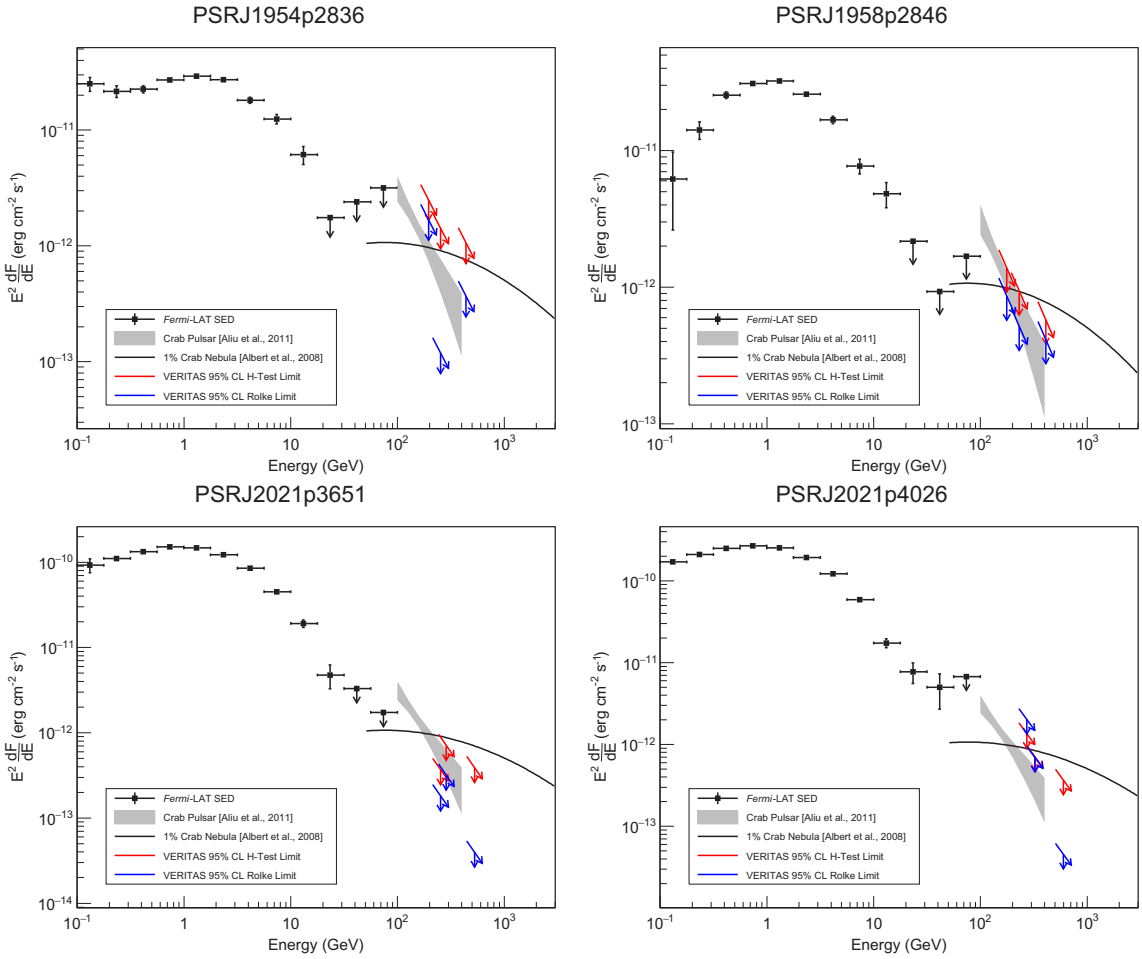

Figure 6–18: Continuation of Figure 6–16.

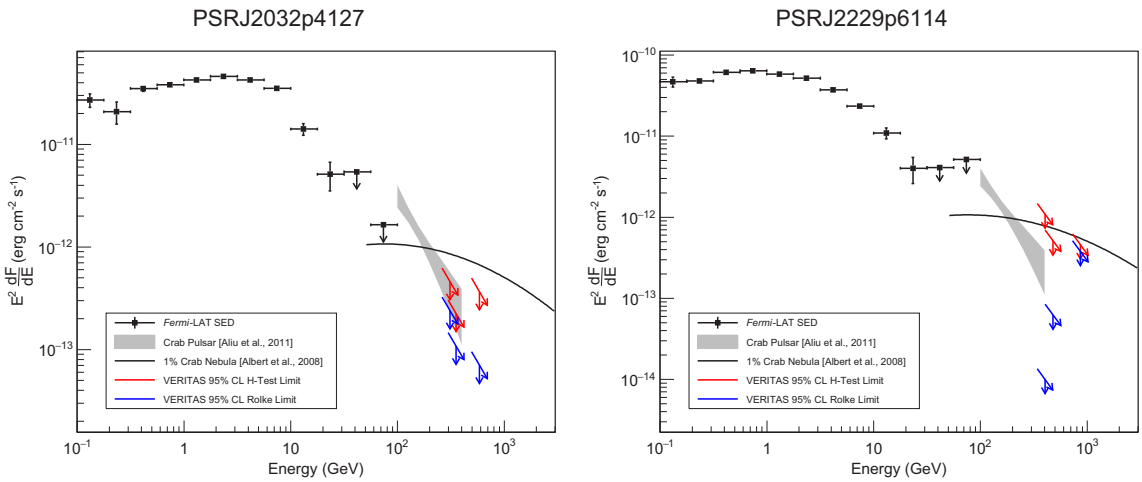

Figure 6–19: Continuation of Figure 6–16.

CHAPTER 7
Conclusions

Archival VERITAS data was searched for pulsations from 14 pulsars appearing in the second Fermi pulsar catalogue. The pulsars were searched for periodicity using a gated test, and with the H-test, for three sets of event selection cuts. The details of the data analysis procedures are described in chapters 5 and 6. No pulsations were observed for any of the VERITAS archival pulsars, using the two periodicity tests, and three sets of event selection cuts. Integral flux upper limits were calculated for the gated analyses using the method of Rolke [106] and for the calculated H-test statistics using the method described in [25] assuming a power law spectrum with a spectral index of 3.8. These upper limits were compared with the corresponding limits obtained from the VEGAS archival pulsar analyses. The limits obtained from the two analysis packages for both the gated and H-test analyses were found to be correlated as expected, with the VEGAS limits being approximately 25% lower on average than the Event Display limits. This is consistent with known sensitivity differences between the two analysis packages using the standard cuts. The flux upper limits calculated as a result of this search are the first and therefore the best limits obtained thus far for these pulsars. In order to contextualize the calculated flux upper limits, Fermi LAT spectra were produced for each of the pulsars using 7.6 years of LAT data. The integral flux upper limits were converted to differential flux upper

limits at the energy thresholds determined for each set of cuts, and plotted with the Fermi spectral points. The results of these analyses are presented in section 6.4.

As mentioned in section 3.2, the VERITAS archival pulsar search was undertaken in order to expand the catalogue of VHE pulsars, and to constrain pulsar gamma ray emission models. No pulsations were discovered in this search, so the Crab and Vela pulsars currently remain the only known VHE gamma ray pulsars. All of the flux upper limits presented here are consistent with curvature radiation gamma-ray emission scenarios that predict exponential cutoffs in the gamma-ray spectra. The majority of the limits appear to be above any possible power law extrapolation of the Fermi LAT spectrum into the VHE band. These limits constrain possible spectral hardening or a new emission component to be at, or below the calculated limits. Some of these limits may be of interest to those proposing models that invoke new spectral components at high energies such as [4], [93] and [92] (see section 2.8.4). The flux upper limits for PSRJ0205+6449, PSRJ1954+2836, PSRJ1958+2846, PSRJ2021+4026, PSRJ2032+4127 and PSRJ2229+6114 may constrain possible power law extrapolations of the Fermi LAT spectra into the VHE band. Some of these limits may also be of interest to those proposing models where the same population of particles is responsible for both the high energy Fermi LAT spectral points and the VHE spectral points, such as [73], [87] and [86] (see section 2.8.4). The limits presented here constrain the flux of a potential VHE pulsed signal to be approximately that of the Crab pulsar or below. The systematic uncertainty on these limits (see section 5.9) is estimated to be approximately 40% due to the assumed spectral index of 3.8.

The sensitivity of VERITAS to VHE pulsar gamma-ray fluxes is limited by the size, number and array configuration of the telescopes as well as the analysis methodology. The upcoming IACT array CTA will be approximately an order of magnitude more sensitive than VERITAS using current analysis methods, which may lead to further detections of VHE pulsars, and will allow similar flux upper limits to be achieved in a fraction of the VERITAS observing times. The limits presented here may help to plan observations of the VERITAS archival pulsars with CTA by providing estimates for the observation times required to obtain important constraints. The detection and measurements of the pulse profiles and spectra of more VHE pulsars will provide important constraints on the emission regions and mechanisms responsible for the observed pulsed gamma rays, but for now the exact nature of the VHE gamma ray emission from pulsars remains to be determined.

APPENDIX A
Neutron star formation

During the life of a main sequence star, hydrogen fusion in the core provides the outward radiation pressure that balances the inward pressure due to gravity. If the mass of the star is less than four solar masses ($M_\odot$), when the hydrogen fuel in the core is exhausted, helium fusion in the core eventually begins, leading to the production of carbon. Carbon and helium nuclei fuse to produce oxygen, leading to a core composed primarily of carbon and oxygen. If the mass of the star is between 4 and 8 $M_\odot$, further fusion reactions take place, resulting in a core composed primarily of oxygen, magnesium and neon. In both cases, the outer layers of the star will eventually be expelled, resulting in a planetary nebula and a carbon-oxygen or oxygen-magnesium-neon white dwarf, held up by electron degeneracy pressure. If the original mass of the star is greater than 8 $M_\odot$, fusion reactions of heavier elements take place, eventually resulting in an increasingly massive iron core. Fusion reactions resulting in the production of nuclei heavier than iron are not exothermic processes, therefore fusion reactions in the iron core do not take place. Radiation pressure from fusion reactions can no longer contribute to holding up the core, and the core is now held up primarily by electron degeneracy pressure. Eventually, the increasing mass of the core causes it to contract to the point where the associated increase in temperature causes photo-dissociation of the iron nuclei into protons, neutrons and lighter nuclei. The free electrons that had been providing the electron degeneracy

pressure required to hold up the core are captured by protons and other nuclei, producing copious amounts of neutrinos. These processes result in the rapid collapse of the core of the star, now composed primarily of neutrons. The core continues to collapse until neutron degeneracy pressure halts the collapse, causing a rebound that results in a shock wave that expels the outer layers of the star in a supernova explosion. The expelled outer layers of the star become a supernova remnant. If the mass of the star is between 8 and 25 $M_{\odot}$, the core collapses into a neutron star which is composed primarily of neutrons and held up by neutron degeneracy pressure. If the mass of the star exceeds 25 $M_{\odot}$, the core collapses into a black hole. Asymmetries in supernova explosions are thought to impart high velocities to neutron stars, called kicks. The discovery of pulsars in supernova remnants and pulsars with high velocities is consistent with the idea that they form in supernovae.

APPENDIX B
Pulsar radiation emission mechanisms

As mentioned in section 2.5, the nature of the radiation mechanisms responsible for the observed radiation from rotation-powered pulsars is currently not well understood. Incoherent processes are thought to be responsible for the optical, X-ray and gamma-ray emission from pulsars [110]. The following four sections describe the various proposed incoherent pulsar radiation emission mechanisms: inverse Compton scattering, cyclotron radiation, synchrotron radiation and curvature radiation. Section B.5 describes pair production on strong magnetic fields, which may limit the energy of the emitted photons.

B.1 Inverse Compton scattering

Compton scattering refers to the scattering of a photon by a charged particle (usually an electron, which is assumed here), where the photon transfers some of its energy to the electron. This results in an increase in the kinetic energy of the electron and the wavelength of the photon. For $E_\gamma < m_e c^2$, the cross section for this interaction is given by the Thomson cross section:

$$\sigma_T = \frac{8\pi}{3} r_e^2 = \frac{e^4}{6\pi\epsilon_0^2 m_e^2 c^4} = 6.65 \times 10^{-29}\ m^2$$

where $r_e = \dfrac{e^2}{4\pi\epsilon_0 m_e c^2}$ is the classical electron radius and ϵ_0 is the permittivity of free space. For $E_\gamma > m_e c^2$ the cross section is reduced, and given by the Klein-Nishina

formula:

$$\sigma_{KN} = \pi r_e^2 \frac{1}{x}\left\{\left[1 - \frac{2(x+1)}{x^2}\right]\ln(2x+1)\frac{1}{2} + \frac{4}{x} + \frac{1}{2(2x+1)^2}\right\}$$

where $x = \dfrac{h\nu}{m_e c^2}$ and $h\nu$ is the energy of the photon [110].

Inverse Compton scattering refers to the scattering of a high-energy photon by a charged particle, where the charged particle gives energy to the photon. This results in an decrease in the kinetic energy of the electron and the wavelength of the photon. This process occurs in astrophysical contexts, where high-energy electrons up-scatter low-energy photons into the gamma-ray regime. For a photon with energy $h\nu_0$, up-scattered by an electron with energy $E_e = \gamma m_e c^2$, the average energy of the up-scattered photon is given by:

$$\langle h\nu \rangle = \frac{4}{3}\gamma^2 h\nu_0$$

showing that electrons with large Lorentz factors may up-scatter photons by a significant amount [110]. The power lost by an electron travelling in a photon field due to inverse Compton scattering is given by:

$$\left(\frac{dE}{dt}\right)_{IC} = \frac{4}{3}\sigma_T u_{rad}\left(\frac{v^2}{c^2}\right)\gamma^2$$

where u_{rad} is the radiation energy density. For a population of electrons following a power-law energy distribution up-scattering a low-energy photon field, the resulting

distribution of up-scattered photons also follows a power law [109]. Inverse Compton scattering may play a role in the incoherent emission from pulsars, which is described in sections 2.8 and 2.8.4.

B.2 Cyclotron radiation

When a non-relativistic charged particle moves in a magnetic field, it spirals around the magnetic field lines due to the Lorentz force, emitting electromagnetic radiation called cyclotron radiation. For a particle moving perpendicular to the magnetic field lines, the frequency ν_L with which the particle moves around the magnetic field lines (called the Larmor frequency) may be determined by equating the Lorentz force qvB, with the centripetal force, $\frac{mv^2}{r}$ where B is the strength of the magnetic field and q, v and r are the charge, velocity and radius of curvature of the particle respectively. This leads to:

$$\nu_L = \frac{v}{2\pi r} = \frac{qB}{2\pi m}.$$

The total power radiated is given by the Larmor formula:

$$\frac{dE}{dt} = \frac{q^2 a^2}{6\pi\epsilon_0 c^3} = \frac{q^4 v^2 B^2}{6\pi\epsilon_0 c^3 m^2}$$

where q is the charge of the particle, and a is the acceleration of the particle, given by $a = \frac{v^2}{r} = \left(\frac{v}{r}\right)v = 2\pi\nu_L v = \frac{qvB}{m}$. The cyclotron radiation emitted by the charged particle is polarized, and emitted at the Larmor frequency.

B.3 Synchrotron radiation

When a relativistic charged particle moves in a magnetic field, the particle spirals about the magnetic field lines, emitting radiation over a wide range of frequencies. For a particle moving perpendicular to the magnetic field lines, the particle rotates about the field lines at a frequency:

$$\nu_G = \frac{v}{2\pi r} = \frac{qB}{2\pi\gamma m}$$

called the gyrofrequency, where γ is the Lorentz factor. Due to the relativistic beaming of light, the emission is beamed in a cone in the direction of motion of the particle, with approximately half of the total emission concentrated into a cone of half angle $\frac{1}{\gamma}$ radians. Due to the beaming, the radiation is observed over only $\frac{1}{\gamma}$ radians in the orbit of the particle, when the emission cone becomes visible to the observer. Transforming from the rest frame of the particle to the observer's frame reduces the duration of the observed pulse of radiation by a factor of γ^2. Therefore, the duration of the observed pulse of radiation is approximately $\delta t \sim \frac{1}{\gamma^3 \nu_G}$. The frequency spectrum of the pulse spans a wide range of frequencies, peaking at approximately:

$$\nu_p \sim \frac{1}{\delta t} = \gamma^3 \nu_G = \frac{\gamma^3 v}{2\pi r} = \frac{\gamma^2 qB}{2\pi m}.$$

A more detailed analysis for a particle moving with angle α with respect to the magnetic field lines yields a characteristic frequency of:

$$\nu_c = \frac{3\gamma^3 c}{4\pi\rho} \sim \frac{3}{2}\gamma^3 \nu_G \sin\alpha = \frac{3\gamma^2 qB}{4\pi m}\sin\alpha$$

where ρ is the radius of curvature of the particle's trajectory [110]. The power spectrum peaks at approximately $\nu_{max} \sim 0.29\nu_C$, and is proportional to $\nu^{\frac{1}{3}}$ below ν_{max} and $\exp[-(\frac{\nu}{\nu_c})]$ above ν_c. The radiated power is given by the relativistic Larmor formula:

$$\frac{dE}{dt} = \frac{q^2\gamma^4}{6\pi\epsilon_0 c^3}\Big(a_\perp^2 + \gamma^2 a_\parallel^2\Big)$$

where q is the charge of the particle, $a_\perp$ is the component of the acceleration perpendicular to the velocity vector, and $a_\parallel$ is the component of the acceleration parallel to the velocity vector [110]. For synchrotron radiation, the acceleration of the particles is perpendicular to the velocity vector, with $a_\perp = \frac{v_\perp^2}{r} = \Big(\frac{v_\perp}{r}\Big)v_\perp = 2\pi\nu_G v_\perp = \frac{qBv\sin\alpha}{\gamma m}$. The emitted power is therefore given by:

$$\dot{E}_{sync} = \frac{q^2\gamma^4}{6\pi\epsilon_0 c^3}a_\perp^2 = \frac{q^2\gamma^4}{6\pi\epsilon_0 c^3}\Big(\frac{v_\perp^2}{r}\Big)^2 = \frac{q^2\gamma^4}{6\pi\epsilon_0 c^3}\Big(\frac{qBv\sin\alpha}{\gamma m}\Big)^2 = \frac{q^4\gamma^2 B^2 v^2\sin^2\alpha}{6\pi\epsilon_0 c^3 m^2}.$$

Averaging over pitch angles, the emitted power may be expressed as:

$$\Big(\frac{dE}{dt}\Big)_{sync} = \frac{4}{3}\sigma_T u_{mag}\Big(\frac{v^2}{c^2}\Big)\gamma^2$$

where $u_{mag} = \dfrac{B}{2\mu_0}$ is the energy density of the magnetic field, and μ_0 is the permeability of free space, similar to the result for inverse Compton scattering [110]. The

shape of the synchrotron radiation spectrum produced by a population of charged particles depends on the shape of the energy spectrum of the charged particles. For example, the synchrotron radiation spectrum emitted by a population of charged particles with a power law energy distribution is also a power law. At low frequencies, the absorption of the synchrotron light by the charged particles leads to a spectrum proportional to $\nu^{\frac{5}{2}}$ [110]. Like cyclotron radiation, synchrotron radiation photons are highly polarized.

B.4 Curvature radiation

When a relativistic charged particle moves in a very strong magnetic field, the motion perpendicular to the magnetic field lines may be rapidly damped by synchrotron radiation losses, causing the particle to move along the magnetic field lines. The motion of the charged particle along the curved magnetic field lines causes the particle to radiate electromagnetic radiation in a manner similar to synchrotron radiation [110] [85]. Like synchrotron radiation, the emission is beamed in the forward direction with an angle of approximately $\frac{1}{\gamma}$ radians, with a characteristic frequency given by:

$$\nu_c = \frac{3\gamma^3 c}{4\pi\rho}$$

where ρ is the radius of curvature of the magnetic field lines. The single particle spectrum is the same as for synchrotron radiation, proportional to $\nu^{\frac{1}{3}}$ below ν_{max} and $\exp[-(\frac{\nu}{\nu_c})]$ above ν_c. The emitted power is given by:

$$\dot{E}_{curv} = \frac{q^2\gamma^4 c}{6\pi\epsilon_0\rho^2}.$$

Like synchrotron radiation, the photon spectrum produced by a population of charged particles with a power law distribution is also a power law. Due to the strong magnetic fields associated with pulsars, many models of pulsar gamma-ray emission invoke curvature radiation as the dominant emission mechanism [95] [107] [13] [10] [30]. In these models, charged particles are accelerated in gaps in the plasma (see section 2.8) by electric fields with components in the direction of the magnetic field lines $E_\parallel$. The particles accelerated in the gaps have a maximum energy, which is attained when the rate of energy gained by the particles due to the electric field, $\dot{E}_{E_\parallel} = qE_\parallel v$, is equal to the power emitted via curvature radiation $\dot{E}_{curv} = \frac{q^2\gamma^4 c}{6\pi\epsilon_0\rho^2}$. This is called the radiation reaction limit, and assuming $v \sim c$, occurs at:

$$E_{max} = \gamma_{max} mc^2 = \left(\frac{6\pi\epsilon_0\rho^2 E_\parallel}{q}\right)^{\frac{1}{4}} mc^2.$$

For a distribution of charged particles, the maximum particle energy leads to a break in the photon spectrum, which occurs at an energy of:

$$E_\gamma^{max} = h\nu_c^{max} = h\frac{3\gamma_{max}^3 c}{4\pi\rho} = \hbar c\rho^{\frac{1}{2}}\left(\frac{3}{2}\right)^{\frac{7}{4}}\left(\frac{4\pi\epsilon_0 E_\parallel}{q}\right)^{\frac{3}{4}} = \hbar c\gamma_{max}\left(\frac{3}{2}\right)^{\frac{3}{2}}\left(\frac{4\pi\epsilon_0 E_\parallel}{q}\right)^{\frac{1}{2}}.$$

Above the break energy E_γ^{max}, the photon spectrum falls off exponentially [10]. Such a spectral feature is called an exponential cutoff, and is predicted by models that

invoke curvature radiation as the primary gamma-ray emission mechanism from pulsars. The accelerating field $E_{\|}$ may be related to the height of the emission region above the pulsar and the strength of the magnetic field at the surface and the period, yielding:

$$E_{\gamma}^{max} \sim \left(\frac{8c}{r\omega}\right)\left(\frac{\rho_c}{r}\right)^{\frac{1}{2}}(4\pi\epsilon_0\eta B_{12})^{\frac{3}{4}}(P_{0.1})^{-\frac{7}{4}} \ \text{GeV}$$

where r is the height of the emission region above the neutron star, ω is the angular frequency of the pulsar, B_{12} is the magnetic field strength at the surface of the pulsar in units of 10^{12} G, $P_{0.1}$ is the period of the pulsar in units of 0.1 seconds and η is an efficiency factor of the electric field such that $E_{\|} = \eta\frac{r\omega B}{c}$ [10]. The above expression allows the measured maximum energy of the emitted photons to be related to the distance of the emission region above the surface of the pulsar for emission scenarios involving curvature radiation.

B.5 Pair production on strong magnetic fields

Due to the strong magnetic fields in the vicinity of pulsars, high-energy photons in the pulsar magnetosphere may undergo pair production: $\gamma_B + \gamma_{HE} \rightarrow e^+ + e^-$. The probability for this process to occur is an increasing function of the photon energy and $B_{\perp}$, the component of the magnetic field perpendicular to the direction of motion of the photons [9] [120]. The produced pairs may radiate additional photons which produce further pairs, resulting in a cascade of secondary photons and pairs, called secondary pair plasma. This process may limit the maximum energy of the photons that escape the pulsar magnetosphere. For pulsar gamma-ray emission

models with emission regions close to the surface of the pulsar (see section 2.8), high-energy photons are expected to undergo significant pair production due to the strong magnetic field. These models predict breaks in the photon spectrum at E_{γ}^{max} with super-exponential cutoffs above the break energy [10] [9]. For a given pulsar, the maximum measured photon energy may be used to constrain the minimum height of the gamma-ray emission region above the surface of the pulsar using the following equation:

$$E_{\gamma}^{max} \sim 0.4\sqrt{P}\Big(\frac{r}{R_{NS}}\Big)^{\frac{1}{2}} max\Big\{1, \frac{0.1B_{cr}}{B_0}\Big(\frac{r}{R_{NS}}\Big)^3\Big\} \text{ GeV}$$

where P is the period of the pulsar, r is the height of the emission region above the surface of the neutron star, R_{NS} is the radius of the neutron star, B_0 is the magnetic field strength at the pole of the pulsar and $B_{cr} = \frac{m_e^2 c^3}{e\hbar} = 4.41 \times 10^{13}\ G$ [9].

References

[1] Scott Wakely and Deirdre Horan . TeVCat . http://tevcat.uchicago.edu/.

[2] A. Djannati-Ata for the H.E.S.S. Collaboration. H.E.S.S. stereoscopic observations of the Vela Pulsar above 100 GeV . https://fskbhe1.puk.ac.za/people/mboett/Texas2017/Djannati.pdf.

[3] A. Nepomuk Otte for the VERITAS Collaboration. The Upgrade of VERITAS with High Efficiency Photomultipliers. *ArXiv e-prints, 1110.4702*, 2011.

[4] F. A. Aharonian, S. V. Bogovalov, and D. Khangulyan. Abrupt acceleration of a 'cold' ultrarelativistic wind from the Crab pulsar. *Nature*, 482:507–509, 2012.

[5] Ahnen et al. Search for VHE gamma-ray emission from Geminga pulsar and nebula with the MAGIC telescopes. *A&A*, 591:A138, 2016.

[6] I. Arka and G. Dubus. Pulsed high-energy γ-rays from thermal populations in the current sheets of pulsar winds. *A&A*, 550:A101, 2013.

[7] J. Arons and E. T. Scharlemann. Pair formation above pulsar polar caps - Structure of the low altitude acceleration zone. *ApJ*, 231:854–879, 1979.

[8] W. Baade and F. Zwicky. On Super-novae. *Proceedings of the National Academy of Science*, 20:254–259, 1934.

[9] M. G. Baring. High-energy emission from pulsars: the polar cap scenario. *Advances in Space Research*, 33:552–560, 2004.

[10] M. G. Baring. Perspectives on Gamma-Ray Pulsar Emission. In *American Institute of Physics Conference Series*, volume 1379, pages 74–81, 2011.

[11] D. Berge, S. Funk, and J. Hinton. Background modelling in very-high-energy γ-ray astronomy. *A&A*, 466:1219–1229, 2007.

[12] H. Bradt, S. Rappaport, and W. Mayer. X-Ray and Optical Observations of the Pulsar NP 0532 in the Crab Nebula. *Nature*, 222:728–730, 1969.

[13] M. Breed, C. Venter, and A. K. Harding. Very-high energy emission from pulsars. *ArXiv e-prints, 1607.06480*, 2016.

[14] Rene Brun and Fons Rademakers. ROOT - an object oriented data analysis framework. *Nuclear Instruments and Methods in Physics Research Section A*, 389(1 - 2):81 86, 1997.

[15] B.W. Carroll and D.A. Ostlie. *An Introduction to Modern Astrophysics*. Pearson Addison-Wesley, 2007.

[16] N. Chamel, P. Haensel, J. L. Zdunik, and A. F. Fantina. On the Maximum Mass of Neutron Stars. *International Journal of Modern Physics E*, 22:1330018, 2013.

[17] K. S. Cheng, C. Ho, and M. Ruderman. Energetic radiation from rapidly spinning pulsars. I - Outer magnetosphere gaps. II - VELA and Crab. *ApJ*, 300:500–539, 1986.

[18] K. S. Cheng, C. Ho, and M. Ruderman. Energetic Radiation from Rapidly Spinning Pulsars. II. VELA and Crab. *ApJ*, 300:522, 1986.

[19] W. J. Cocke, M. J. Disney, and D. J. Taylor. Discovery of Optical Signals from Pulsar NP 0532. *Nature*, 221:525–527, 1969.

[20] The FERMI Collaboration. LAT Gamma-ray Pulsar Timing Models. `https://confluence.slac.stanford.edu/display/GLAMCOG/LAT+Gamma-ray+Pulsar+Timing+Models`.

[21] The FERMI Collaboration. Pulsar Ephemerides for Timing LAT Pulsars. `http://fermi.gsfc.nasa.gov/ssc/data/access/lat/ephems/`.

[22] VERITAS collaboration. VERITAS website. http://veritas.sao.arizona.edu/.

[23] Wikimedia Commons. `https://commons.wikimedia.org/wiki/File:Atmospheric_electromagnetic_transmittance_or_opacity.jpg`.

[24] John M. Davies and Eugene S. Cotton. Design of the Quartermaster solar furnace. *Solar Energy*, 1(2-3):16 – 22, 1957. The Proceedings of the Solar Furnace Symposium.

[25] O. C. de Jager. On periodicity tests and flux limit calculations for gamma-ray pulsars. *ApJ*, 436:239–248, 1994.

[26] O. C. de Jager, B. C. Raubenheimer, and J. W. H. Swanepoel. A poweful test for weak periodic signals with unknown light curve shape in sparse data. *A&A*, 221:180–190, 1989.

[27] LeBohec S. Duke C. http://www.physics.utah.edu/gammaray/GrISU/.

[28] R. T. Edwards, G. B. Hobbs, and R. N. Manchester. TEMPO2, a new pulsar timing package - II. The timing model and precision estimates. *MNRAS*, 372:1549–1574, 2006.

[29] Abdo et al. The First Fermi Large Area Telescope Catalog of Gamma-Ray Pulsars. *ApJS*, 187:460–494, 2010.

[30] Abdo et al. The Second Fermi Large Area Telescope Catalog of Gamma-Ray Pulsars. *ApJS*, 208:17, 2013.

[31] Abeysekara et al. The 2HWC HAWC Observatory Gamma-Ray Catalog. *ApJ*, 843:40, 2017.

[32] Acero et al. Fermi Large Area Telescope Third Source Catalog. *ApJS*, 218:23, 2015.

[33] Albert et al. VHE γ-Ray Observation of the Crab Nebula and its Pulsar with the MAGIC Telescope. *ApJ*, 674:1037–1055, 2008.

[34] Aleksić et al. Observations of the Crab Pulsar between 25 and 100 GeV with the MAGIC I Telescope. *ApJ*, 742:43, 2011.

[35] Aleksić et al. Phase-resolved energy spectra of the Crab pulsar in the range of 50-400 GeV measured with the MAGIC telescopes. *A&A*, 540:A69, 2012.

[36] Aleksić et al. Measurement of the Crab Nebula spectrum over three decades in energy with the MAGIC telescopes. *Journal of High Energy Astrophysics*, 5:30–38, 2015.

[37] Aliu et al. Observation of Pulsed γ-Rays Above 25 GeV from the Crab Pulsar with MAGIC. *Science*, 322:1221, 2008.

[38] Aliu et al. Detection of Pulsed Gamma Rays Above 100 GeV from the Crab Pulsar. *Science*, 334:69, 2011.

[39] Aliu et al. A Search for Pulsations from Geminga above 100 GeV with VERITAS. *ApJ*, 800:61, 2015.

[40] Archambault et al. Gamma-ray observations under bright moonlight with VERITAS. *Astroparticle Physics*, 91:34–43, 2017.

[41] Berk et al. Modtran6: a major upgrade of the modtran radiative transfer code. In *Proceedings of SPIE - The International Society for Optical Engineering*, volume 9088, page 90880H, 2014.

[42] Bertsch et al. Pulsed high-energy gamma-radiation from Geminga (1E0630 + 178). *Nature*, 357:306, 1992.

[43] D. Kniffen et al. Gamma radiation from the Crab Nebula above 35 MeV. *Nature*, pages 397–399.

[44] Djannati-Ataï et al. volume 1792 of *AIP Conf. Proc.*, page 040028, 2017.

[45] Fritz et al. X-ray Pulsar in the Crab Nebula. *Science*, 164:709–712, 1969.

[46] Hall et al. Veritas CFDs. *Proceedings of the 28th International Cosmic Ray Conference. Trukuba, Japan.*, 5:2851, July 2003.

[47] Halpern et al. Discovery of High-Energy Gamma-Ray Pulsations from PSR J2021+3651 with AGILE. *ApJ*, 688:L33, 2008.

[48] Heck et al. *CORSIKA: a Monte Carlo code to simulate extensive air showers.* 1998.

[49] Hewish et al. Observation of a Rapidly Pulsating Radio Source. *Nature*, 217:709–713, 1968.

[50] Konopelko et al. Effectiveness of TeV γ-ray observations at large zenith angles with a stereoscopic system of imaging atmospheric Cerenkov telescopes. *Journal of Physics G Nuclear Physics*, 25:1989–2000, 1999.

[51] Kraushaar et al. High-Energy Cosmic Gamma-Ray Observations from the OSO-3 Satellite. *ApJ*, 177:341, 1972.

[52] Nolan et al. Fermi Large Area Telescope Second Source Catalog. *ApJ*, 199:31, 2012.

[53] Pellizzoni et al. Discovery of New Gamma-Ray Pulsars with AGILE. *ApJ*, 695(1):L115, 2009.

[54] S. Ansoldi et al. Teraelectronvolt pulsed emission from the Crab pulsar detected by MAGIC. *A&A*, 585:A133, 2016.

[55] Vacanti et al. Muon ring images with an atmospheric Čerenkov telescope. *Astroparticle Physics*, 2:1–11, February 1994.

[56] Verrecchia et al. An updated list of AGILE bright γ-ray sources and their variability in pointing mode. *A&A*, 558:A137, 2013.

[57] Weekes et al. Observation of TeV gamma rays from the Crab nebula using the atmospheric Cerenkov imaging technique. *ApJ*, 342:379–395, 1989.

[58] Tanabashi et al. (Particle Data Group). Review of particle physics. *Phys. Rev. D*, 98:030001, 2018.

[59] Australia Telescope National Facility. ATNF Pulsar Catalogue. `http://www.atnf.csiro.au/research/pulsar/psrcat/`.

[60] S.J. Fegan and V.V. Vassiliev. Analysis of muon images for VERITAS. VERITAS internal memo, March 2007.

[61] G. J. Feldman and R. D. Cousins. Unified approach to the classical statistical analysis of small signals. *Phys. Rev. D*, 57:3873–3889, 1998.

[62] Fermi LAT collaboration. Fermi LAT website at NASA . `https://fermi.gsfc.nasa.gov/ssc/Fermi_5_year.jpg`.

[63] Fermi LAT Multiwavelength Coordinating Group. Public List of LAT-Detected Gamma-Ray Pulsars. `https://confluence.slac.stanford.edu/display/GLAMCOG/Public+List+of+LAT-Detected+Gamma-Ray+Pulsars`.

[64] B. Zitzer for the VERITAS Collaboration. The VERITAS Upgraded Telescope-Level Trigger Systems: Technical Details and Performance Characterization. *ArXiv e-prints, 1307.8360*, 2013.

[65] G. T. Richards et al. Recent pulsar results from VERITAS on Geminga and the missing link binary pulsar PSR J1023+0038. *ArXiv e-prints, 1508.06969*, 2015.

[66] T. GOLD. Rotating neutron stars as the origin of the pulsating radio sources. *Nature*, 218:731–732, 1968.

[67] P. Goldreich and W. H. Julian. Pulsar Electrodynamics. *ApJ*, 157:869–880, 1969.

[68] Claus Grupen and Boris Shwartz. *Particle Detectors*. Cambridge University Press, 2008.

[69] Hammamatsu. Photomultiplier Tubes, Basics and Applications. `https://www.hamamatsu.com/resources/pdf/etd/PMT_handbook_v3aE.pdf`.

[70] D. Hanna. Calibration Techniques for VERITAS. In *Proceedings of the 30th International Cosmic Ray Conference. Mérida, Yucatán, Mexico.*, volume 3, pages 1417–1420, 2008.

[71] D. Hanna, A. McCann, M. McCutcheon, and L. Nikkinen. An LED-based flasher system for VERITAS. *Nuclear Instruments and Methods in Physics Research A*, 612:278–287, 2010.

[72] A. Harding and A. Muslimov. Pulsar Slot Gaps and Unidentified Egret Sources. *Ap&SS*, 297:63–70, 2005.

[73] A. K. Harding and C. Kalapotharakos. Synchrotron Self-Compton Emission from the Crab and Other Pulsars. *ApJ*, 811:63, 2015.

[74] A. K. Harding, J. V. Stern, J. Dyks, and M. Frackowiak. High-Altitude Emission from Pulsar Slot Gaps: The Crab Pulsar. *ApJ*, 680:1378–1393, 2008.

[75] O. Helene. Upper limit of peak area. *Nuclear Instruments and Methods in Physics Research*, 212:319–322, 1983.

[76] A. M. Hillas. Cerenkov light images of EAS produced by primary gamma. In *Proceedings of the 19th International Cosmic Ray Conference. La Jolla, United States.*, volume 3, pages 445–448, 1985.

[77] K. Hirotani. Three-dimensional non-vacuum pulsar outer-gap model: Localized acceleration electric field in the higher altitudes. *ApJ*, 798(2):L40, 2015.

[78] G. B. Hobbs, R. T. Edwards, and R. N. Manchester. TEMPO2, a new pulsar-timing package - I. An overview. *MNRAS*, 369:655–672, 2006.

[79] J. Holder. Atmospheric Cherenkov Gamma-ray Telescopes. *ArXiv e-prints, 1510.05675*, 2015.

[80] The Smithsonian institution and the University of Arizona. The MMT observatory.
`https://www.mmto.org/`.

[81] J. Condon and S. Ransom. Essential Radio Astronomy. `http://www.cv.nrao.edu/~sransom/web/Ch6.html`.

[82] J. Holder et al. (The VERITAS collaboration). The first VERITAS telescope. *Astroparticle Physics*, 25(6):391 – 401, 2006.

[83] T.-P. Li and Y.-Q. Ma. Analysis methods for results in gamma-ray astronomy. *ApJ*, 272:317–324, 1983.

[84] D. R. Lorimer and M. Kramer. *Handbook of Pulsar Astronomy*. Cambridge University Press, December 2004.

[85] Andrew Lyne and Francis Graham-Smith. *Pulsar Astronomy*. Cambridge University Press, 2012.

[86] M. Lyutikov. Inverse Compton model of pulsar high-energy emission. *MNRAS*, 431:2580–2589, 2013.

[87] M. Lyutikov, N. Otte, and A. McCann. The Very High Energy Emission from Pulsars: A Case for Inverse Compton Scattering. *ApJ*, 754:33, 2012.

[88] G. Maier. Monte Carlo studies of the VERITAS array of Cherenkov telescopes. *Proceedings of the 30th International Cosmic Ray Conference. Mérida, Yucatán, Mexico.*, 3:1413–1416, 2008.

[89] R. N. Manchester, G. B. Hobbs, A. Teoh, and M. Hobbs. The Australia Telescope National Facility Pulsar Catalogue. *AJ*, 129:1993–2006, 2005.

[90] S. Mangano. Cherenkov Telescope Array Status Report. *ArXiv e-prints, 1705.07805*, 2017.

[91] Andrew McCann. *Discovery of Emission above 100 GeV from The Crab Pulsar With VERITAS*. PhD thesis, McGill University, 2011.

[92] I. Mochol. Pulsar striped winds. *ArXiv e-prints, 1702.00720*, 2017.

[93] I. Mochol and J. Pétri. Very high energy emission as a probe of relativistic magnetic reconnection in pulsar winds. *MNRAS*, 449:L51–L55, 2015.

[94] A. G. Muslimov and A. K. Harding. Extended Acceleration in Slot Gaps and Pulsar High-Energy Emission. *ApJ*, 588:430–440, 2003.

[95] A. G. Muslimov and A. K. Harding. High-Altitude Particle Acceleration and Radiation in Pulsar Slot Gaps. *ApJ*, 606:1143–1153, 2004.

[96] NASA. `https://www.nasa.gov/sites/default/files/0003356.jpg`.

[97] NASA. Fermi Gamma-ray Space Telescope Education and Public Outreach website . `http://fermi.sonoma.edu/multimedia/gallery/GLASTinSpaceWeb.jpg`.

[98] NASA's High Energy Astrophysics Science Archive Research Center. CGRO gamma-ray pulsars. `https://heasarc.gsfc.nasa.gov/docs/cgro/images/epo/gallery/pulsars/index.html`.

[99] NASA's High Energy Astrophysics Science Archive Research Center. Observatories: COS-B. `https://heasarc.gsfc.nasa.gov/Images/cosb/cosb_photo.gif`.

[100] NASA's High Energy Astrophysics Science Archive Research Center. Observatories: COS-B. `https://heasarc.gsfc.nasa.gov/Images/cosb/cosb_gcem.gif`.

[101] NASA's High Energy Astrophysics Science Archive Research Center. Observatories: OSO-3. `https://heasarc.gsfc.nasa.gov/Images/oso/oso3.gif`.

[102] NASA's High Energy Astrophysics Science Archive Research Center. Observatories: SAS-2. `https://heasarc.gsfc.nasa.gov/Images/sas2/sas2_flight.gif`.

[103] A. Nepomuk Otte and Veritas Collaboration. First Detection of a Pulsar above 100 GeV. In *Journal of Physics Conference Series*, volume 375 of *Journal of Physics Conference Series*, page 052023, 2012.

[104] F. Özel and P. Freire. Masses, Radii, and the Equation of State of Neutron Stars. *ARA&A*, 54:401–440, 2016.

[105] J. Pétri. High-energy emission from the pulsar striped wind: a synchrotron model for gamma-ray pulsars. *MNRAS*, 424:2023–2027, 2012.

[106] W. A. Rolke and A. M. López. Confidence intervals and upper bounds for small signals in the presence of background noise. *Nuclear Instruments and Methods in Physics Research A*, 458:745–758, 2001.

[107] R. W. Romani. Gamma-Ray Pulsars: Radiation Processes in the Outer Magnetosphere. *ApJ*, 470:469, 1996.

[108] M. A. Ruderman and P. G. Sutherland. Theory of pulsars - Polar caps, sparks, and coherent microwave radiation. *ApJ*, 196:51–72, 1975.

[109] G. B. Rybicki and A. P. Lightman. *Radiative Processes in Astrophysics*. Wiley-VCH, 1986.

[110] M. S. Longair. *High Energy Astrophysics*. Cambridge University Press, 2011.

[111] T. Y. Saito, S. Bonnefoy, K. Hirotani, and R. Zanin for the MAGIC collaboration. Detection of VHE Bridge emission from the Crab pulsar with the MAGIC Telescopes. *ArXiv e-prints, 1502.02757*, 2015.

[112] Martin Schroedter. *The Very High Energy Spectra of AGN*. PhD thesis, The University of Arizona, 2004.

[113] P. A. Sturrock. A Model of Pulsars. *ApJ*, 164:529, 1971.

[114] The HAWC collaboration. HAWC collaboration website . `https://www.hawc-observatory.org/img/hawc_site_201611_hires.jpg`.

[115] The H.E.S.S. collaboration. H.E.S.S. collaboration website . `https://www.mpi-hd.mpg.de/hfm/HESS/pages/press/2012/HESS_II_first_light/images/Image_13.JPG`.

[116] The MAGIC collaboration. MAGIC collaboration website . `https://magicold.mpp.mpg.de/gallery/pictures/IMG_2520.JPG`.

[117] D. J. Thompson. Gamma Ray Pulsars. In *Cosmic Gamma-Ray Sources*, volume 304 of *Astrophysics and Space Science Library*, 2004.

[118] D. J. Thompson. Gamma ray astrophysics: the EGRET results. *Reports on Progress in Physics*, 71(11):116901, 2008.

[119] D. J. Thompson, C. E. Fichtel, D. A. Kniffen, and H. B. Ogelman. SAS-2 high-energy gamma-ray observations of the VELA pulsar. *ApJ*, 200:L79–L82, 1975.

[120] Wu-yang Tsai and Thomas Erber. Photon Pair Creation in Intense Magnetic Fields. *Phys. Rev. D*, D10:492, 1974.

[121] Jonathan Tyler. Muon identification with VERITAS using the Hough Transform. Master's thesis, McGill University, 2011.

[122] VERITAS Collaboration: T. Nagai, R. McKay, G. Sleege, and D. Petry. Focal Plane Instrumentation of VERITAS. *ArXiv e-prints, 0709.4517*, 2007.

[123] A. Weinstein. The VERITAS Trigger System. *Proceedings of the 30th International Cosmic Ray Conference. Mérida, Yucatán, Mexico.*, 3:1539–1542, 2008.